



**HAL**  
open science

## Quantification of uncertainties of radiative transfer calculation in urban canopy models

Robert Schoetter, Cyril Caliot, Tin-Yuet Chung, Robin J. Hogan, Valéry Masson

► **To cite this version:**

Robert Schoetter, Cyril Caliot, Tin-Yuet Chung, Robin J. Hogan, Valéry Masson. Quantification of uncertainties of radiative transfer calculation in urban canopy models. *Boundary-Layer Meteorology*, 2023, 10.1007/s10546-023-00827-9 . hal-04330926

**HAL Id: hal-04330926**

**<https://hal.science/hal-04330926>**

Submitted on 8 Dec 2023

**HAL** is a multi-disciplinary open access archive for the deposit and dissemination of scientific research documents, whether they are published or not. The documents may come from teaching and research institutions in France or abroad, or from public or private research centers.

L'archive ouverte pluridisciplinaire **HAL**, est destinée au dépôt et à la diffusion de documents scientifiques de niveau recherche, publiés ou non, émanant des établissements d'enseignement et de recherche français ou étrangers, des laboratoires publics ou privés.

1 **Quantification of uncertainties of radiative transfer**  
2 **calculation in urban canopy models**

3 **Robert Schoetter · Cyril Caliot ·**  
4 **Tin-Yuet Chung · Robin J. Hogan ·**  
5 **Valéry Masson**

6  
7 Received: DD Month YEAR / Accepted: DD Month YEAR

8 **Abstract**

9 Urban canopy models simplify urban morphology and physical processes such  
10 as radiative transfer to calculate the urban surface energy balance as a lower  
11 boundary condition for atmospheric models at low computational cost. The  
12 present study uses a reference model of urban radiative transfer based on the  
13 Monte Carlo method, which solves the radiative transfer equation by taking  
14 into account the complex geometry of buildings and vegetation. Procedurally-  
15 generated urban morphologies similar to the Local Climate Zones (LCZ) are  
16 studied to cover the variety of urban forms that exist globally. The uncertain-  
17 ties arising from the simplification of the urban morphology as an infinitely-  
18 long street canyon or a regular array of square blocks are quantified. In addi-  
19 tion, uncertainties due to the neglect of specular or spectral material reflectivi-  
20 ties and the involved atmosphere are investigated. It is found that for all LCZ,  
21 the street canyon and block morphologies lead to a systematic overestima-  
22 tion (underestimation) of the fraction of solar radiation absorbed by the walls  
23 (ground). The neglect of pitched roofs has a strong influence on the simulated

---

R. Schoetter  
CNRM, Université de Toulouse, Météo-France, CNRS, 42 avenue Gaspard Coriolis,  
Toulouse, France  
Tel.: +33-5-61079723  
E-mail: robert.schoetter@meteo.fr

C. Caliot  
CNRS, UPPA, E2S, LMAP, 1 Allée du Parc Montaury, Anglet, France

T.-Y. Chung  
CNRM, Université de Toulouse, Météo-France, CNRS, 42 avenue Gaspard Coriolis,  
Toulouse, France

R. J. Hogan  
ECMWF, Reading, United Kingdom

V. Masson  
CNRM, Université de Toulouse, Météo-France, CNRS, 42 avenue Gaspard Coriolis,  
Toulouse, France

urban solar radiation budget for low solar elevation angles. Neglecting the spectral reflectivity of urban materials does not lead to relevant uncertainties in the broadband radiative fluxes. Specularly reflecting windows only change the urban solar radiation budget for a central business district morphology with a high glazing ratio. The participating atmosphere can strongly influence the urban terrestrial radiation budget, especially for high-rise districts. Future urban canopy models should therefore improve the realism of the urban morphology, and consider a participating atmosphere for the calculation of terrestrial radiation.

**Keywords** Monte Carlo Method · Reference model · Uncertainty quantification · Urban canopy model · Urban radiative transfer

## 1 Introduction

About 60% of the world’s population lives in cities, and urbanisation is expected to continue (UN 2019). Urban populations are potentially exposed to heat stress, exacerbated by the (nocturnal) urban heat island (UHI) effect (Arnfield 2003) and global climate change (Collins et al. 2013). Radiative transfer in the complex three-dimensional urban morphology is a key physical process for the UHI (Oke 1982; Krayenhoff et al. 2014; Best and Grimmond 2015), building energy consumption (Strømman-Andersen and Sattrup 2011; Frayssinet et al. 2018), and human thermal comfort (Fröhlich and Matzarakis 2020; Dissegna et al. 2021; Geletič et al. 2022). Multiple reflections in the three-dimensional urban morphology reduce the effective solar reflectivity (albedo) of cities and increase the effective emissivity of terrestrial radiation. The radiative energy balance of the building envelope, and solar heat gain through windows is different in dense urban areas compared to isolated buildings. This can affect building energy consumption for heating, ventilation, and air-conditioning (HVAC), which accounts for about 40% of the global primary energy consumption (Yang et al. 2014). Outdoor human thermal comfort depends on the mean radiant temperature (MRT) (Höppe 1999; Thorsson et al. 2007; Mayer et al. 2008; Blazejczyk et al. 2012), which is influenced by solar shading and the emission of terrestrial radiation by buildings.

Numerical models have been developed to quantify the urban climate and to assess the impact of climate change mitigation and adaptation measures in urban areas. Urban canopy models (Grimmond et al. 2010, 2011) operate at the meso- (100 m to 10 km resolution) or global (10 km to 200 km resolution) scale and are based on a simplification of urban morphology (e.g., an infinitely-long street canyon) and physical processes such as radiative transfer. The building-resolving urban climate models (about 1 m resolution) such as Envi-Met (Bruse and Fleer 1998), Code\_Saturne (Milliez and Carissimo 2007), IBM-WRF (Lundquist et al. 2012), MITRAS (Salim et al. 2018), PALM-4U (Maronga et al. 2020; Krč et al. 2021; Salim et al. 2022), or uDALES (Suter et al. 2022) represent the detailed three-dimensional building morphology, but are so computationally expensive that they can only be used to simulate a

67 period of a few days for a part of a large city. They are not yet suitable for  
 68 numerical weather prediction or regional climate simulations.

69 The aim of the present study is to use a reference model of urban radiative  
 70 transfer based on the Monte Carlo Method (MCM) (Villefranque et al. 2019,  
 71 2022; Caliot et al. 2022) to quantify the uncertainties due to the simplification  
 72 of the radiative transfer calculation in urban canopy models. Such simplifica-  
 73 tions are the use of a simple urban morphology (infinitely-long street canyon,  
 74 regular blocks) with flat roofs, the assumption of broadband Lambertian ur-  
 75 ban materials, or neglecting the scattering and absorption of radiation in the  
 76 urban canopy layer by air, aerosols, or clouds. The present study addresses  
 77 this knowledge gap to guide future developments of urban canopy models.

## 78 2 Radiative Transfer Calculation in Urban Canopy Models

### 79 2.1 Simplification of Radiative Transfer Calculation

80 The radiative transfer equation (RTE) describes the propagation of the three-  
 81 dimensional field of spectral radiance in any direction through a potentially  
 82 scattering, absorbing, and emitting medium (participating medium). Bound-  
 83 ary conditions (e.g., radiation from the sun at the top of the atmosphere or  
 84 reflection and emission from the ground) must be taken into account. Solving  
 85 the RTE for the urban canopy layer (the volume between the ground and the  
 86 tallest buildings), a large number of radiation propagation directions, on a  
 87 very high resolution grid (e.g., 1 m), and for the real complex urban morphol-  
 88 ogy is too computationally expensive for urban canopy models. Instead, these  
 89 models simplify both the urban morphology and radiative transfer physics.  
 90 The peer-reviewed scientific literature published since 1970 that is referenced  
 91 by Google Scholar and indexed by the keywords *urban canopy model*, *urban*  
 92 *climate model*, or *urban radiation* has been reviewed to determine which radi-  
 93 ative transfer calculation methods (Tab. 1) have been used and how the urban  
 94 morphology is simplified (Tab. 2). The following methods have been identified:

- 95 – **Prescribed net radiation:** The net radiation at the surface is prescribed.  
 96 This method can be used when net radiation observations are available.
- 97 – **Single reflection from a flat surface:** The net exchanged solar ( $SW_{net}$ )  
 98 and terrestrial radiative flux ( $LW_{net}$ ) at the surface is calculated by as-  
 99 suming that the surface is flat. In this case, there is one reflection of the  
 100 downwelling solar ( $SW_{down}$ ) and terrestrial ( $LW_{down}$ ) radiation at the sur-  
 101 face:

$$102 \quad SW_{net} = (\alpha - 1)SW_{down} \quad (1)$$

$$103 \quad LW_{net} = \epsilon (\sigma T_s^4 - LW_{down}) \quad (2)$$

103 where  $\alpha$  is the broadband albedo,  $\epsilon$  the emissivity, and  $T_s$  is the skin surface  
 104 temperature. The specifics of the three-dimensional urban morphology are  
 105 not taken into account.

- 106 – **Single reflection from a flat surface with empirical modification of**  
 107 **albedo and emissivity:** The effect of the three-dimensional urban mor-  
 108 phology is parameterised by an effective urban albedo (lower albedo than  
 109 for a flat surface) and/or an effective urban emissivity (higher emissivity  
 110 than for a flat surface) in Eqs. 1 and 2.
- 111 – **Horizontal layer representing the urban canopy:** The urban canopy  
 112 is represented by a horizontal layer that is located between the atmosphere  
 113 and the ground. This layer may have a different albedo, emissivity, and  
 114 skin surface temperature than the ground. It exchanges radiation with the  
 115 sky and the ground.
- 116 – **Extinction method:** The urban canopy layer is treated as a turbid medium  
 117 and the extinction of the radiation propagating through it due to intercep-  
 118 tion by buildings is calculated using the Beer-Lambert law. For exam-  
 119 ple, Chin et al. (2005) calculate the net radiation as a function of height,  
 120  $R_{net}(z)$ , based on the net radiation at the top of the urban canopy layer,  
 121  $R_{net}(z_{top})$ :

$$R_{net}(z) = R_{net}(z_{top}) \exp(-kL(z)), \quad (3)$$

122 where  $k$  is a user-defined extinction coefficient and  $L(z)$  is the cumulative  
 123 index of the building surface area:

$$L(z) = \int_z^{z_{top}} \lambda_p(z') dz', \quad (4)$$

124 where  $\lambda_p$  is the plane area building density.

- 125 – **Radiosity method with analytically calculated shape factors:** It is  
 126 assumed that the urban surfaces (e.g., the roof, wall, and ground facets) are  
 127 opaque and reflect and emit radiation isotropically (Lambertian surfaces).  
 128 A matrix of shape factors is computed, which provides the information  
 129 about the fraction of radiation leaving facet  $i$  ( $1 < i < N_f$ ) that is inter-  
 130 cepted by facet  $j$  ( $1 < j < N_f$ ). The term shape factor is used here because  
 131 it specifies the radiative exchange for the average of the facet as opposed to  
 132 the view factor, which is specific to a single point (Harman et al. 2004). A  
 133 linear system of  $N_f$  equations is solved to calculate the radiation incident  
 134 on each facet as a function of downwelling solar or terrestrial radiation,  
 135 facet reflectivities, and temperatures. For urban morphologies consisting  
 136 of rectangular axis-parallel surfaces (e.g. an infinitely-long street canyon),  
 137 the shape factors can be calculated analytically. The contribution of the  
 138 atmosphere to the radiative exchange between urban facets is neglected.
- 139 – **Discrete ordinates method:** The RTE is solved assuming that the dif-  
 140 fuse solar and terrestrial radiation travels into  $2 N_{stream}$  discrete directions.  
 141 An example is the two-stream approximation often used in atmospheric  
 142 models, which solves for downwelling and upwelling radiation, e.g. there is  
 143 only one stream per hemisphere ( $N_{stream} = 1$ ).
- 144 – **Radiosity method with shape factors calculated by MCM:** This  
 145 method is the same as the radiosity method, except for the calculation of  
 146 the shape factors. At the start of the simulation, rays are randomly traced

**Table 1** Methods to calculate radiative transfer in urban canopy models

Method	Studies
Prescribed net radiation	Myrup (1969); Tso et al. (1990)
Single reflection from a flat surface	Carlson and Boland (1978); Todhunter and Terjung (1988) (HFLUX); Saitoh et al. (1996)
Single reflection from a flat surface with empirical modification of urban albedo and emissivity	Outcalt (1972); Todhunter and Terjung (1988) (URBD, only solar); Grossman-Clarke et al. (2005); Dupont and Mestayer (2006) (SM2-U); De Ridder et al. (2015) (UrbClim); Wouters et al. (2016) (SURY)
Horizontal layer representing the urban canopy	Best (2005) (MOSES)
Extinction method	Dupont et al. (2004) (DA-SM2-U); Chin et al. (2005)
Radiosity method with analytically calculated shape factors	Arnfield (1976); Todhunter and Terjung (1988) (URBAN3); Sakakibara (1995); Mills (1997); Ca et al. (1999); Arnfield (2000); Masson (2000) (TEB); Kusaka et al. (2001) (SLUCM); Martilli et al. (2002) (BEP); Kondo et al. (2005); Krayenhoff and Voogt (2007) (TUF-2D, TUF-3D); Lee and Park (2008) (VUCM); Oleson et al. (2008); Porson et al. (2010) (MORUSES); Ryu et al. (2011); Thatcher and Hurley (2012); Schubert et al. (2012) (DCEP); Wang et al. (2013); Li et al. (2016) (LM3-UCM)
Discrete ordinates method	Hogan (2019b) (SPARTACUS-Urban)
Radiosity method with shape factors calculated by MCM	Kanda et al. (2005a,b) (SUMM); Krayenhoff et al. (2014); Wang (2014); Ryu et al. (2016); Nice et al. (2018) (VTUF-3D); Krayenhoff et al. (2020) (BEP-Tree); Meili et al. (2020) (UT&C); Wang et al. (2021) (ASLUM)

147 from each facet and it is count how many rays intersect another facet. The  
148 shape factors are calculated from the results of the MCM raytracing. This  
149 method is well suited for complex morphologies where it is not possible  
150 to calculate the shape factors analytically. For example, when representing  
151 urban vegetation, analytical shape factors can be calculated for a street  
152 canyon with one row of vegetation, but not for more complex vegetation  
153 shapes (Wang et al. 2021).

154 The most commonly used simplifications of urban morphology are the infinitely-  
155 long street canyon, the square, and the rectangular blocks. They are simple,  
156 but allow the three-dimensional nature of urban morphology to be represented.  
157 For such morphologies with axis-parallel rectangular Lambertian surfaces, it  
158 is convenient to calculate urban radiation using the radiosity method with  
159 analytically calculated shape factors. In the case of urban vegetation with a  
160 complex shape, the shape factors must be calculated using the MCM. An al-  
161 ternative is to consider that the urban canopy layer is a turbid medium and  
162 to use the Beer-Lambert extinction law to calculate how the radiation pass-  
163 ing through it is attenuated by collision with builings. Hogan (2019a,b) show  
164 that for typical urban districts, the distribution of wall-to-wall distances is

**Table 2** Simplified urban morphologies and number of layers ( $N_l$ ) used in urban canopy models. For  $N_l=1$ , the radiative observables are calculated only at ground level, for  $N_l=2$  they are calculated separately for the roof and the street canyon, for  $N_l=3$  they are calculated for the roof, wall, and ground, and for  $N_l = N$ , the radiative observables are calculated for a user-defined number of layers

Morphology	Studies	Number of layers
Flat surface	Myrup (1969); Outcalt (1972); Carlson and Boland (1978); Todhunter and Terjung (1988) (HFLUX, URBD); Tso et al. (1990); Saitoh et al. (1996); Grossman-Clarke et al. (2005); Dupont and Mestayer (2006) (SM2-U); De Ridder et al. (2015) (UrbClim); Wouters et al. (2016) (SURY)	1
Horizontal layer representing the urban canopy	Best (2005) (MOSES)	1
Vertically extended porous medium	Dupont et al. (2004) (DA-SM2-U); Chin et al. (2005)	N
Street canyon	Porson et al. (2010) (MORUSES); Li et al. (2016) (LM3-UCM);	2
	Arnfield (1976); Sakakibara (1995); Ca et al. (1999); Arnfield (2000); Masson (2000) (TEB); Kusaka et al. (2001) (SLUCM); Lee and Park (2008) (VUCM); Oleson et al. (2008); Ryu et al. (2011); Thatcher and Hurley (2012); Ryu et al. (2016); Meili et al. (2020) (UT&C); Wang et al. (2021) (ASLUM)	3
	Martilli et al. (2002) (BEP); Wang et al. (2013); Wang (2014); Krayenhoff et al. (2020) (BEP-Tree)	N
Double street canyon	Schubert et al. (2012) (DCEP)	N
Rectangular blocs	Todhunter and Terjung (1988) (URBAN3)	3
Square blocs	Mills (1997); Kanda et al. (2005a,b) (SUMM)	3
	Kondo et al. (2005)	N
Array of rectangular buildings with axis-parallel surfaces	Krayenhoff and Voogt (2007) (TUF-2D, TUF-3D); Krayenhoff et al. (2014); Nice et al. (2018) (VTUF-3D)	N
Exponential distribution of wall-to-wall distances	Hogan (2019b) (SPARTACUS-Urban)	N

165 exponential, implying that radiative transfer in the urban canopy layer can be  
 166 solved similarly to atmospheric radiative transfer.

167 In summary, the assumption of broadband Lambertian urban materials, the  
 168 neglect of participating air, aerosols, or clouds in the urban canopy layer, the  
 169 simplification of the urban morphology by a street canyon or regular blocks  
 170 with flat roofs are ubiquitous in urban canopy models. Therefore, the uncer-  
 171 tainties of these simplifications are investigated in the present study.

## 172 2.2 Previous Uncertainty Analyses

### 173 2.2.1 Reflections

174 Arnfield (1976), Kobayashi and Takamura (1994), Montávez et al. (2000), Har-  
175 man et al. (2004), and Yang and Li (2013) have studied the effect of (multiple)  
176 reflections on the urban radiation budget. They found that the importance of  
177 multiple reflections is higher when the albedo (emissivity) of different urban  
178 facets is higher (lower), and when the urban morphology is denser and taller.  
179 As most urban materials have a  $\epsilon$  close to 1, but typical values of  $\alpha$  are between  
180 0.1 and 0.5, a lower number of reflections is usually assumed for terrestrial ra-  
181 diation than for solar radiation.

### 182 2.2.2 Specularly Reflecting Materials

183 Aida and Gotoh (1982) used a MCM radiation model to quantify the effect of  
184 specular reflections on the effective albedo of a street canyon for the extreme  
185 case where the entire street canyon consists of purely specularly reflecting ma-  
186 terials. They found that the albedo is 15% higher for a solar zenith angle of  
187  $0^\circ$ , because purely specular reflection from the ground leads to a strong re-  
188 duction in multiple reflections compared to pure Lambertian reflection. The  
189 albedo is 50% lower for a solar zenith angle of  $80^\circ$  because the specular re-  
190 flection from the wall surfaces leads to more reflected radiation downwards  
191 compared to pure Lambertian reflection. However, for real cities, less influence  
192 from specularly reflecting materials can be expected because it is not realistic  
193 for all surfaces to be pure specular reflectors. Verseghy and Munro (1989a)  
194 found discrepancies of 5 to  $10 \text{ W m}^{-2}$  between their numerical model assum-  
195 ing Lambertian reflections and observations on a building wall. This could be  
196 explained by specular reflection of direct solar radiation from windows on the  
197 opposite wall. Kotthaus and Grimmond (2014) performed flux observations in  
198 the Central Business District (CBD) of London and found that at their site  
199 and under clear-sky conditions, the surface albedo can be strongly influenced  
200 by specular reflections.

### 201 2.2.3 Participating Atmosphere

202 Verseghy and Munro (1989b) investigated the influence of the participating  
203 atmosphere using a numerical model of radiative transfer in a building court-  
204 yard. They found that neglecting the absorption by the air that is colder than  
205 the walls leads to an overestimation of the incoming longwave radiation at the  
206 wall surfaces by 8 to  $9 \text{ W m}^{-2}$  for clear-sky conditions and by 4 to  $7 \text{ W m}^{-2}$  for  
207 overcast conditions. Based on a numerical study, Hogan (2019b) showed that  
208 atmospheric absorption significantly modifies the energy balance of the urban  
209 canopy and that its effect increases with building height. Net absorption by air  
210 in the urban canopy layer was found to be  $75 \text{ W m}^{-2}$  for 50 m high buildings  
211 and the wall surface temperature was 10 K higher than the air temperature.



#### 2.2.4 Isotropic Downwelling Radiation

Urban radiation models typically assume that the downwelling solar diffuse and terrestrial radiation are isotropic. Verseghe and Munro (1989a) found that for clear-sky conditions, this assumption leads to an underestimation (overestimation) of the incoming solar radiation at the sunlit (shaded) walls. This is because, in the real-world, most of the diffuse solar radiation comes from a direction that is close to the direction of the sun. When the urban canopy model is coupled with an atmospheric model using delta-Eddington scaling (Joseph et al. 1976) in the radiation scheme, this will not be the case as circumsolar scattered radiation is treated as direct solar radiation to improve the accuracy of the total solar radiation. For terrestrial radiation, Verseghe and Munro (1989b) found that the assumption of isotropic downwelling radiation leads to an underestimation of the radiation incident on a vertical wall, since more terrestrial radiation comes from the parts of the sky close to the horizon than from those at the zenith.

### 3 Reference Model of Urban Radiative Transfer

#### 3.1 The HTRDR-Urban Monte-Carlo Model of Urban Radiative Transfer

The HTRDR-Urban reference model of urban radiative transfer has been introduced by Caliot et al. (2022). It is based on the MCM and solves the RTE for solar and terrestrial radiation taking into account the participating atmosphere with non-gray absorption, emission, and anisotropic scattering. The solar and terrestrial radiative flux densities are calculated with a backward MCM using the null-collision technique (Galtier et al. 2013; El Hafi et al. 2021) and accelerating grids (Villefranque et al. 2019). The upper boundary is the top of the atmosphere (TOA), where is the solar spectrum irradiance obtained by averaging the data of year 2020 from the data set Coddington et al. (2015). The lower boundary is the Earth's surface consisting of vegetation and buildings. Material surfaces are assumed to be opaque and reflect radiation in a Lambertian or specular manner, with a spectral dependence of their reflectivity. The Spectral Library of impervious Urban Materials (SLUM) available from the London Urban Micromet data Archive (LUMA) (Kotthaus et al. 2013, 2014) with measured spectral Lambertian reflectivities is included in HTRDR-Urban. The specular reflectivity of window glass is calculated with the measured complex refractive index given by Rubin (1985). The constant surface temperature of different facets can be specified. The participating atmosphere is characterised by the 3D fields of spectral and directional radiative properties of gases, liquid droplets, and solid particles, which can be specified by the user as data of absorption and scattering coefficient data and scattering phase functions.

### 251 3.2 Calculation of Mean Radiant Temperature

252 HTRDR-Urban can be used to calculate the MRT, which is one of the input  
 253 variables for thermal climate indices such as the Physiological Equivalent Tem-  
 254 perature (PET) (Höppe 1999) or the Universal Thermal Climate Index (UTCI)  
 255 (Blazejczyk et al. 2012). For this purpose, a user-defined file in wavefront for-  
 256 mat with the desired human-like geometry can be provided to HTRDR-Urban.  
 257 An MRT map of user-defined spatial extent and resolution is obtained by plac-  
 258 ing the human-like geometry for each realization of the MCM algorithm at a  
 259 random location in each grid point of the MRT map and by rotating it by a  
 260 random azimuth angle between  $0^\circ$  and  $360^\circ$ . The solar ( $\dot{Q}_{\text{body,sw}}$ ) and terres-  
 261 trial ( $\dot{Q}_{\text{body,lw}}$ ) radiative flux density incident on the human-like geometry is  
 262 calculated using the algorithms described in Caliot et al. (2022). The MRT is  
 263 then calculated by

$$MRT = \left( \frac{(1 - \alpha_{\text{body}})\dot{Q}_{\text{body,sw}} + \dot{Q}_{\text{body,lw}}}{\epsilon_{\text{body}} \sigma} \right)^{0.25}. \quad (5)$$

264  $\alpha_{\text{body}}$  and  $\epsilon_{\text{body}}$  are the broadband solar albedo and thermal emissivity of the  
 265 human body. In the present study, the human body is a cylinder of 1 m height  
 266 and 0.14 m radius centred at 1.1 m above the ground. With this choice, similar  
 267 to Thorsson et al. (2007) and Dissegna et al. (2021), the radiative fluxes in the  
 268 horizontal direction have a weight of 0.88, while the upwelling and downwelling  
 269 fluxes have a weight of 0.06. The values of  $\alpha_{\text{body}}$  and  $\epsilon_{\text{body}}$  are set to 0.3 and  
 270 0.95 respectively. In the current implementation of the MRT calculation, the  
 271 human body does not affect the radiative transfer in the urban scene.

## 272 4 Procedurally-generated Urban Morphologies

### 273 4.1 Procedural City Generator

274 The urban morphologies studied are created using an in-house procedural city  
 275 generator. It assumes a flat terrain and generates a major road network start-  
 276 ing from a central square in radial mode (Kelly and McCabe 2006), based  
 277 on user-specified values for the number of sectors, the radius of the central  
 278 square, and the ring of major roads. The space in between the major roads is  
 279 filled with rectangular terrains of a user-specified length and width distribu-  
 280 tion. There are five geometric primitives of building types: 1) buildings aligned  
 281 with the major roads and 2-5) rectangular buildings with four different roof  
 282 types. Only the building type 1, which is aligned with the roads, can be placed  
 283 on the terrains adjacent to major roads. The user defines the probability that  
 284 a terrain will be covered by a given building type, and for each building type  
 285 the statistical distribution of its width, length, and number of storeys.

## 286 4.2 Urban Morphologies

287 Urban morphologies are based on the Local Climate Zone (LCZ) classification  
 288 of Stewart and Oke (2012). The lightweight low-rise LCZ7 is excluded as it  
 289 differs from the dense low-rise LCZ3 by the use of light materials, which is not  
 290 relevant to the present study. Based on the results of Tornay et al. (2017), who  
 291 conducted a survey with urban planners about urban morphologies typically  
 292 found in French cities, we further differentiate compact mid-rise LCZ2 into  
 293 compact mid-rise blocks (LCZ2a, the buildings are aligned with the streets)  
 294 and compact mid-rise rows (LCZ2b, the buildings form rows). The same is  
 295 done for the open low-rise LCZ6. These additional morphologies better repre-  
 296 sent the urban forms found in European cities. An additional CBD morphology  
 297 with open high-rise buildings and a facade glazing ratio ( $f_g$ ) of 0.9 is created  
 298 for the study of specularly-reflecting windows. The horizontal extent of the ur-  
 299 ban morphologies is a square of 800 m side length, except for LCZ4 (1200 m)  
 300 and CBD (400 m).

301 The urban morphologies are characterised by the morphology parameters,  
 302 plane area building density ( $\lambda_p$ ; Eq. 6), external facade surface density ( $\lambda_w$ ;  
 303 Eq. 7), and mean building height ( $H_{mean}$ ; Eq. 8). The footprint area of build-  
 304 ing  $n$  is  $A_n$ , its external facade area is  $AF_n$ , and its height is  $H_n$ . The total  
 305 number of buildings in a district is  $N_{build}$  and the total horizontal area of the  
 306 district is  $A_{district}$ .

307

$$\lambda_p = \frac{\sum_{n=1}^{N_{build}} A_n}{A_{district}} \quad (6)$$

$$\lambda_w = \frac{\sum_{n=1}^{N_{build}} AF_n}{A_{district}} \quad (7)$$

$$H_{mean} = \frac{\sum_{n=1}^{N_{build}} A_n H_n}{\sum_{n=1}^{N_{build}} A_n} \quad (8)$$

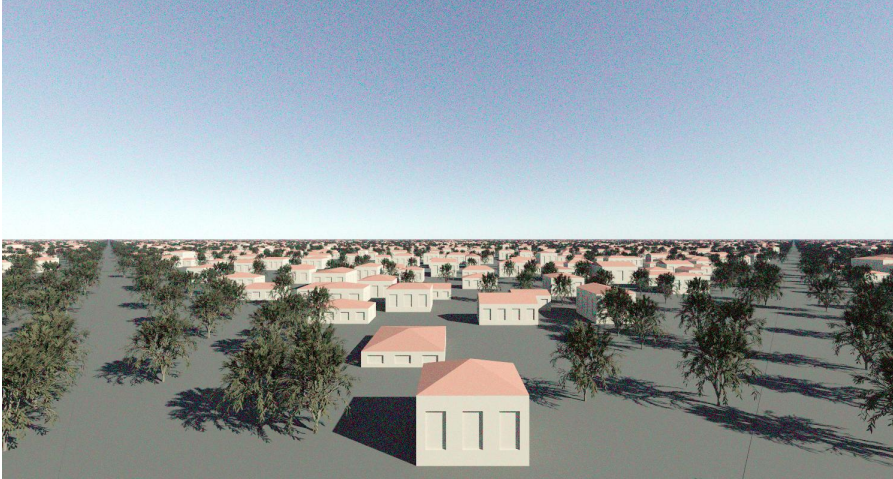
308 Simplified morphologies are generated for each district to allow for comparison  
 309 and assessment of uncertainties. These are: a representative street canyon, a  
 310 regular arrangement of square blocks, and a flat ground. The representative  
 311 infinitely-long street canyon has a building height equal to  $H_{mean}$  and the  
 312 height-over-width ratio (aspect ratio) of the street is calculated as follows

$$\frac{H}{W} = \frac{0.5\lambda_w}{1 - \lambda_p}. \quad (9)$$

313 The regular square blocks of height  $H_{mean}$  have a side length ( $l_{side}$ ) on a  
 314 square plot of length ( $l_{total}$ ):

$$l_{side} = \frac{4\lambda_p H_{mean}}{\lambda_w} \quad (10)$$

$$l_{total} = \frac{l_{side}}{\sqrt{\lambda_p}} \quad (11)$$




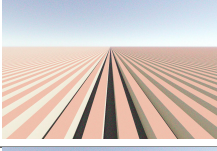
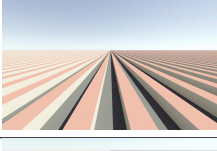
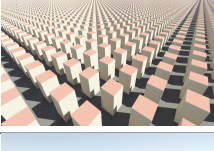
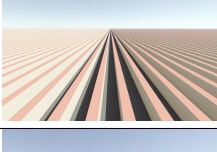
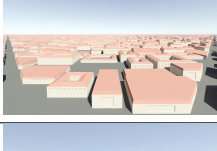
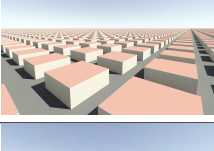
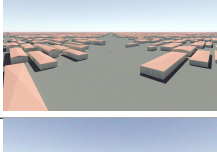
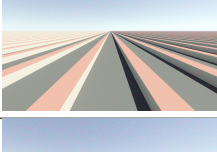
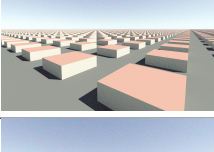
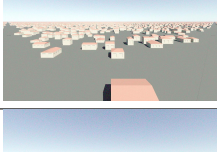
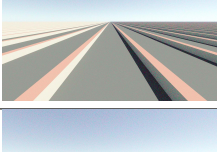
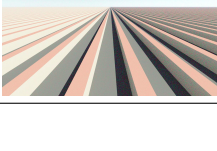
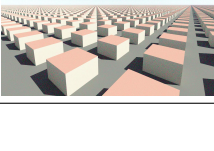
**Fig. 1** Rendering of the LCZ9 morphology with 1045 trees of the same type and a height of 10 m in the visible part of the solar spectrum. The number of pixels is  $1500 \times 800$ , the vertical field of view is  $70^\circ$ , and the number of samples per pixel is 200

315 The representative flat ground is the same as the representative street canyon,  
 316 but with  $H_{mean} = 0$  m. For all morphologies, potential overhanging roofs that  
 317 may occur in real cities are not considered. The morphologies LCZ2a, LCZ2b,  
 318 LCZ5, LCZ6a, LCZ6b, and LCZ9 have pitched roofs. Since pitched roofs are  
 319 not considered in the representative street canyon or regular square blocks, a  
 320 copy of these morphologies with flat roofs is created to quantify the effect of  
 321 pitched roofs. A realistic window geometry (window sill, glass pane surface) is  
 322 present, except for the urban morphologies LCZ8 (large low-rise) and LCZ10  
 323 (heavy industry), which have no windows. The 12 urban morphologies are pre-  
 324 sented in Tab. 3.

325 Trees represented by trunks, branches, and individual leaves, can be placed in  
 326 the procedurally-generated urban morphologies. In the present study, a sepa-  
 327 rate version of the LCZ2a, LCZ4, LCZ5, and LCZ9 morphologies is created,  
 328 in which trees of the same type with a height of 10 m, a diameter of 10.55 m,  
 329 and a leaf area index (LAI) of 2.24 are placed so that they do not intersect the  
 330 buildings. Because of the different values of  $\lambda_p$  in these morphologies, a differ-  
 331 ent number of trees can be placed in the morphologies (64 trees for LCZ2a, 963  
 332 for LCZ4, 869 for LCZ5, and 1045 for LCZ9). The plane area surface fraction  
 333 covered by trees is 0.01 for LCZ2a, 0.13 for LCZ4, 0.12 for LCZ5, and 0.14 for  
 334 LCZ9 (Fig. 1).

### 335 4.3 Distributions of Wall-to-wall and Wall-to-ground Distances

336 The distributions of wall-to-wall ( $p_{ww}$ ) and wall-to-ground distances ( $p_{wg}$ ) are  
 337 crucial for urban radiative transfer since they determine how much radiation  
 338 travelling through the urban canopy layer is intercepted by the different facets

Urban morphology	Realistic morphology	Street canyon	Square blocks
<b>LCZ1: Compact high-rise</b> $\lambda_p = 0.46$ ; $\lambda_w = 6.6$ ; $H_{mean} = 86.2$ m; $H_{max} = 115.1$ m; $\sigma_H = 15.1$ m; $\frac{H}{W} = 6.1$ ; $f_g = 0.3$			
<b>LCZ2a: Blocks of compact mid-rise</b> $\lambda_p = 0.53$ ; $\lambda_w = 1.21$ ; $H_{mean} = 16.1$ m; $H_{max} = 25.5$ m; $\sigma_H = 3.9$ m; $\frac{H}{W} = 1.29$ ; $f_g = 0.3$			
<b>LCZ2b: Rows of compact mid-rise</b> $\lambda_p = 0.35$ ; $\lambda_w = 0.97$ ; $H_{mean} = 17.2$ m; $H_{max} = 25.5$ m; $\sigma_H = 4.9$ m; $\frac{H}{W} = 0.75$ ; $f_g = 0.3$			
<b>LCZ3: Compact low-rise</b> $\lambda_p = 0.40$ ; $\lambda_w = 0.58$ ; $H_{mean} = 5.8$ m; $H_{max} = 11.0$ m; $\sigma_H = 1.4$ m; $\frac{H}{W} = 0.48$ ; $f_g = 0.3$			
<b>LCZ4: Open high-rise</b> $\lambda_p = 0.23$ ; $\lambda_w = 1.83$ ; $H_{mean} = 47.1$ m; $H_{max} = 62.7$ m; $\sigma_H = 8.0$ m; $\frac{H}{W} = 1.19$ ; $f_g = 0.3$			
<b>LCZ5: Open mid-rise</b> $\lambda_p = 0.32$ ; $\lambda_w = 1.18$ ; $H_{mean} = 15.6$ m; $H_{max} = 22.0$ m; $\sigma_H = 3.7$ m; $\frac{H}{W} = 0.87$ ; $f_g = 0.3$			
<b>LCZ6a: Blocks of open low-rise</b> $\lambda_p = 0.38$ ; $\lambda_w = 0.58$ ; $H_{mean} = 6.8$ m; $H_{max} = 12.6$ m; $\sigma_H = 1.8$ m; $\frac{H}{W} = 0.47$ ; $f_g = 0.3$			
<b>LCZ6b: Rows of open low-rise</b> $\lambda_p = 0.25$ ; $\lambda_w = 0.29$ ; $H_{mean} = 5.9$ m; $H_{max} = 9.4$ m; $\sigma_H = 1.2$ m; $\frac{H}{W} = 0.19$ ; $f_g = 0.3$			
<b>LCZ8: Large low-rise</b> $\lambda_p = 0.31$ ; $\lambda_w = 0.27$ ; $H_{mean} = 7.0$ m; $H_{max} = 12.1$ m; $\sigma_H = 1.8$ m; $\frac{H}{W} = 0.2$ ; $f_g = 0.0$			
<b>LCZ9: Sparsely built</b> $\lambda_p = 0.11$ ; $\lambda_w = 0.23$ ; $H_{mean} = 5.9$ m; $H_{max} = 10.6$ m; $\sigma_H = 1.4$ m; $\frac{H}{W} = 0.13$ ; $f_g = 0.3$			
<b>LCZ10: Heavy industry</b> $\lambda_p = 0.25$ ; $\lambda_w = 0.6$ ; $H_{mean} = 13.0$ m; $H_{max} = 21.0$ m; $\sigma_H = 4.6$ m; $\frac{H}{W} = 0.4$ ; $f_g = 0.0$			
<b>CBD: Central Business District</b> $\lambda_p = 0.24$ ; $\lambda_w = 3.1$ ; $H_{mean} = 75.2$ m; $H_{max} = 120.1$ m; $\sigma_H = 22.2$ m; $\frac{H}{W} = 2.0$ ; $f_g = 0.9$			

**Table 3** Rendering of the procedurally-generated urban morphologies in the visible part of the solar spectrum and its representative infinitely-long street canyon and regular array of square blocks.  $\sigma_H$  is the standard deviation of individual building heights,  $H_{max}$  the maximum building height. No simplified street canyon and block geometries are analysed for the CBD

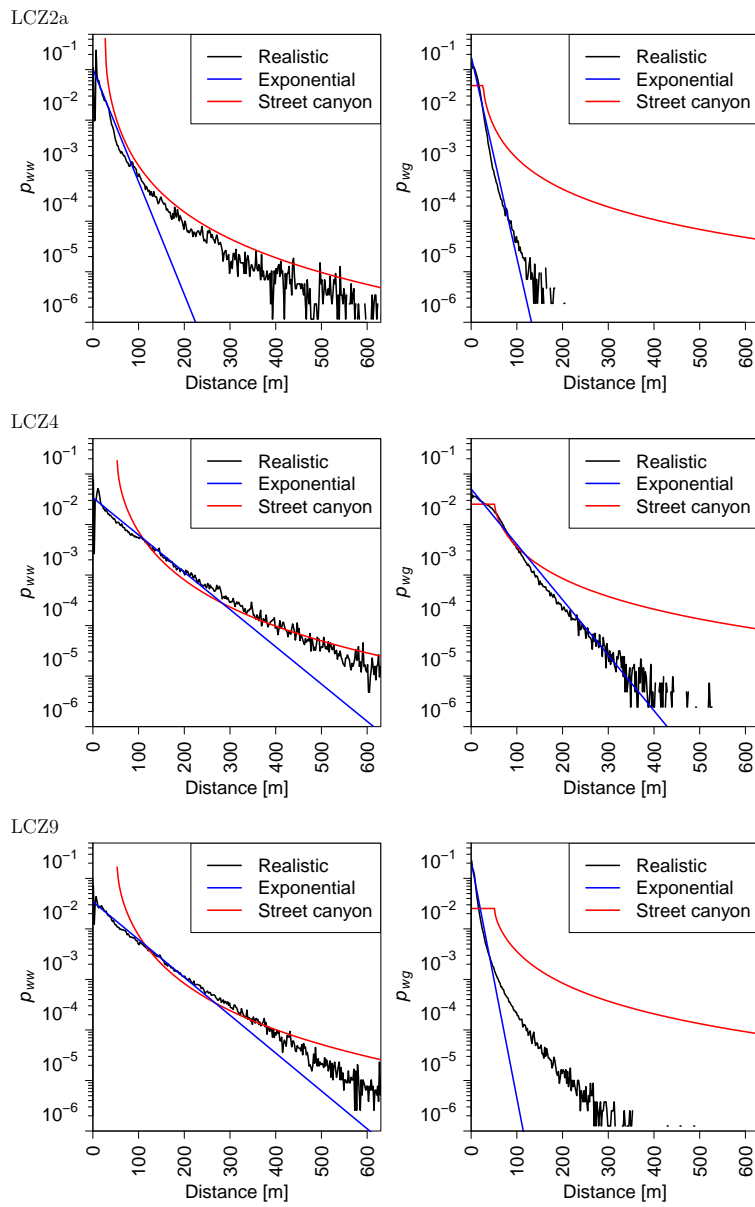


(Hogan 2019a). Hogan (2019a) studied these distributions for four real urban areas (central and residential London, downtown and residential Los Angeles) and compared them with two theoretical distributions: 1) the one that would be obtained for an infinitely-long street canyon, and 2) an exponential decay of  $p_{ww}$  and  $p_{wg}$  with increasing distance. It was found that  $p_{ww}$  for the real cities fits the exponential distribution well for distances between 0 and 200 m. The assumption of a street canyon geometry leads to a particularly bad  $p_{ww}$  for small distances, since it cannot represent buildings closer to each other than the width of the street canyon. For distances greater than 200 m and the districts in Los Angeles, the  $p_{ww}$  distribution obtained for the street canyon morphology is closer to the real distribution than the exponential distribution. For the districts in London, the real distribution lies in between the exponential and street canyon distributions. For  $p_{wg}$ , the exponential distribution fits best for distances below 200 m, while neither the exponential nor the infinite street canyon distribution fits well for larger distances. Stretton et al. (2022) analysed  $p_{ww}$  and  $p_{wg}$  for central London and Indianapolis (US) and found a relatively similar performance of the exponential model than Hogan (2019a). HTRDR-Urban is used to determine  $p_{ww}$  and  $p_{wg}$  for the procedurally-generated urban morphologies. For  $p_{ww}$ ,  $10^6$  rays are traced from a random point on a wall in the horizontal direction, and if the ray hits another wall, the distance that has been travelled is recorded. For  $p_{wg}$ ,  $10^6$  rays are traced in a randomly chosen downward direction from a random point on a wall. Figure 2 shows the results for LCZ2a, LCZ4, and LCZ9, the results for the remaining urban morphologies are shown in the supplementary Figs. 14 to 16. In general, the  $p_{ww}$  and  $p_{wg}$  distributions are close to the exponential distribution for small distances (up to 100 m to 200 m) and deviate considerably at higher distances. For LCZ2a and LCZ4 and distances greater than 200 m, the theoretical distribution obtained for the infinite street canyon fits better than the exponential distribution for  $p_{ww}$ , a result that is similar to Hogan (2019a)’s finding for downtown and residential Los Angeles. For  $p_{wg}$ , the exponential distribution is the best fit, even at higher distances. The distributions of  $p_{ww}$  and  $p_{wg}$  for the procedurally-generated cities are similar to those for real cities.

## 371 5 Methodology

### 372 5.1 Setup of Sensitivity Studies

373 The solar radiation budget in the layer of air between the ground and the  
 374 height of the tallest building (Urban Canopy Layer, UCL) is investigated. The  
 375 only source of energy is the downwelling solar radiation ( $\dot{Q}_D$ ) at the top of the  
 376 UCL. The  $\dot{Q}_D$  can be absorbed by the roofs ( $\dot{Q}_R$ ), the facades ( $\dot{Q}_F$ ; the sum of  
 377 the absorption by walls and windows), the ground ( $\dot{Q}_G$ ), potential trees ( $\dot{Q}_T$ ),  
 378 and the air in the UCL ( $\dot{Q}_{air}$ ). The radiation that is not absorbed leaves the  
 379 UCL towards the sky ( $\dot{Q}_U$ ). These radiative observables are studied because  
 380 the main objective of the radiation calculation in urban canopy models is to



**Fig. 2** Distribution of wall-to-wall ( $p_{ww}$ ) and wall-to-ground ( $p_{wg}$ ) distances for the urban morphologies LCZ2a, LCZ4, and LCZ9 and their representative infinitely-long street canyon and regular array of square blocks

381 calculate the effective albedo, emissivity, and radiative surface temperature of  
 382 the urban area as these variables are coupled with the radiation scheme of  
 383 the atmospheric model. A secondary objective may be to provide more detail  
 384 on the radiation absorbed by different urban facets (e.g. the average solar  
 385 radiation incident on all building facades) as the urban canopy models could  
 386 solve the energy budget of different urban facets separately.

387 In Sect. 6, the different terms of the solar radiation budget are displayed  
 388 normalised by the downwelling solar radiation at the top of the urban canopy  
 389 layer ( $\dot{Q}_D$ ). The normalised values are denoted by  $\dot{q}_U$ ,  $\dot{q}_R$ ,  $\dot{q}_F$ ,  $\dot{q}_G$ , and  $\dot{q}_T$ ,  
 390 for the upwelling solar radiation, and the radiation absorbed by the roofs,  
 391 the facades, the ground, and the trees respectively. The terrestrial radiation  
 392 budget consists of the longwave radiation exchanged by the sky ( $\dot{E}_{sky}$ ), the  
 393 roofs ( $\dot{E}_R$ ), the facades ( $\dot{E}_F$ ), the ground ( $\dot{E}_G$ ), the trees ( $\dot{E}_T$ ), and the air  
 394 ( $\dot{E}_{air}$ ).

395 Different boundary conditions for downwelling radiation are investigated:

396 – For direct-only downwelling solar radiation, only radiation from the solar  
 397 disc reaches the top of the urban canopy layer; there is no radiation  
 398 scattered by the atmosphere. To achieve this with HTRDR-Urban, the radiative  
 399 properties of the atmosphere are set to vacuum ones. Simulations  
 400 are performed for solar elevation angles ( $\gamma$ ) of  $1^\circ$ ,  $5^\circ$ ,  $10^\circ$ ,  $20^\circ$ ,  $30^\circ$ ,  $45^\circ$ ,  
 401  $60^\circ$ ,  $75^\circ$ , and  $90^\circ$ . The solar azimuth angle is sampled evenly between  $0^\circ$   
 402 and  $360^\circ$ . A larger number of MCM realisations is required for lower values  
 403 of  $\gamma$  to achieve a given accuracy of the radiative observables. Therefore, the  
 404 number of MCM realisations is calculated as follows

$$N_\gamma = int \left( \frac{N_{zen}}{\sin(\gamma)} \right). \quad (12)$$

405  $N_{zen}$  is the number of realisations when the sun is at the zenith ( $\gamma = 90^\circ$ ).  
 406 Rounding to the nearest integer is denoted by *int*.

407 – For the diffusive-only downwelling solar radiation, the solar radiation reach-  
 408 ing the top of the urban canopy layer is perfectly diffusive (e.g. similar to  
 409 an overcast sky with an optically thick cloud). To technically achieve this  
 410 with HTRDR-Urban, the atmospheric radiative properties are also set to  
 411 vacuum ones, and a sky model with isotropic downwelling solar radiation  
 412 with  $\dot{Q}_D$  normalised to  $1 \text{ W m}^{-2}$  is employed. The number of MCM reali-  
 413 sations is  $N_{zen}$ . There is no dependence of the results on  $\gamma$ .

414 – For the clear-sky conditions, the default atmospheric conditions consist of  
 415 the one-dimensional atmospheric profile from Hogan and Bozzo (2018).

## 416 5.2 Simplification of Urban Morphology

417 To quantify the uncertainty due to the simplification of the urban morphology,  
 418 HTRDR-Urban simulations are performed for real morphologies and their cor-  
 419 responding simplified morphologies such as infinitely-long street canyon, reg-  
 420 ular square blocks, and flat ground. All urban morphologies, including those



421 with flat roofs are studied. All surfaces are made of a Lambertian grey material  
 422 with a solar albedo of 0.3. Both direct and diffuse solar radiation boundary  
 423 conditions are considered. The value of  $N_{zen}$  is  $10^6$ .

### 424 5.3 Influence of Spectrally-reflecting Materials

425 The influence of spectrally-reflecting materials on the urban solar radiation  
 426 budget is studied for all urban morphologies. Measured spectral reflectivities  
 427 are available from the spectral library of impervious urban materials (SLUM),  
 428 which is part of the London urban micrometeorological archive (LUMA) (Kot-  
 429 thaus et al. 2013). An extreme case is considered. The roofs are made of rusting  
 430 cement red roofing tiles (R008), the facades of the weathered metal with cop-  
 431 per patina (Z004), and the ground of white weathered concrete (C006). In the  
 432 solar spectrum band, the albedo of the material C006 is low (0.2 at 350 nm),  
 433 but increases towards 0.5 at 600 nm. It remains relatively constant for larger  
 434 wavelengths. The metal Z004 has an albedo that varies along the solar spec-  
 435 trum. It is very low (0.1) at 350 nm, has a maximum of 0.55 at 500 nm, a  
 436 minimum of 0.27 at 650 nm, very high values (0.65 – 0.7) between 750 and  
 437 1100 nm, and another minimum (0.25) at 1500 nm. The Z004 material is one  
 438 of the materials with the largest variation in albedo with wavelength along  
 439 the solar spectrum that is included in the SLUM dataset. HTRDR-Urban  
 440 simulations are performed for direct-only and diffusive-only downwelling solar  
 441 radiation. HTRDR-Urban is used to calculate the incident radiative flux den-  
 442 sity ( $\dot{I}_{facet}$ ) on a specific type of facet (e.g., the roofs) and absorbed ( $\dot{Q}_{facet}$ )  
 443 by that type of facet. From the results, the effective broadband albedo ( $\alpha_{eff}$ )  
 444 of this facet is calculated for each urban morphology,  $\gamma$ , and the radiative  
 445 boundary condition following:

$$\alpha_{eff}(LCZ, \gamma) = 1 - \frac{\dot{Q}_{facet}(LCZ, \gamma)}{\dot{I}_{facet}(LCZ, \gamma)}. \quad (13)$$

446  $\alpha_{eff}$  is the broadband albedo that a material must have in order for the  
 447 broadband reflected radiative flux density to be the same as if the spectral  
 448 albedo of the material were used. It depends on the urban morphology or  
 449 the solar elevation angle, as these can change the spectral composition of  
 450 the radiation reaching a given surface. The HTRDR-Urban simulations are  
 451 repeated using the values of  $\alpha_{eff}$  as the broadband albedo. For all simulations,  
 452 the value of  $N_{zen}$  is  $10^6$ .

### 453 5.4 Influence of Specular Reflections from Windows

454 The influence of specular reflections from windows is studied for the urban  
 455 morphologies LCZ1, LCZ2a, LCZ9, and CBD. The boundary condition cor-  
 456 responds to a clear-sky situation. The spectral reflectivities of the non-glass  
 457 materials are taken from the SLUM database. All roofs are made of rusting

458 cement red roofing tiles (R008), all walls are made of white weathered con-  
 459 crete (C006), and all ground surfaces are made of black tarmac asphalt (A009).  
 460 Three simulations are made for each morphology and  $\gamma$ :

- 461 – **No windows.** The material of the window glass pane is the same as for  
 462 the wall (C006),
- 463 – **Specular windows.** The material of the window glass pane is soda lime  
 464 silica glass. The spectral complex refractive index is taken from Rubin  
 465 (1985) and is used by HTRDR-Urban to calculate the directional and spec-  
 466 tral specular reflectivity,
- 467 – **Lambertian windows.** The window glass pane is made of a hypotheti-  
 468 cal Lambertian material with an effective broadband reflectivity, which is  
 469 calculated for each urban morphology and  $\gamma$  as a function of the incident  
 470 ( $\dot{I}_{win,spec}$ ) and absorbed ( $\dot{Q}_{win,spec}$ ) solar radiation from the **Specular**  
 471 **windows** case:

$$\alpha_{win,Lam}(LCZ,\gamma) = 1 - \frac{\dot{Q}_{win,spec}(LCZ,\gamma)}{\dot{I}_{win,spec}(LCZ,\gamma)}. \quad (14)$$

472 For the specular windows simulations, a large value of  $N_{zen} = 5 \times 10^8$  is used  
 473 because Caliot et al. (2022) found convergence problems in the MCM algorithm  
 474 due to the rare events of specular reflections of solar spectral irradiance.

## 475 5.5 Influence of the Participating Atmosphere in the Urban Canopy Layer

476 The influence of the participating atmosphere on the urban terrestrial radi-  
 477 ation budget is studied for all urban morphologies. All surfaces are made of  
 478 a grey Lambertian material with a broadband emissivity of 0.9. Four one-  
 479 dimensional clear-sky atmospheric profiles are considered: Tropical (TRO),  
 480 Mid-Latitude Summer (MLS), Mid-Latitude Winter (MLW), and Sub-Arctic  
 481 Winter (SAW). The radiation scheme of the European Centre for Medium-  
 482 range Weather Forecasts (ECMWF) (ECRAD, Hogan and Bozzo (2016)) is  
 483 used to calculate the atmospheric radiative properties for these profiles. The  
 484 near surface air temperature is 300 K, 294.2 K, 272.06 K, and 257.2 K for  
 485 TRO, MLS, MLW, and SAW, respectively. The skin surface temperature of  
 486 all urban facets is the same and is varied as a function of the near-surface air  
 487 temperature to obtain a desired difference between the skin surface tempera-  
 488 ture and the near-surface air temperature ( $\Delta T_{surf}$ ). Simulations are performed  
 489 for  $\Delta T_{surf} = -10$  K, 0 K, 10 K, 20 K, and 30 K. The MCM simulations are  
 490 performed once with the real atmospheric properties and once with the atmo-  
 491 spheric properties in the urban canopy layer set to vacuum ones. The value of  
 492  $N_{zen}$  is set to  $5 \times 10^5$ .

## 493 5.6 Influence of Urban Trees

494 MCM simulations of the solar and terrestrial radiation budgets are made for  
 495 the urban morphologies LCZ2a, LCZ4, LCZ5, and LCZ9 with and without

496 trees. For the solar (terrestrial) radiation, all urban surfaces including the trees  
 497 are made of Lambertian grey materials with a broadband albedo (emissivity) of  
 498 0.4 (0.9). For the solar radiation, the direct-only and diffusive-only downwelling  
 499 solar radiation boundary conditions are analysed. For the terrestrial radiation,  
 500 the one-dimensional atmospheric profile corresponds to the clear-sky MLS.  
 501 The value of  $\Delta T_{surf}$  is varied between -10 K, 0 K, 10 K, 20 K, and 30 K and  
 502 is applied to all materials, except for the leaves. For these, the skin surface  
 503 temperature is assumed to be equal to the air temperature.  $N_{zen}$  is  $10^6$ .

## 504 5.7 Influence of Urban Fog

505 The solar and terrestrial radiation budgets are simulated for the urban mor-  
 506 phologies LCZ2a, LCZ4, LCZ5, and LCZ9 for different densities of urban fog.  
 507 For the solar (terrestrial) radiation, all surfaces are made of Lambertian grey  
 508 materials with a broadband albedo of 0.3 (0.9). The atmospheric profile at  
 509 altitudes above 130 m a.g.l. corresponds to the clear-sky MLS. Below 130 m  
 510 a.g.l., there is a layer of fog with a homogeneous liquid water mixing ratio.  
 511 Simulations with different values of the mixing ratio (0.05, 0.1, 0.2, 0.5, and  
 512 1 g kg<sup>-1</sup>) are performed. A case without fog is also simulated. The value of  
 513  $N_{zen}$  is set to  $10^6$ .

## 514 6 Results

### 515 6.1 Simplification of Urban Morphology

516 Figure 3 shows the results for the direct-only urban radiation budget in LCZ1.  
 517 Results for the other morphologies are shown in the supplementary Figs. 17-32.  
 518 The results for the sparsely-built low-rise LCZ9 geometry, the dense mid-rise  
 519 LCZ2a, and the dense high-rise LCZ1 are discussed in detail, while the results  
 520 for the other morphologies are summarised.

521 For the LCZ9 morphology with flat roofs (Fig. 17), there is no difference of  $\dot{q}_R$   
 522 between the real morphology and the simplified ones for  $\gamma$  above  $20^\circ$ . For lower  
 523  $\gamma$ , the absorption by the flat roofs is lower for the real morphology than for the  
 524 simplified morphologies, which is due to shading. The normalised upwelling solar  
 525 radiative flux  $\dot{q}_U$  is exactly 0.3 for the corresponding flat ground geometry  
 526 because there is no shading. For the other morphologies, due to multiple reflec-  
 527 tions,  $\dot{q}_U$  is less than 0.3 and tends to decrease with  $\gamma$ . The differences between  
 528 the results obtained with the real urban morphology and the representative  
 529 street canyon or regular blocks are small.  $\dot{q}_F$  is low for high  $\gamma$  and increases  
 530 with lower  $\gamma$  as more radiation illuminates the facades. For  $\gamma$  values below  $20^\circ$ ,  
 531  $\dot{q}_F$  is slightly lower for the real morphology than for the simplified morpholo-  
 532 gies. This is due to the distance between buildings and the layout design of  
 533 the real morphologies. In fact, as shown in Fig. 2, for realistic morphologies,  
 534 buildings can be closer to each other than for the street canyon and regular

535 block geometries, for which there is a minimum distance between buildings.  
 536 In addition, the realistic layout includes large roads and central squares that  
 537 allow the sun's rays to reach the ground. This is expected to result in more  
 538 shading from one building onto the facade of another in realistic morphol-  
 539 ogy results, whereas for the simplified morphologies, the minimum distance  
 540 between the buildings (e.g., street canyon width) limits shading and leads to  
 541 higher  $\dot{q}_F$  compared to the real morphology. This mechanism affects also  $\dot{q}_G$ ,  
 542 which has a higher value for the realistic morphologies due to the aggregation  
 543 of buildings, which allows the ground to absorb more direct solar radiation in  
 544 unshaded streets and central squares.

545 For LCZ9 with pitched roofs (Fig. 18),  $\dot{q}_R$  is higher for the real morphology  
 546 than for the simplified morphologies (with flat roofs) for  $\gamma$  below  $30^\circ$ .  $\dot{q}_F$  is  
 547 also lower because the pitched roofs of the real morphology intercept more  
 548 solar radiation than the flat roofs of the simplified morphologies. For  $\gamma$  below  
 549  $30^\circ$ , the urban solar radiation budget is strongly different between the LCZ9  
 550 with flat and pitched roofs.

551 For LCZ2a with pitched roofs (Fig. 19),  $\dot{q}_R$  is lower for the simplified mor-  
 552 phologies than for the real morphology; the underestimation increases with  
 553 lower  $\gamma$  and reaches 25% for  $\gamma = 1^\circ$ . Thus,  $\dot{q}_F$  is overestimated by the simpli-  
 554 fied morphologies.  $\dot{q}_U$  is slightly higher for the simplified morphologies than  
 555 for the real morphologies for  $\gamma$  below  $45^\circ$  and is only slightly different above.

556 For LCZ2a with flat roofs (Fig. 20),  $\dot{q}_R$  is considerably lower and  $\dot{q}_F$  higher  
 557 for lower solar elevation angle compared to LCZ2a with pitched roofs, while  
 558  $\dot{q}_U$  and  $\dot{q}_G$  do not differ much between the flat and pitched roof morphologies.

559 For LCZ1 (Fig. 3), the simplified urban morphologies with uniform building  
 560 height overestimate  $\dot{q}_R$  for  $\gamma$  below  $75^\circ$  because in the real morphology the  
 561 heterogeneity of building heights leads to shading of the roofs. The overesti-  
 562 mation is 30% for  $\gamma = 45^\circ$  and increases to 400% for  $\gamma = 1^\circ$ . Thus, street  
 563 canyon and block morphologies overestimate  $\dot{q}_U$  by 10% for  $\gamma = 45^\circ$  and up to  
 564 25% for  $\gamma = 1^\circ$  because too much radiation is reflected off the roof to the sky.  
 565 In addition,  $\dot{q}_F$  is underestimated by the street canyon and block morpholo-  
 566 gies for  $\gamma$  below  $50^\circ$ , which is due to the overestimation of  $\dot{q}_R$  and  $\dot{q}_U$ . For  $\gamma$   
 567 above  $50^\circ$ ,  $\dot{q}_F$  is overestimated by the street canyon and block morphologies  
 568 due to the greater distance between building facades compared to the realistic  
 569 morphology, which underestimates shading between buildings.  $\dot{q}_G$  is underes-  
 570 timated by the simplified morphologies for all solar elevation angles.

571 The overall results for the other urban morphologies show that  $\dot{q}_F$  is overesti-  
 572 mated by the infinitely-long street canyon and regular block morphologies for  
 573 a range of  $\gamma$  that depends on the morphologies'  $\lambda_p$  and  $H_{mean}$ . For the mid-rise  
 574 morphologies LCZ2b (Figs. 21-22), LCZ5 (Figs. 23-24), and LCZ10 (Fig. 25),  
 575 the overestimation of  $\dot{q}_F$  is found for  $\gamma$  between  $20^\circ$  and  $50^\circ$ . For the low-rise  
 576 morphologies LCZ3 (Fig. 26), LCZ6a (Figs. 27-28), LCZ6b (Figs. 29-30), and  
 577 LCZ8 (Fig. 31),  $\dot{q}_F$  is overestimated for  $\gamma$  between  $5^\circ$  and  $30^\circ$ , and for the  
 578 high-rise LCZ4 (Fig. 32) it is overestimated for  $\gamma$  between  $20^\circ$  and  $70^\circ$ . This  
 579 is due to the fact that the higher and denser the urban morphology, the more  
 580 shadow is cast by a given building on the facades of other buildings, even for

581 high values of  $\gamma$ . This shading is systematically underestimated by the sim-  
 582 plified morphologies resulting in too high values of  $\dot{q}_F$ . The uncertainties in  
 583  $\dot{q}_G$  are complementary to those of  $\dot{q}_F$ , i.e. they are underestimated in similar  
 584 ranges of  $\gamma$  than  $\dot{q}_F$  is overestimated. For low values of  $\gamma$ , the results for the  
 585 flat roof and the corresponding pitched roof morphology are very different.  
 586 For the flat roof,  $\dot{q}_R$  decreases for lower  $\gamma$  while it increases for the pitched  
 587 roof morphology. As a complement,  $\dot{q}_F$  increases for lower  $\gamma$  for the flat roof  
 588 morphology and decreases for the pitched roof morphology. The street canyon  
 589 and regular block morphologies have in common that  $\dot{q}_R$  does not depend on  
 590  $\gamma$ , so they can neither represent the shading of higher buildings on the roofs  
 591 of lower buildings, nor the potential effect of the pitched roofs. The effective  
 592 urban albedo ( $\dot{q}_U$ ) is the parameter that is the least affected by the simplifi-  
 593 cation of urban morphology.

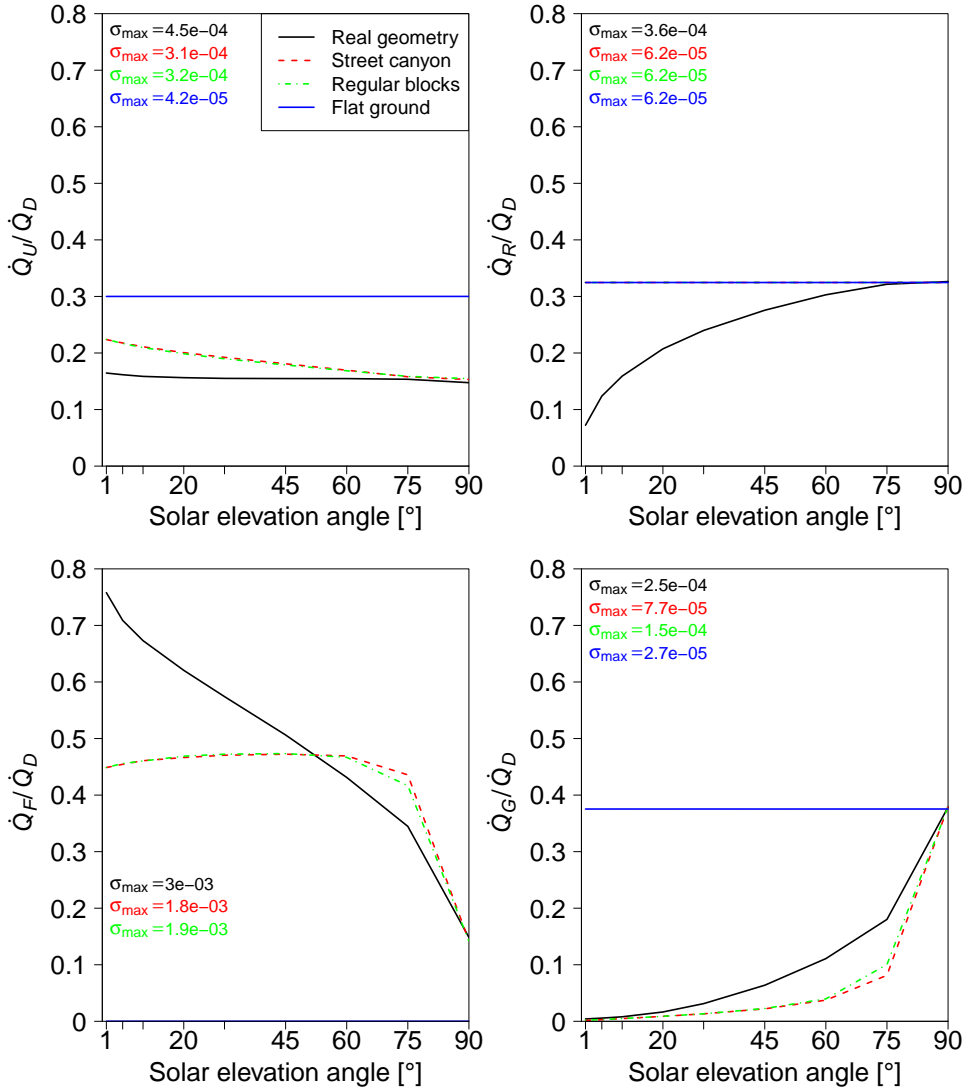
594 Figure 4 shows the radiation budget of LCZ2a and LCZ9 districts with flat and  
 595 pitched roofs for diffusive-only downwelling solar radiation. The results for the  
 596 other morphologies are shown in supplementary Figs. 33-35. The results are  
 597 mainly similar to those for the direct-only solar radiation averaged for all val-  
 598 ues of  $\gamma$ . For example, for LCZ1 and direct-only downwelling solar radiation,  
 599  $\dot{q}_G$  is underestimated for all values of  $\gamma$  when using the infinitely-long street  
 600 canyon and regular block morphologies. As a consequence,  $\dot{q}_G$  is also underes-  
 601 timated for the diffusive-only downwelling solar radiation. For other radiative  
 602 observables and morphologies, errors of different sign for different values of  $\gamma$   
 603 are partly compensated for. Therefore, the results for the diffusive-only solar  
 604 radiation are less affected by the simplification of the urban morphology than  
 605 those for the direct-only solar radiation.

606

## 607 6.2 Influence of Spectrally-reflecting Materials

608 The differences in the simulated solar radiation budget between the morpholo-  
 609 gies with spectrally-reflecting and broadband materials tend to be small. For  
 610 direct-only downwelling solar radiation and low-rise morphologies, the relative  
 611 differences are less than 0.8%. For the mid-rise morphologies they are below  
 612 1%, except for LCZ2a where they reach 2% for  $\dot{q}_U$  and  $\dot{q}_G$ . Figure 5 shows  
 613 the results for LCZ1 where the largest differences are found. For LCZ1 with  
 614 spectrally-reflecting materials,  $\dot{q}_U$  is up to 2% lower than for LCZ1 with broad-  
 615 band materials, while  $\dot{q}_F$  is up to 2% higher. For diffusive-only downwelling  
 616 solar radiation, the differences in results between the spectral and broadband  
 617 materials are very small. The largest relative uncertainty of 1.3% is found for  
 618 LCZ1 (not shown).

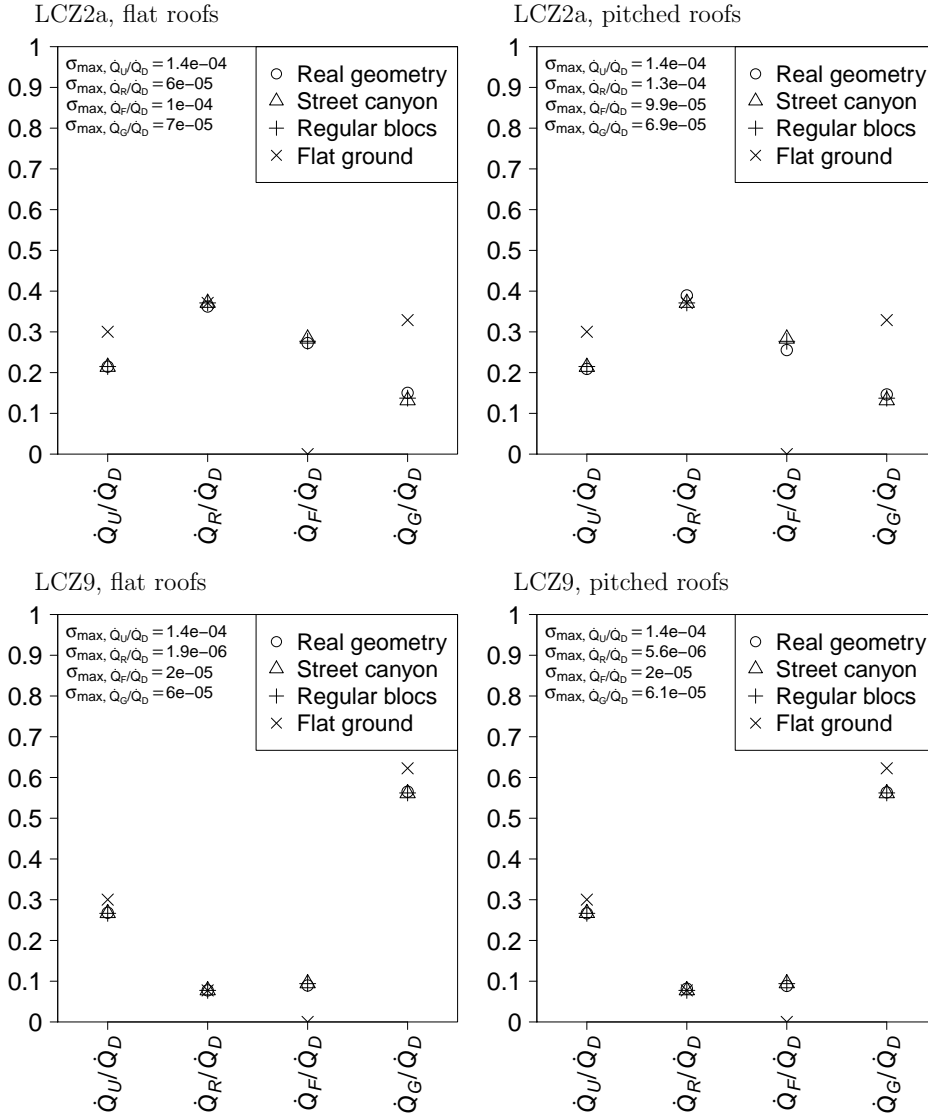
619



**Fig. 3** Effect of urban morphology simplifications on the urban, roof, facade, and ground solar radiation budgets for direct-only downwelling solar radiation and the LCZ1 morphology. The values of  $\sigma_{max}$  indicate the maximum value of the standard deviation of the radiative observable obtained from the MCM simulations for all values of  $\gamma$

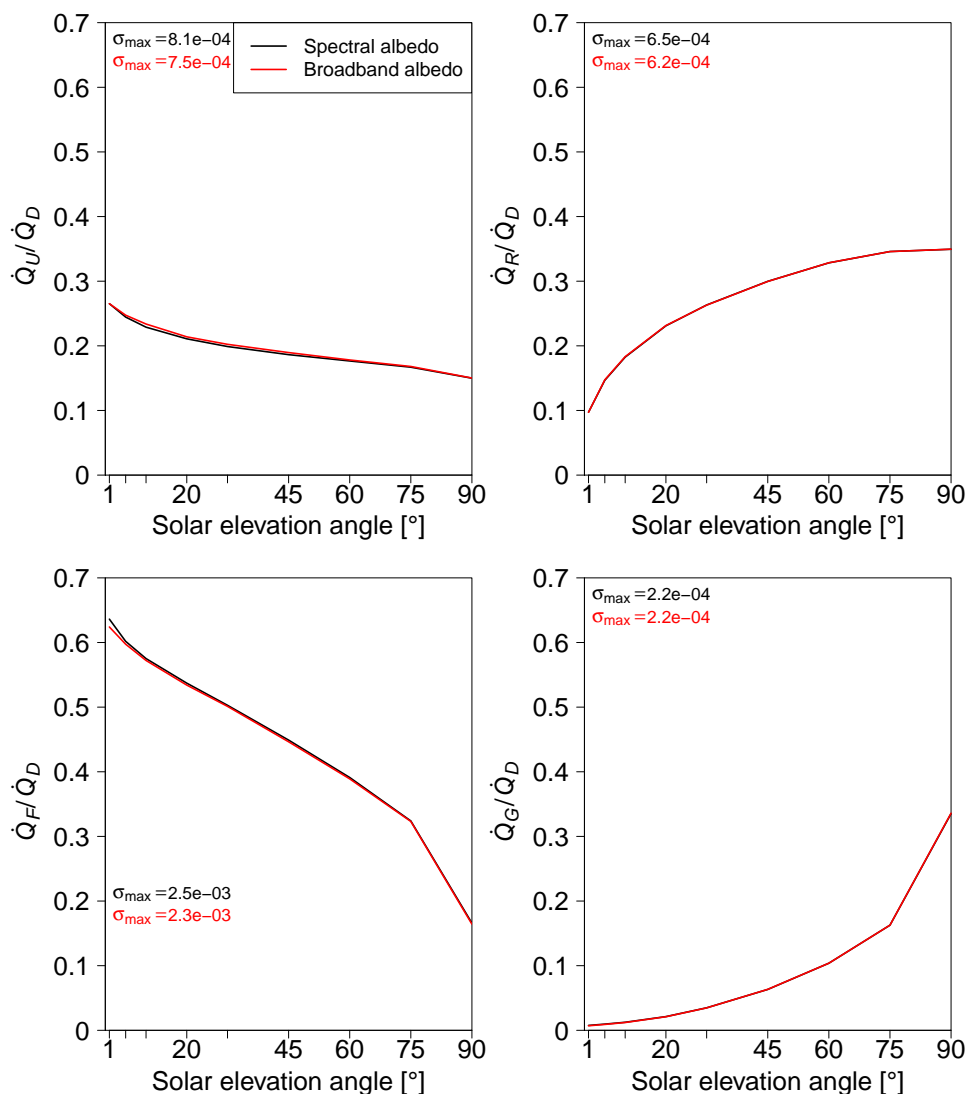
### 620 6.3 Influence of Specular Reflections by Windows

621 The Tab. 4 shows the values of the effective broadband window glass pane  
 622 albedo ( $\alpha_{win,Lam}$ ) calculated according to Eq. 14 for each urban morphology  
 623 and  $\gamma$ . The values are low (between 0.06 and 0.1) for  $\gamma$  between 1° and 45°.



**Fig. 4** Effect of urban morphology simplifications on the urban, roof, facade, and ground solar radiation budgets of selected morphologies and for diffusive-only downwelling solar radiation

624 This is due to the high angle of incidence of direct solar radiation on the  
 625 windows. For  $\gamma$  equal to  $60^\circ$  and  $75^\circ$ ,  $\alpha_{win,Lam}$  is higher (up to 0.28 for  $\gamma =$   
 626  $75^\circ$  and the CBD morphology), which is due to the lower angle of incidence  
 627 of direct solar radiation on the windows. For  $\gamma = 90^\circ$ , no direct solar radia-  
 628 tion reaches the windows. Therefore, the values of  $\alpha_{win,Lam}$  are lower (0.09 to



**Fig. 5** Impact of spectrally-reflecting urban materials on the urban, roof, facade, and ground solar radiation budgets for direct-only downwelling solar radiation and the realistic LCZ1 morphology

629 0.11).

630 Figure 6 shows the urban solar radiation budget of the CBD for clear-sky  
 631 conditions, and the results for the other morphologies are shown in supple-  
 632 mentary Figs. 36-38. For all morphologies, consideration of windows leads to  
 633 a decrease in  $\dot{q}_U$  and an increase in  $\dot{q}_F$ . This is due to the low albedo of the  
 634 window compared to the C006 wall material. The values of  $\dot{q}_R$  and  $\dot{q}_G$  are less



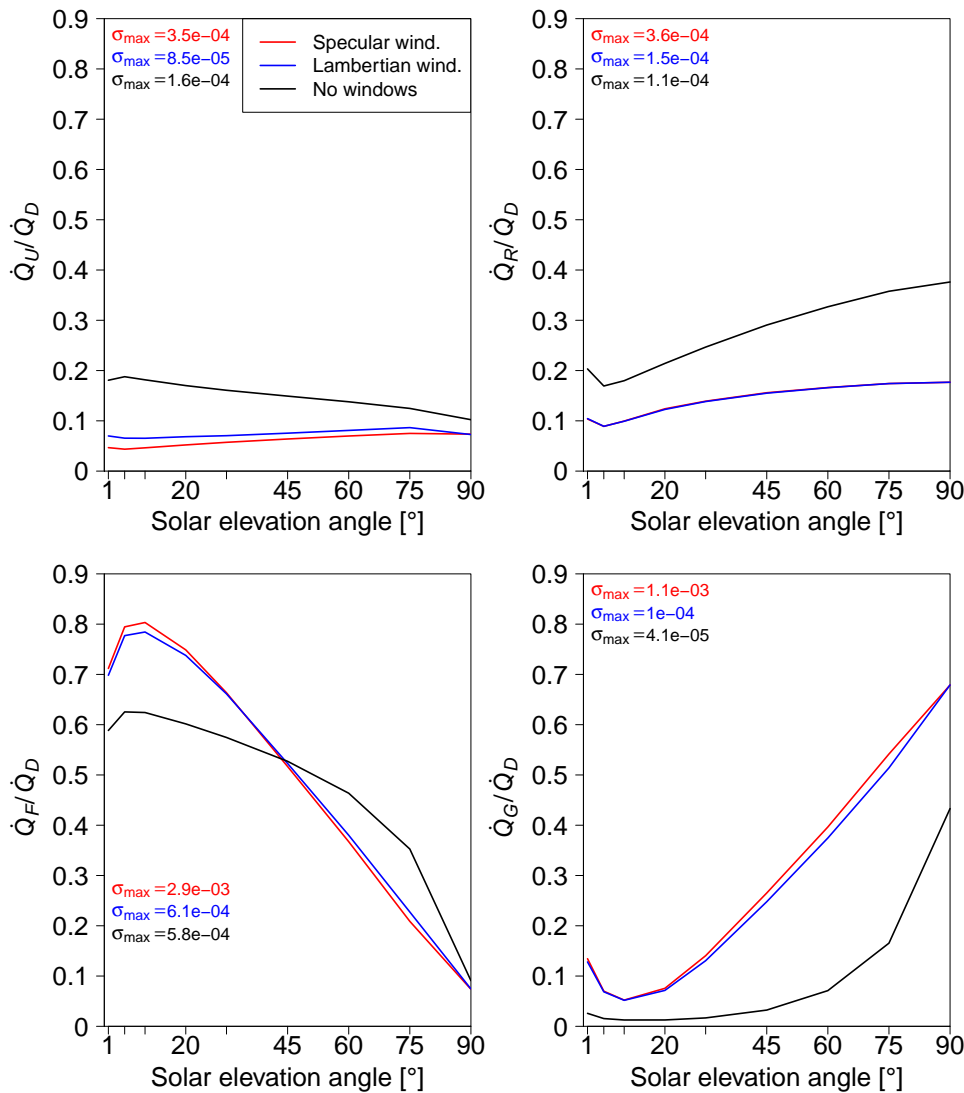
**Table 4** Effective broadband Lambertian albedo of windows

$\gamma$ [°]	1	5	10	20	30	45	60	75	90
LCZ1	0.08	0.08	0.07	0.06	0.08	0.09	0.12	0.19	0.09
LCZ2a	0.08	0.07	0.08	0.08	0.08	0.09	0.13	0.21	0.09
LCZ9	0.06	0.07	0.07	0.07	0.07	0.09	0.12	0.18	0.08
CBD	0.10	0.08	0.08	0.08	0.09	0.11	0.16	0.28	0.11

635 affected by the presence of windows, except for the CBD with its very high  
636 glazing ratio ( $f_g = 0.9$ ). Specularly-reflecting windows lead to a lower  $\dot{q}_U$  than  
637 Lambertian windows, except for  $\gamma = 90^\circ$ , where almost no direct solar radi-  
638 ation reaches the windows. The reason for this is that the specularly-reflected  
639 solar radiation propagates downwards whereas the diffusively-reflected solar  
640 radiation is travels upwards or downwards with the same probability.  $\dot{q}_F$  and  
641  $\dot{q}_G$  are slightly higher for the specularly-reflecting windows. For the morpholo-  
642 gies with normal glazing ratio ( $f_g = 0.3$ ), the relative differences between the  
643 results for specular and Lambertian windows are small (1.5% for LCZ9, 1.3%  
644 for LCZ2a, and 3% for LCZ1). Only for CBD with  $f_g = 0.9$ , the differences  
645 are larger (e.g.,  $\dot{q}_U$  is 10% to 50% lower for specularly-reflecting windows).

#### 646 6.4 Influence of Participating Atmosphere in the Urban Canopy Layer

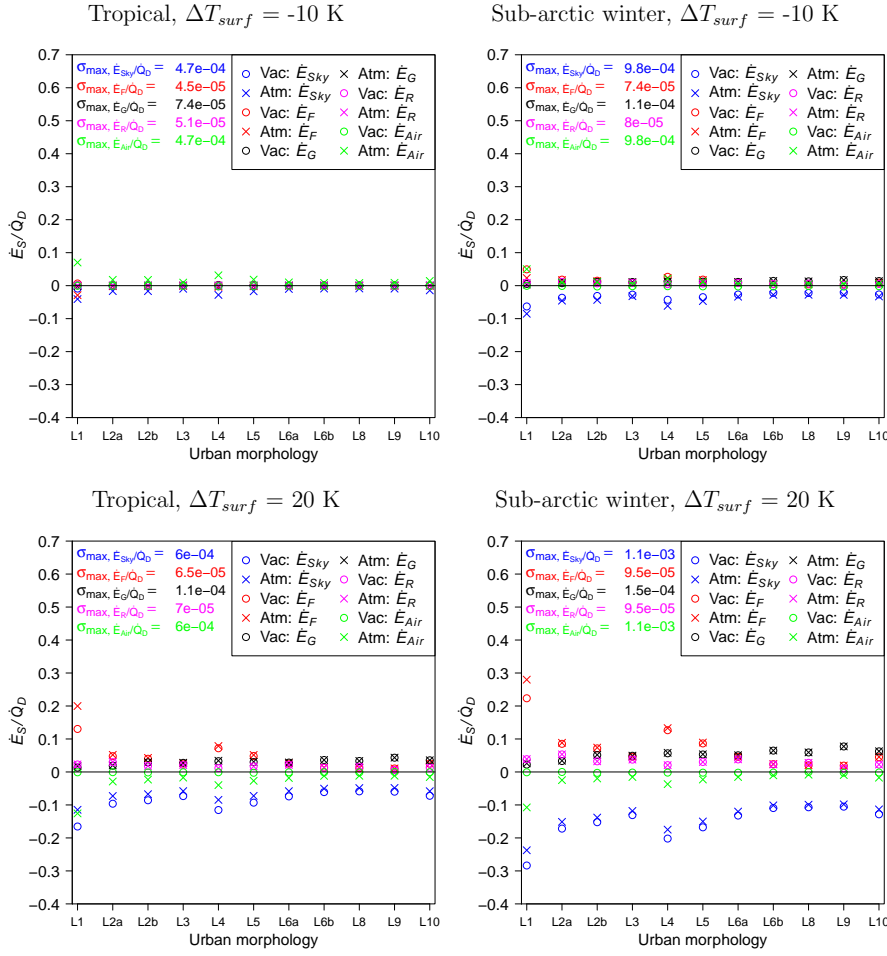
647 Figure 7 shows the urban terrestrial radiation budget with participating atmo-  
648 sphere in the urban canopy layer (Atm case) and without (Vac case) for the  
649 warmest (TRO) and the coldest (SAW) atmospheric profiles and  $\Delta T_{surf} =$   
650  $-10$  K or  $+20$  K. The other results are shown in the supplementary Figs. 39-  
651 41. The differences in the terrestrial urban radiation budget between the Vac  
652 and Atm cases tend to be larger for those urban morphologies with large build-  
653 ing height (LCZ1 and LCZ4) and are also strongly dependent on the  $\Delta T_{surf}$ .  
654 When urban surfaces are 10 K colder than the air temperature,  $\dot{E}_{sky}$  is less  
655 negative for Atm than for Vac, because the warmer air emits more radiation  
656 towards the sky than the colder urban surfaces.  $\dot{E}_{sky}$  is also more negative  
657 for SAW than for TRO because there is less participation of the colder SAW  
658 air than of the warmer TRO air. For  $\Delta T_{surf} = 0$  K, the differences between  
659 Atm and Vac are small, which is not surprising. When the urban skin surface  
660 temperature is higher than the air temperature,  $\dot{E}_{sky}$  is less negative for Atm  
661 than for Vac because some of the radiation emitted by the warm urban sur-  
662 faces is absorbed by the cold air in the UCL and therefore does not reach the  
663 atmosphere above the urban canopy layer. The values of  $\dot{E}_{sky}$  are more nega-  
664 tive for the SAW profile than for the TRO profile, because the cold SAW air  
665 participates less in radiative exchange than the warm TRO air.  $\dot{E}_F$  is higher  
666 for Atm than for Vac because the cold air between the facades absorbs part  
667 of the radiation emitted by the facades leading to a lower value of incident  
668 terrestrial radiation at the facades. The differences in  $\dot{E}_R$  and  $\dot{E}_G$  between the  
669 Vac and Atm cases remain small, even for the highest  $\Delta T_{surf}$  of 30 K.  
670



**Fig. 6** Effect of (specularly-reflecting) windows on the urban, roof, facade, and ground solar radiation budget for clear-sky conditions and the realistic CBD morphology

671 6.5 Influence of Urban Trees

672 Figure 8 shows the urban solar radiation budget of LCZ9 for the direct-only  
 673 downwelling solar radiation with and without trees. Results for LCZ2a, LCZ4,  
 674 and LCZ5 are shown in the supplementary Figs. 42-44. For the sparsely-built  
 675 LCZ9 with  $H_{mean} = 5.9$  m, the trees are almost twice as high as the buildings  
 676 and therefore strongly modify the solar radiation budget. For  $\gamma$  below  $10^\circ$ , the



**Fig. 7** Terrestrial radiation exchanged by the sky, the roofs, the facades, the ground, and the air in the urban canopy layer for clear-sky tropical and sub-arctic winter atmosphere with (Atm) and without (Vac) participating atmosphere in the urban canopy layer. The names of the realistic LCZ morphologies are abbreviated: L1 is LCZ1, etc.

677 trees cast shade on the roofs, leading to a large reduction in  $\dot{q}_R$ . For  $\gamma$  above  
 678  $45^\circ$ , the trees absorb ( $\dot{q}_T$ ) about 10% of the downwelling solar radiation, and  
 679 this fraction increases to more than 50% for a  $\gamma$  of  $1^\circ$ . The radiation absorbed  
 680 by the trees does not reach the facades (mainly for low  $\gamma$ ) or the ground (mainly  
 681 for high  $\gamma$ ). The presence of trees lowers  $\dot{q}_U$  due to the multiple reflections by  
 682 the leaves. For LCZ5, the buildings are taller than the trees, so the trees do not  
 683 change the  $\dot{q}_R$ . The fraction of solar radiation absorbed by the trees decreases  
 684 for  $\gamma$  below  $10^\circ$  because the buildings shade the trees. The trees slightly reduce  
 685  $\dot{q}_F$  and  $\dot{q}_G$  for all values of  $\gamma$ . For the denser LCZ2a and the open high-rise  
 686 LCZ4, the main results are similar to those for LCZ5.

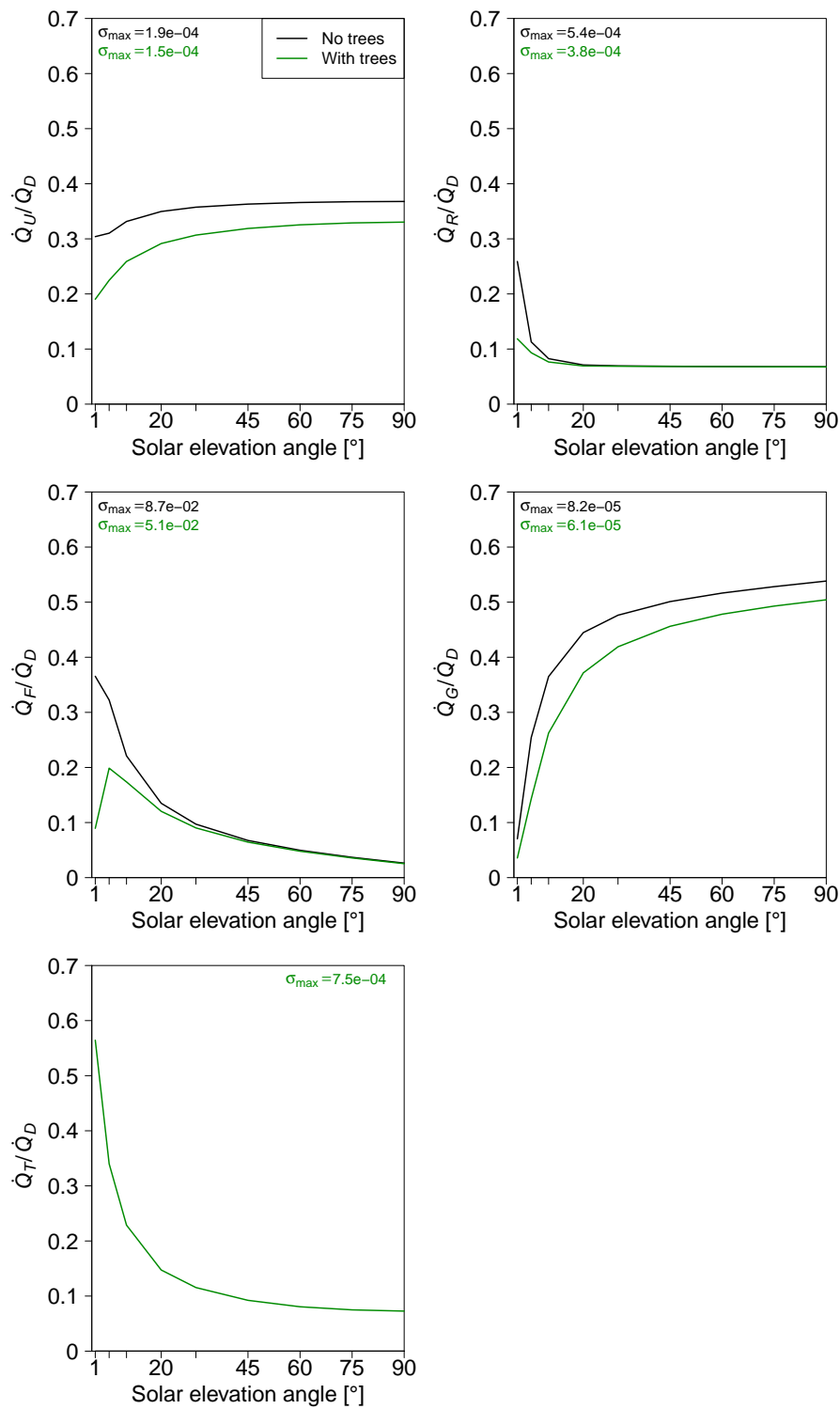
687 For diffusive-only downwelling solar radiation (Fig. 9), the presence of trees  
 688 has no effect on  $\dot{q}_R$  for LCZ9, contrary to the result for direct-only downwelling  
 689 solar radiation. The other results are similar to those for direct-only radiation.  
 690 The trees reduce  $\dot{q}_F$ ,  $\dot{q}_G$ , and  $\dot{q}_U$  except for LCZ2a, for which they do not have  
 691 sufficient influence.

692 The influence of trees on the urban terrestrial radiation budget is shown in  
 693 Fig. 10. The trees do not change the radiative observables much, the only  
 694 exception being  $\dot{E}_{sky}$ , which is lower when trees are present, as the urban  
 695 morphology with trees has a higher total surface area resulting in a higher  
 696 effective emissivity.

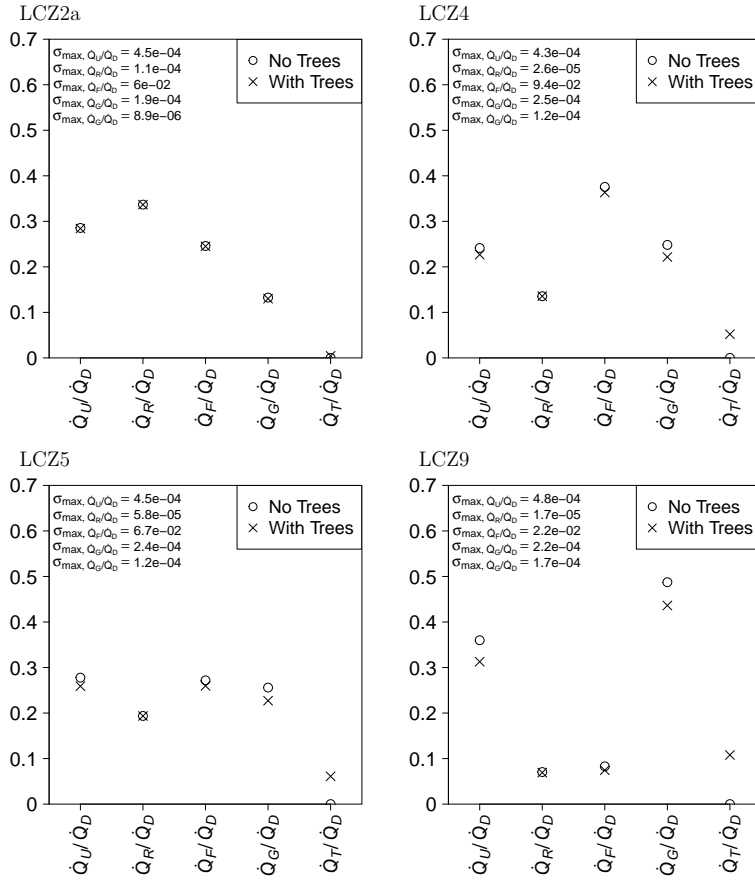
697 Figure 11 shows a  $1\text{ m} \times 1\text{ m}$  resolution map of MRT for the LCZ9 district with  
 698 and without trees. The top row shows the MRT calculated with the solar and  
 699 terrestrial radiation contributions ( $\gamma = 30^\circ$ , the solar azimuth angle is  $292.5^\circ$   
 700 from north, clockwise) and the skin surface temperature of all urban facets  
 701 including the trees is 304.2 K. The bottom row shows the MRT calculated  
 702 with only the terrestrial radiation contribution (nighttime conditions). During  
 703 the day, the MRT is between 49 and  $57^\circ\text{C}$  in the sunlit areas far from buildings,  
 704 between 17 and  $25^\circ\text{C}$  in the areas shaded by buildings, and up to  $62^\circ\text{C}$  near  
 705 the sunlit building walls, which is due to the solar radiation reflected by the  
 706 building walls. The trees lead to a strong MRT reduction of 10 K in the  
 707 partially-shaded areas and 30 K in the fully-shaded areas. Considering that the  
 708 sensitivity of human thermal comfort indices to MRT is about 0.25 (Schoetter  
 709 et al. 2013), they would be about 7 to 8 K lower in the fully shaded areas.  
 710 For the night conditions, MRT is mainly between 13 and  $15^\circ\text{C}$  with only  
 711 little spatial variation. Trees lead to slightly higher MRT (between 2 and 4 K  
 712 higher), because they emit more terrestrial radiation than the downwelling  
 713 terrestrial radiation from the sky that is occulted by the trees.

## 714 6.6 Influence of Urban Fog

715 The urban solar radiation budget for different liquid water mixing ratios of  
 716 urban fog is shown in Fig. 12 for LCZ4 and in the supplementary Figs. 45-47  
 717 for LCZ2a, LCZ5, and LCZ9. The denser the urban fog, the more  $\dot{q}_U$  increases  
 718 and the less it depends on  $\gamma$ . This is because in very dense urban fog, most of  
 719 the downwelling solar radiation is reflected by the fog layer before it reaches  
 720 the urban facets. For LCZ9, LCZ5, and LCZ2a,  $\dot{q}_R$  is reduced in the presence  
 721 of urban fog, because the fog reflects and absorbs a part of the downwelling  
 722 solar radiation before it can reach the roofs of buildings. For LCZ4 and low  
 723 values of  $\gamma$ ,  $\dot{q}_R$  is increased in the presence of urban fog. This is because, under  
 724 clear-sky conditions, some roofs of the LCZ4 morphology are shaded, whereas  
 725 in the presence of fog, there is more diffuse solar radiation and more of the  
 726 downwelling radiation at the roof level is actually absorbed by the roofs. For  
 727 clear-sky conditions,  $\dot{q}_F$  is strongly dependent on  $\gamma$ . This is no longer the case  
 728 in the presence of urban fog. Compared to clear-sky conditions, urban fog  
 729 leads to a lower  $\dot{q}_F$  for low  $\gamma$  and a higher  $\dot{q}_F$  for higher  $\gamma$  because less direct

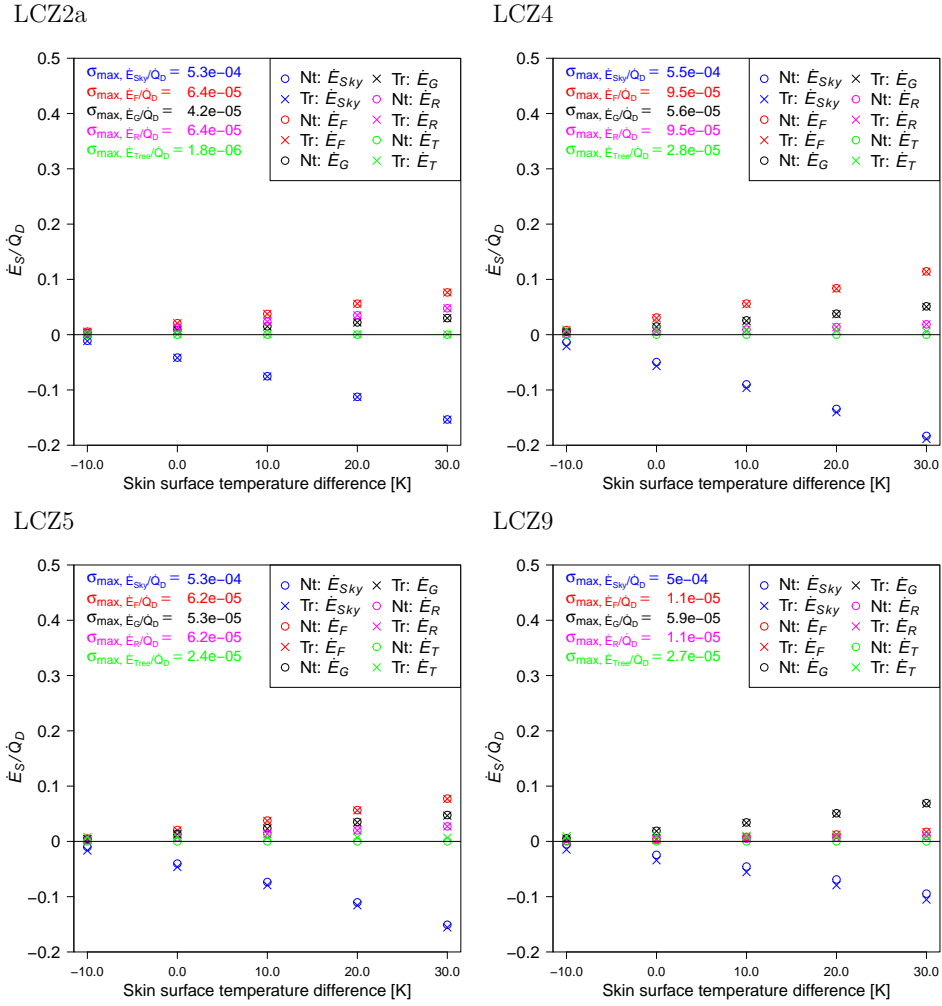


**Fig. 8** Effect of trees on the urban, roof, facade, ground, and tree solar radiation budgets for direct-only downwelling solar radiation and the realistic LCZ9 morphology



**Fig. 9** Effect of trees on the urban, roof, facade, ground, and tree solar radiation budgets for diffusive-only downwelling solar radiation for the realistic LCZ2a, LCZ4, LCZ5, and LCZ9 morphologies

730 downwelling solar radiation reaches the urban facets. In the presence of urban  
 731 fog,  $\dot{q}_G$  increases with the solar elevation angle ( $\gamma$ ).  
 732 Figure 13 displays the effect of fog on the terrestrial urban radiation budget  
 733 for LCZ4 and supplementary Figs. 48-50 for LCZ2a, LCZ5, and LCZ9. For the  
 734 clear-sky conditions, the urban area emits radiation towards the sky ( $\dot{E}_{Sky}$   
 735 is negative) and more radiation is emitted with increasing  $\Delta T_{surf}$ . In the presence  
 736 of urban fog, the urban terrestrial radiation budget is markedly changed.  
 737 The denser the urban fog, the less radiation is exchanged with the sky. For an  
 738 urban fog with a density of  $0.5 \text{ g kg}^{-1}$  or higher, only very little radiation is  
 739 exchanged between the urban surfaces and the sky. The emission from roofs,  
 740 facades, and ground still increases with increasing  $\Delta T_{surf}$ , but the value of  
 741 the emission is lower because there is almost no emission to the sky. Instead,  
 742 the urban facets exchange radiation with the urban fog.

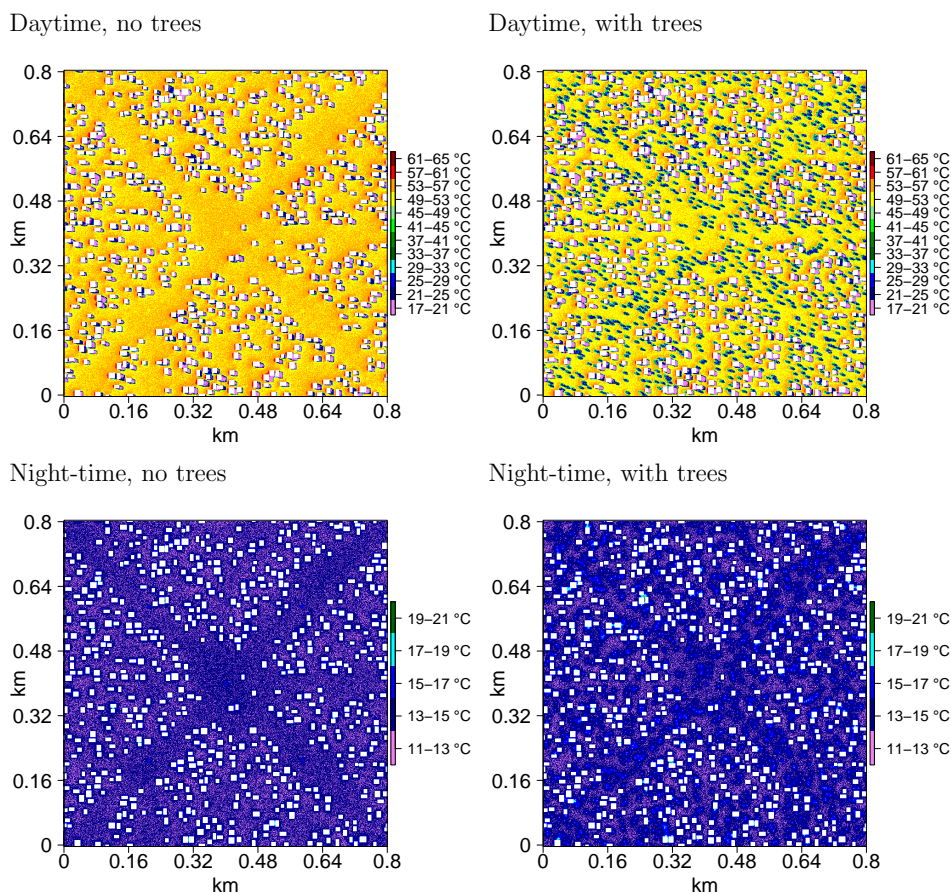


**Fig. 10** Effect of trees on the longwave radiation exchanged by the sky, the roofs, the facades, the ground, and the trees for the realistic LCZ2a, LCZ4, LCZ5, and LCZ9 morphologies. In the legend,  $Tr$  denotes the urban district with trees (cross),  $Nt$  the urban district without trees (circle)

## 743 7 Discussion

744 The main findings obtained of the MCM-based sensitivity studies are as follows:  
745

- 746 – The simplified urban morphologies infinitely-long street canyon and regular  
747 square blocks, which are very often used in urban canopy models, lead to a  
748 systematic overestimation (underestimation) of the fraction of direct solar  
749 radiation absorbed by the building facades (the ground). This is because

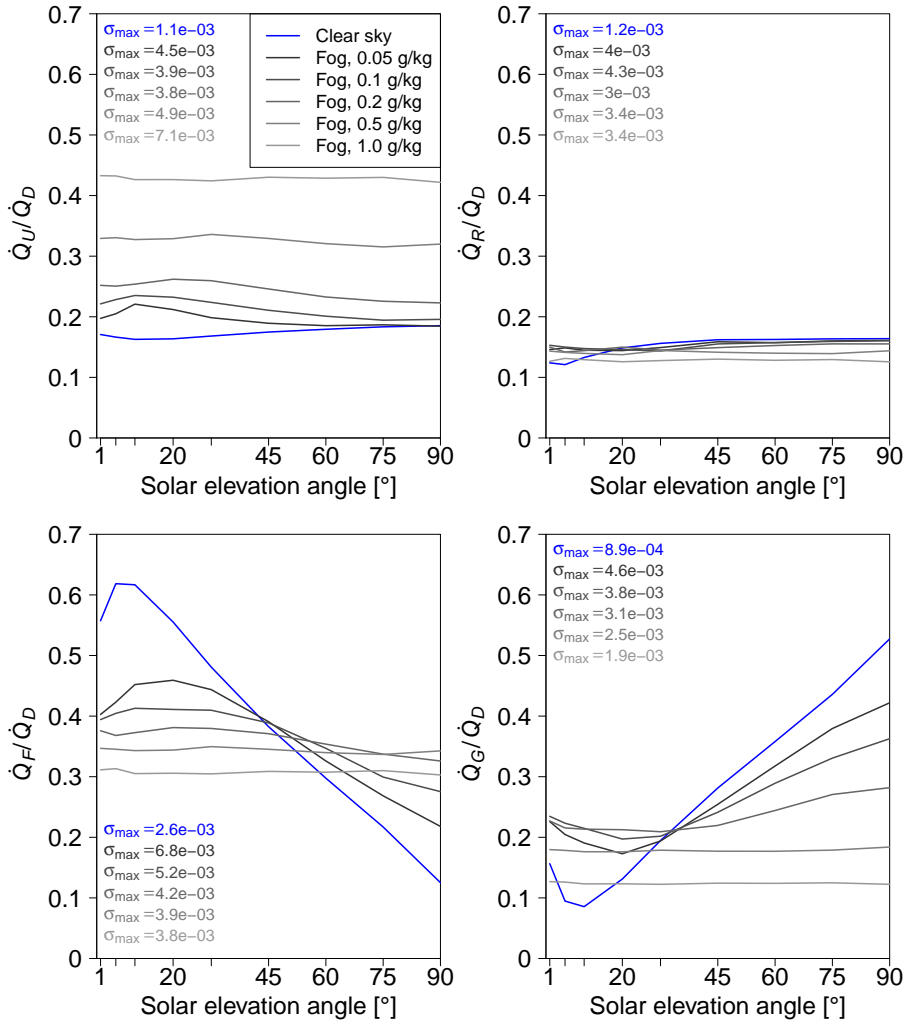


**Fig. 11** Map at 1 m resolution of the daytime and night-time MRT of a realistic LCZ9 morphology with and without trees. The solar elevation angle is  $30^\circ$  and the solar azimuth angle is  $292.5^\circ$  from north clockwise. The areas covered by buildings are white

750 these morphologies cannot represent buildings that are closer to each other  
 751 than the width of the street canyon or the distance between the square  
 752 blocks. For mid- and high-rise urban morphologies, the uncertainty in the  
 753 radiation absorbed by the facades can be more than 10% of the downwelling  
 754 direct solar radiation. As a consequence, the partitioning of the surface-  
 755 atmosphere exchanges between the building envelope and the ground is  
 756 incorrect, which can affect the results of urban canopy models.

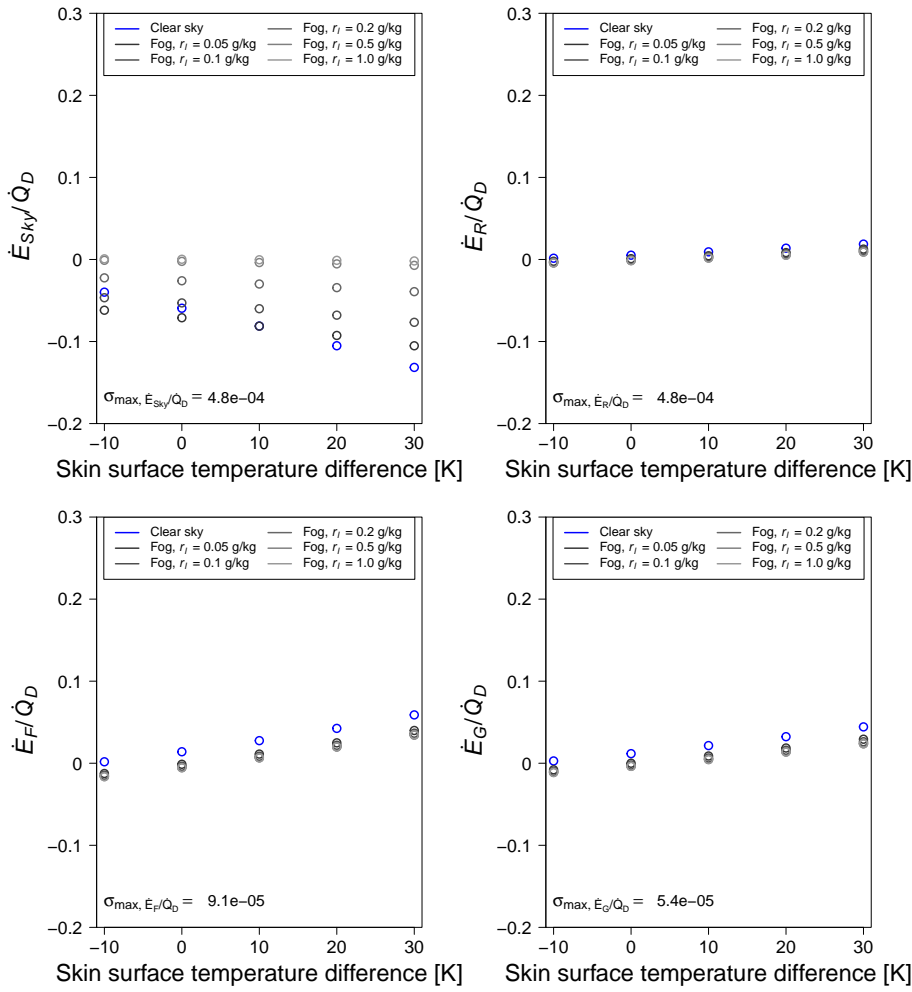
757 – There is only little difference between the results obtained for the infinitely-  
 758 long street canyon and the regular array of square block morphologies. An  
 759 interesting point is that the square blocks do not perform better than  
 760 the infinitely-long street canyon for urban morphologies such as LCZ4 or  
 761 LCZ9, which are more like blocks than like canyons. This is because for





**Fig. 12** Effect of fog on the urban, roof, facade, and ground direct solar radiation budget for the realistic LCZ4 morphology

- 762 both square blocks and street canyon, there is a minimum distance between  
 763 the geometric elements, which does not exist in a realistic morphology.  
 764 – Simplified morphologies that neglect the variety of building heights lead to  
 765 large uncertainties for the high-rise LCZ1 and LCZ4. Therefore, the use of  
 766 more sophisticated approaches is advised for the simulation of cities where  
 767 such morphologies are common (e.g., Asian megacities).  
 768 – The simplification of the urban morphology leads to greater uncertainties  
 769 when considering direct solar radiation compared to diffuse solar radiation.



**Fig. 13** Effect of fog on the terrestrial radiation exchanged by the sky, the roofs, the facades, and the ground for the realistic LCZ4 morphology

770 – At low angles of solar elevation, pitched roofs greatly alter the urban direct  
 771 solar radiation budget. With pitched roofs, more solar radiation is absorbed  
 772 by the roofs and less by the facades. As urban canopy models neglect  
 773 pitched roofs, this is a major source of uncertainty, especially in subarctic  
 774 regions where the solar elevation angle is typically low. This result has to be  
 775 modulated because the absolute values of downwelling solar radiation are  
 776 small at low solar elevation angles and therefore, large relative uncertainties  
 777 in the radiative observables may not lead to a large absolute uncertainty  
 778 in the simulated urban radiation budget.

- 779 – The effective city albedo is the parameter that is the least affected by  
780 the simplification of the urban morphology. Therefore, less sophisticated  
781 approaches to represent the city could be used if the focus is only on the  
782 effective city albedo for the coupling with the atmospheric model.
- 783 – The uncertainty in the urban solar radiation budget introduced by the  
784 use of broadband compared to spectral reflectivity of urban materials is  
785 small. Larger uncertainties may be found for radiative observables that are  
786 defined for a narrow band of the solar spectrum such as photosynthetically  
787 active radiation or ultraviolet radiation.
- 788 – Specular reflections from windows alter the urban solar radiation budget  
789 in a relevant manner only in the CBD district with a very high glazing  
790 ratio. The main reason for this is that the fraction of radiation that is  
791 reflected by windows is quite low (between 0.06 and 0.28 depending on  
792 solar elevation angle). Therefore, for the urban radiation budget, it does  
793 not make much difference whether the reflection is Lambertian or specular.  
794 The previous study by Aida and Gotoh (1982) found a large influence  
795 of specular reflections on urban albedo. This is because in their study,  
796 all urban surfaces were considered as specular reflectors, whereas in the  
797 present study, only the windows are specular reflectors. Effects of specular  
798 reflections may be greater for urban districts with specularly reflecting wall  
799 materials or window coatings with a higher albedo.
- 800 – The interaction between terrestrial radiation and clear air in the urban  
801 canopy layer strongly modifies the urban radiation budget. The higher the  
802 buildings, the more relevant the participating atmosphere becomes. For  
803 the high-rise LCZ1 and skin surface temperature 20 K higher than the air  
804 temperature, the radiation exchanged by the facades is almost a factor of  
805 two higher with the participating atmosphere than without. This could  
806 strongly change the energy balance of the building or the sensible heat flux  
807 from the facades to the atmosphere. Such findings are in line with those  
808 of Hogan (2019b). It is therefore problematic that urban canopy models  
809 usually do not take into account the participating atmosphere. In warmer  
810 and more humid climates where many high-rise megacities are located,  
811 the participating atmosphere has a greater effect than in colder or drier  
812 climates.
- 813 – Urban trees have a very large influence on the solar radiation budget if they  
814 are higher than the buildings. Therefore, urban canopy models including  
815 urban trees should be designed to be able to account for trees that are  
816 taller than the buildings.
- 817 – The presence of fog strongly alters both the solar and terrestrial radiation  
818 budgets of urban areas. Therefore it may be interesting to extend urban  
819 canopy models so that they can represent urban fog and aerosols.

820 Several systematic drawbacks and limitations of the present study need to be  
821 mentioned.

- 822 – Only idealised procedurally-generated urban morphologies have been in-  
823 vestigated. Although key morphology parameters such as  $\lambda_p$  and  $H_{mean}$

- 824 have been chosen to match the typical values for the LCZ given in Stewart  
825 and Oke (2012), there may be systematic differences between the idealised  
826 morphologies and real cities. This could be the  $p_{ww}$  and  $p_{wg}$ , the omission  
827 of overhanging roofs, balconies, etc..
- 828 – The urban morphologies studied are designed to represent one building  
829 type per district; the type of LCZ is clearly defined. In real cities, there are  
830 districts with a mix of building types, which has not been investigated in  
831 this study.
  - 832 – The effect of heterogeneous urban materials and skin surface temperature  
833 has not been investigated. For example, half of the roofs could be bright  
834 brick tiles and the other half dark slate, whereas an urban canopy model  
835 would only solve the urban energy balance using the most common material,  
836 or average the parameters.
  - 837 – The present study did not investigate the climatology of uncertainties of  
838 urban canopy models. For example, the uncertainty due to the neglect  
839 of pitched roofs, which was found for low solar elevation angles is more  
840 relevant for cities at high latitude than for tropical cities.
  - 841 – In the present study, the radiative observables have been averaged for all  
842 solar azimuth angles. In a real-world application, there is a specific position  
843 of the sun, but the urban canopy model may still be averaging all solar  
844 azimuths. This adds another uncertainty, which has not been quantified  
845 here.

## 846 8 Conclusion and Outlook

847 The present study has investigated the uncertainties of radiative transfer calculation  
848 in urban canopy models. Urban districts similar to the LCZ have been  
849 created using a procedural city generator. A reference MCM model of urban  
850 radiative transfer is used to quantify the uncertainties arising from simplifications  
851 of urban morphology and radiative transfer physics that are typically  
852 made in urban canopy models. These assume that the complex urban morphology  
853 can be represented by an infinitely-long street canyon or regular square  
854 blocks, that urban materials are broadband Lambertian reflectors, and that atmospheric  
855 participation in radiative exchange in the urban canopy layer can be neglected.  
856 The results of the present study allow one to identify some priorities  
857 for the future development of urban canopy models. For all urban morphologies,  
858 the street canyon and block geometries lead to a wrong partitioning of  
859 solar radiative energy between the facades and the ground, as they lead to  
860 a systematic underestimation of inter-building shading. Therefore, the urban  
861 geometry proposed by Hogan (2019a), which assumes an exponential distribution  
862 of  $p_{ww}$  and  $p_{wg}$  is promising. Pitched roofs should also be considered in  
863 future urban canopy models. The inclusion of a variety of building heights at  
864 grid-point scale is necessary for high-rise or very heterogeneous urban districts.  
865 Future urban canopy models should take into account the participating atmosphere  
866 in the urban canopy layer for the calculation of the urban terrestrial

867 radiation budget. Representation of spectral reflectivities of urban materials  
868 and specular reflections is of lower priority since they only modify the urban  
869 radiation budget for urban morphologies and building materials, which do not  
870 occur frequently.

871 In future studies, HTRDR-Urban could be used to investigate meteorologi-  
872 cal situations with urban air pollution, urban districts with different types of  
873 trees, windows with different coatings, districts with heterogeneous materials  
874 and building types, or uneven ground. The results of the present study to-  
875 gether with those of Hogan (2019a) are the motivation to couple the urban  
876 canopy model Town Energy Balance (TEB, Masson (2000)) with the new ur-  
877 ban radiation scheme SPARTACUS-Urban (Hogan 2019b), which allows to  
878 overcome most of the shortcomings of radiation transfer calculations in urban  
879 canopy models identified in the present study.

880 **Acknowledgements** Simone Kotthaus is acknowledged for sharing the Spectral Library  
881 of Impervious Urban Materials, Vincent Eymet for his help with the creation of the optical  
882 properties files, and Najda Villefranque for her advice on the cloud optical properties files.

## 883 9 Declarations

### 884 9.1 Ethical Approval

885 This declaration is not applicable.

### 886 9.2 Competing interests

887 The authors declare no competing interest.

### 888 9.3 Authors' contributions

889 Conceptualization: Robert Schoetter, Robin Hogan, Valéry Masson; Method-  
890 ology: Robert Schoetter, Cyril Caliot, Tin-Yuet Chung, Robin Hogan, Valéry  
891 Masson; Formal analysis and investigation: Robert Schoetter, Cyril Caliot,  
892 Tin-Yuet Chung, Robin Hogan, Valéry Masson; Writing - original draft prepara-  
893 tion: Robert Schoetter, Cyril Caliot, Tin-Yuet Chung; Writing - review and  
894 editing: Robert Schoetter, Cyril Caliot, Tin-Yuet Chung, Robin Hogan, Valéry  
895 Masson; Project administration: Robert Schoetter, Cyril Caliot; Funding ac-  
896 quisition: Robert Schoetter, Cyril Caliot

### 897 9.4 Funding

898 This work received financial support from the French Agency for Ecologi-  
899 cal Transition ADEME (project MODRADURB-1917C001). Partial financial

900 support was received from French National Research Agency through Grant  
901 ANR-21-CE46-0013.

## 902 9.5 Availability of data and materials

903 The new HTRDR-Urban code package for solar and infrared radiative flux  
904 computations associated with the current submission is publicly available at  
905 [https://gitlab.com/edstar/htrdr/-/tree/main\\_urban](https://gitlab.com/edstar/htrdr/-/tree/main_urban).

906 The scripts to launch and postprocess the HTRDR-Urban simulations that  
907 are presented here are available on request.

## 908 **Appendix 1: List of symbols**

909 The list of symbols is given in Table 5.

## 910 **References**

- 911 Aida M, Gotoh K (1982) Urban albedo as a function of the urban structure — a  
912 two-dimensional numerical simulation. *Boundary-Layer Meteorol* 23(4):415–  
913 424, DOI 10.1007/BF00116270
- 914 Arnfield A (1976) Numerical modelling of urban surface radiative parameters.,  
915 pp 1–28
- 916 Arnfield AJ (2000) A simple model of urban canyon energy budget and its val-  
917 idation. *Phys Geogr* 21(4):305–326, DOI 10.1080/02723646.2000.10642712
- 918 Arnfield AJ (2003) Two decades of urban climate research: a review of tur-  
919 bulence, exchanges of energy and water, and the urban heat island. *Int J*  
920 *Climatol* 23(1):1–26, DOI 10.1002/joc.859
- 921 Best MJ (2005) Representing urban areas within operational numerical  
922 weather prediction models. *Boundary-Layer Meteorol* 114(1):91–109, DOI  
923 10.1007/s10546-004-4834-5
- 924 Best MJ, Grimmond CSB (2015) Key conclusions of the First International  
925 Urban Land Surface Model Comparison Project. *Bull Am Meteorol Soc*  
926 96(5):805–819, DOI 10.1175/BAMS-D-14-00122.1
- 927 Blazejczyk K, Epstein Y, Jendritzky G, Staiger H, Tinz B (2012) Comparison  
928 of UTCI to selected thermal indices. *Int J Biometeorol* 56:515–535, DOI  
929 10.1007/s00484-011-0453-2
- 930 Bruse M, Flerer H (1998) Simulating surface–plant–air interactions inside urban  
931 environments with a three dimensional numerical model. *Environ Modell*  
932 *Softw* 13(3):373–384, DOI 10.1016/S1364-8152(98)00042-5
- 933 Ca VT, Asaeda T, Ashie Y (1999) Development of a numerical model for the  
934 evaluation of the urban thermal environment. *J Wind Eng Ind Aerodyn*  
935 81(1):181–196, DOI [https://doi.org/10.1016/S0167-6105\(99\)00016-1](https://doi.org/10.1016/S0167-6105(99)00016-1)

- 936 Caliot C, Schoetter R, Forest V, Eymet V, Chung TY (2022) Model of spectral  
937 and directional radiative transfer in complex urban canopies with participat-  
938 ing atmospheres. *Boundary-Layer Meteorol* DOI 10.1007/s10546-022-00750-  
939 5
- 940 Carlson TN, Boland FE (1978) Analysis of urban-rural canopy using a surface  
941 heat flux/temperature model. *J Appl Meteorol Clim* 17(7):998–1013, DOI  
942 10.1175/1520-0450(1978)017<0998:AOURCU>2.0.CO;2
- 943 Chin HNS, Leach MJ, Sugiyama GA, Leone JM, Walker H, Nasstrom JS,  
944 Brown MJ (2005) Evaluation of an urban canopy parameterization in a  
945 mesoscale model using VTMX and URBAN 2000 data. *Mon Weather Rev*  
946 133(7):2043–2068, DOI 10.1175/MWR2962.1
- 947 Coddington O, Lean LJ, Doug L, Pilewskie P, Snow M, NOAA CDR Program  
948 (2015) NOAA climate data record (CDR) of solar spectral irradiance (SSI),  
949 NRLSSI version 2. [ssi\_v02r01\_yearly\_s1610\_e2020\_c20210204.nc]. DOI  
950 10.7289/V51J97P6
- 951 Collins M, Knutti R, Arblaster J, Dufresne JL, Fichet T, Friedlingstein P,  
952 Gao X, Gutowski W, Johns T, Krinner G, Shongwe M, Tebaldi C, Weaver  
953 A, Wehner M (2013) Chapter 12 - long-term climate change: Projections,  
954 commitments and irreversibility. In: IPCC (ed) *Climate Change 2013: The*  
955 *Physical Science Basis*. IPCC Working Group I Contribution to AR5, Cam-  
956 bridge University Press, Cambridge
- 957 De Ridder K, Lauwaet D, Maiheu B (2015) Urbclim – a fast ur-  
958 ban boundary layer climate model. *Urban Clim* 12:21–48, DOI  
959 <https://doi.org/10.1016/j.uclim.2015.01.001>
- 960 Dissegna MA, Yin T, Wu H, Lauret N, Wei S, Gastellu-Etchegorry JP, Grêt-  
961 Regamey A (2021) Modeling Mean Radiant Temperature distribution in  
962 urban landscapes using DART. *Remote Sens* 13(8), DOI 10.3390/rs13081443
- 963 Dupont S, Mestayer PG (2006) Parameterization of the urban energy budget  
964 with the submesoscale soil model. *J Appl Meteorol Clim* 45(12):1744–1765,  
965 DOI 10.1175/JAM2417.1
- 966 Dupont S, Otte TL, Ching JK (2004) Simulation of meteorolog-  
967 ical fields within and above urban and rural canopies with a  
968 mesoscale model (MM5). *Boundary-Layer Meteorol* 113(1):111–158, DOI  
969 10.1023/B:BOUN.0000037327.19159.ac
- 970 El Hafi M, Blanco S, Dauchet J, Fournier R, Galtier M, Ibarrart L, Tre-  
971 gan JM, Villefranque N (2021) Three viewpoints on null-collision monte  
972 carlo algorithms. *J Quant Spectrosc Radiat Transf* 260:107,402, DOI  
973 <https://doi.org/10.1016/j.jqsrt.2020.107402>
- 974 Frayssinet L, Merlier L, Kuznik F, Hubert JL, Milliez M, Roux JJ (2018)  
975 Modeling the heating and cooling energy demand of urban buildings at city  
976 scale. *Renew Sust Energ Rev* 81:2318–2327, DOI 10.1016/j.rser.2017.06.040
- 977 Fröhlich D, Matzarakis A (2020) Calculating human thermal comfort and ther-  
978 mal stress in the palm model system 6.0. *Geosci Model Dev* 13(7):3055–3065,  
979 DOI 10.5194/gmd-13-3055-2020
- 980 Galtier M, Blanco S, Caliot C, Coustet C, Dauchet J, El Hafi M, Eymet  
981 V, Fournier R, Gautrais J, Khuong A, Piaud B, Terrée G (2013) Integral

- 982 formulation of null-collision Monte Carlo algorithms. *J Quant Spectrosc*  
983 *Radiat Transf* 125:57–68, DOI 10.1016/j.jqsrt.2013.04.001
- 984 Geletić J, Lehnert M, Resler J, Krč P, Middel A, Krayenhoff E, Krüger E  
985 (2022) High-fidelity simulation of the effects of street trees, green roofs and  
986 green walls on the distribution of thermal exposure in prague-dejvice. *Build*  
987 *Environ* 223:109,484, DOI <https://doi.org/10.1016/j.buildenv.2022.109484>
- 988 Grimmond CSB, Blackett M, Best MJ, Barlow J, Baik JJ, Belcher SE, Bohnen-  
989 stengel SI, Calmet I, Chen F, Dandou A, Fortuniak K, Gouvea ML, Hamdi  
990 R, Hendry M, Kawai T, Kawamoto Y, Kondo H, Krayenhoff ES, Lee SH,  
991 Loridan T, Martilli A, Masson V, Miao S, Oleson K, Pigeon G, Porson A,  
992 Ryu YH, Salamanca F, Shashua-Bar L, Steeneveld GJ, Tombrou M, Voogt  
993 J, Young D, Zhang N (2010) The International Urban Energy Balance Mod-  
994 els Comparison Project: First results from Phase 1. *J Appl Meteorol Clim*  
995 49(6):1268–1292, DOI 10.1175/2010JAMC2354.1
- 996 Grimmond CSB, Blackett M, Best MJ, Baik JJ, Belcher SE, Beringer J,  
997 Bohnenstengel SI, Calmet I, Chen F, Coutts A, Dandou A, Fortuniak K,  
998 Gouvea ML, Hamdi R, Hendry M, Kanda M, Kawai T, Kawamoto Y, Kondo  
999 H, Krayenhoff ES, Lee SH, Loridan T, Martilli A, Masson V, Miao S, Ole-  
1000 son K, Ooka R, Pigeon G, Porson A, Ryu YH, Salamanca F, Steeneveld  
1001 G, Tombrou M, Voogt JA, Young DT, Zhang N (2011) Initial results from  
1002 Phase 2 of the International Urban Energy Balance Model Comparison. *Int*  
1003 *J Climatol* 31(2):244–272, DOI 10.1002/joc.2227
- 1004 Grossman-Clarke S, Zehnder JA, Stefanov WL, Liu Y, Zoldak MA (2005)  
1005 Urban modifications in a mesoscale meteorological model and the effects  
1006 on near-surface variables in an arid metropolitan region. *J Appl Meteorol*  
1007 44(9):1281–1297, DOI 10.1175/JAM2286.1
- 1008 Harman IN, Best MJ, Belcher SE (2004) Radiative exchange in an  
1009 urban street canyon. *Boundary-Layer Meteorol* 110:301–316, DOI  
1010 10.1023/A:1026029822517
- 1011 Hogan RJ (2019a) An exponential model of urban geometry for use in ra-  
1012 diative transfer applications. *Boundary-Layer Meteorol* 170:357–372, DOI  
1013 10.1007/s10546-018-0409-8
- 1014 Hogan RJ (2019b) Flexible treatment of radiative transfer in complex urban  
1015 canopies for use in weather and climate models. *Boundary-Layer Meteorol*  
1016 173(1):53–78, DOI 10.1007/s10546-019-00457-0
- 1017 Hogan RJ, Bozzo A (2016) ECRAD: A new radiation scheme for the IFS.  
1018 ECMWF Technical Memoranda (787)
- 1019 Hogan RJ, Bozzo A (2018) A flexible and efficient radiation scheme for  
1020 the ECMWF model. *J Adv Model Earth Syst* 10(8):1990–2008, DOI  
1021 <https://doi.org/10.1029/2018MS001364>
- 1022 Höppe P (1999) The physiological equivalent temperature – a universal in-  
1023 dex for the biometeorological assessment of the thermal environment. *Int J*  
1024 *Biometeorol* 43:71–75, DOI 10.1007/s004840050118
- 1025 Joseph JH, Wiscombe WJ, Weinman JA (1976) The delta-eddington approx-  
1026 imation for radiative flux transfer. *J Atmos Sci* 33(12):2452–2459, DOI  
1027 10.1175/1520-0469(1976)033<2452:TDEAFR>2.0.CO;2



- 1028 Kanda M, Kawai T, Kanega M, Moriwaki R, Narita K, Hagishima A (2005a)  
1029 A simple energy balance model for regular building arrays. *Boundary-Layer*  
1030 *Meteorol* 116:423–443, DOI 10.1007/s10546-004-7956-x
- 1031 Kanda M, Kawai T, Nakagawa K (2005b) A simple theoretical radiation  
1032 scheme for regular building arrays. *Boundary-Layer Meteorol* 114(1):71–90,  
1033 DOI 10.1007/s10546-004-8662-4
- 1034 Kelly G, McCabe H (2006) A survey of procedural techniques for city gener-  
1035 ation. *The ITB Journal* 7(2), DOI doi:10.21427/D76M9P
- 1036 Kobayashi T, Takamura T (1994) Upward longwave radiation from a non-black  
1037 urban canopy. *Boundary-Layer Meteorol* 69:201–213
- 1038 Kondo H, Genchi Y, Kikegawa Y, Ohashi Y, Yoshikado H, Komiyama H  
1039 (2005) Development of a multi-layer urban canopy model for the analysis  
1040 of energy consumption in a big city: Structure of the urban canopy model  
1041 and its basic performance. *Boundary-Layer Meteorol* 116(3):395–421, DOI  
1042 10.1007/s10546-005-0905-5
- 1043 Kotthaus S, Grimmond C (2014) Energy exchange in a dense urban environ-  
1044 ment – Part II: Impact of spatial heterogeneity of the surface. *Urban Clim*  
1045 10:281–307, DOI <https://doi.org/10.1016/j.uclim.2013.10.001>
- 1046 Kotthaus S, Smith T, Wooster M, Grimmond S (2013) Spectral Library of Im-  
1047 pervious Urban Materials (version 1.0) [luma\_slum\_sw.csv luma\_slum\_ir.csv]
- 1048 Kotthaus S, Smith TE, Wooster MJ, Grimmond C (2014) Derivation of  
1049 an urban materials spectral library through emittance and reflectance  
1050 spectroscopy. *ISPRS J Photogramm Remote Sens* 94:194–212, DOI  
1051 10.1016/j.isprsjprs.2014.05.005
- 1052 Krayenhoff ES, Voogt JA (2007) A microscale three-dimensional urban energy  
1053 balance model for studying surface temperatures. *Boundary-Layer Meteorol*  
1054 123(3):433–461, DOI 10.1007/s10546-006-9153-6
- 1055 Krayenhoff ES, Christen A, Martilli A, Oke TR (2014) A multi-layer radia-  
1056 tion model for urban neighbourhoods with trees. *Boundary-Layer Meteorol*  
1057 151(1):139–178, DOI 10.1007/s10546-013-9883-1
- 1058 Krayenhoff ES, Jiang T, Christen A, Martilli A, Oke TR, Bailey BN, Nazar-  
1059 ian N, Voogt JA, Giometto MG, Stastny A, Crawford BR (2020) A multi-  
1060 layer urban canopy meteorological model with trees (BEP-Tree): Street  
1061 tree impacts on pedestrian-level climate. *Urban Clim* 32:100,590, DOI  
1062 10.1016/j.uclim.2020.100590
- 1063 Krč P, Resler J, Sührling M, Schubert S, Salim MH, Fuka V (2021) Radiative  
1064 Transfer Model 3.0 integrated into the PALM model system 6.0. *Geosci*  
1065 *Model Dev* 14(5):3095–3120, DOI 10.5194/gmd-14-3095-2021
- 1066 Kusaka H, Kondo H, Kikegawa Y, Kimura F (2001) A simple single-layer  
1067 urban canopy model for atmospheric models: Comparison with multi-  
1068 layer and slab models. *Boundary-Layer Meteorol* 101:329–358, DOI  
1069 10.1023/A:1019207923078
- 1070 Lee SH, Park SU (2008) A vegetated urban canopy model for meteorologi-  
1071 cal and environmental modelling. *Boundary-Layer Meteorol* 126(1):73–102,  
1072 DOI 10.1007/s10546-007-9221-6

- 1073 Li D, Malyshev S, Shevliakova E (2016) Exploring historical and future  
1074 urban climate in the earth system modeling framework: 1. Model de-  
1075 velopment and evaluation. *J Adv Model Earth Syst* 8(2):917–935, DOI  
1076 <https://doi.org/10.1002/2015MS000578>
- 1077 Lundquist KA, Chow FK, Lundquist JK (2012) An immersed boundary  
1078 method enabling large-eddy simulations of flow over complex terrain in  
1079 the wrf model. *Monthly Weather Review* 140(12):3936 – 3955, DOI  
1080 <https://doi.org/10.1175/MWR-D-11-00311.1>
- 1081 Maronga B, Banzhaf S, Burmeister C, Esch T, Forkel R, Fröhlich D, Fuka V,  
1082 Gehrke KF, Geletič J, Giersch S, Gronemeier T, Groß G, Heldens W, Hell-  
1083 sten A, Hoffmann F, Inagaki A, Kadasch E, Kanani-Sühring F, Ketelsen K,  
1084 Khan BA, Knigge C, Knoop H, Krč P, Kurppa M, Maamari H, Matzarakis  
1085 A, Mauder M, Pallasch M, Pavlik D, Pfafferoth J, Resler J, Rissmann S,  
1086 Russo E, Salim M, Schrempf M, Schwenkel J, Seckmeyer G, Schubert S,  
1087 Sühring M, von Tils R, Vollmer L, Ward S, Witha B, Wurps H, Zeidler  
1088 J, Raasch S (2020) Overview of the palm model system 6.0. *Geoscientific  
1089 Model Development* 13(3):1335–1372, DOI 10.5194/gmd-13-1335-2020
- 1090 Martilli A, Clappier A, Rotach MW (2002) An urban surface exchange param-  
1091 eterisation for mesoscale models. *Boundary-Layer Meteorol* 104(2):261–304,  
1092 DOI 10.1023/A:1016099921195
- 1093 Masson V (2000) A physically-based scheme for the urban energy budget  
1094 in atmospheric models. *Boundary-Layer Meteorol* 94(3):357–397, DOI  
1095 10.1023/A:1002463829265
- 1096 Mayer H, Holst J, Dostal P, Imbery F, Schindler D (2008) Human thermal  
1097 comfort in summer within an urban street canyon in central europe. *Meteo-  
1098 rol Z* 17(3):241–250, DOI 10.1127/0941-2948/2008/0285
- 1099 Meili N, Manoli G, Burlando P, Bou-Zeid E, Chow WTL, Coutts AM, Daly E,  
1100 Nice KA, Roth M, Tapper NJ, Velasco E, Vivoni ER, Fatichi S (2020) An  
1101 urban ecohydrological model to quantify the effect of vegetation on urban  
1102 climate and hydrology (UT&C v1.0). *Geosci Model Dev* 13(1):335–362, DOI  
1103 10.5194/gmd-13-335-2020
- 1104 Milliez M, Carissimo B (2007) Numerical simulations of pollutant dispersion in  
1105 an idealized urban area, for different meteorological conditions. *Boundary-  
1106 Layer Meteorology* 122:321–342, DOI [https://doi.org/10.1007/s10546-006-  
1107 9110-4](https://doi.org/10.1007/s10546-006-9110-4)
- 1108 Mills G (1997) An urban canopy-layer climate model. *Theor Appl Climatol*  
1109 57:229–244, DOI 10.1007/BF00863615
- 1110 Montávez JP, Jiménez JL, Sarsa A (2000) A Monte Carlo model of the noc-  
1111 turnal surface temperatures in urban canyons. *Boundary-Layer Meteorol*  
1112 96(3):433–452, DOI 10.1023/A:1002600523841
- 1113 Myrup LO (1969) A numerical model of the urban heat is-  
1114 land. *J Appl Meteorol Clim* 8(6):908–918, DOI 10.1175/1520-  
1115 0450(1969)008;0908:ANMOTU;2.0.CO;2
- 1116 Nice KA, Coutts AM, Tapper NJ (2018) Development of the VTUF-3D  
1117 v1.0 urban micro-climate model to support assessment of urban vegeta-  
1118 tion influences on human thermal comfort. *Urban Clim* 24:1052–1076, DOI

- 1119 <https://doi.org/10.1016/j.uclim.2017.12.008>
- 1120 Oke TR (1982) The energetic basis of the urban heat island. *Q J R Meteorol*
- 1121 *Soc* 108(455):1–24, DOI 10.1002/qj.49710845502
- 1122 Oleson KW, Bonan GB, Feddema J, Vertenstein M, Grimmond CSB (2008)
- 1123 An urban parameterization for a global climate model. Part I: Formulation
- 1124 and evaluation for two cities. *J Appl Meteorol Clim* 47(4):1038–1060, DOI
- 1125 10.1175/2007JAMC1597.1
- 1126 Outcalt SI (1972) A reconnaissance experiment in mapping and
- 1127 modeling the effect of land use on urban thermal regimes.
- 1128 *J Appl Meteorol Clim* 11(8):1369–1373, DOI 10.1175/1520-
- 1129 0450(1972)011;1369:AREIMA;2.0.CO;2
- 1130 Porson A, Clark PA, Harman IN, Best MJ, Belcher SE (2010) Implementation
- 1131 of a new urban energy budget scheme in the MetUM. Part I: Description
- 1132 and idealized simulations. *Q J R Meteorol Soc* 136(651):1514–1529, DOI
- 1133 10.1002/qj.668
- 1134 Rubin M (1985) Optical properties of soda lime silica glasses. *Sol Energ Mater*
- 1135 12(4):275–288, DOI 10.1016/0165-1633(85)90052-8
- 1136 Ryu YH, Baik JJ, Lee SH (2011) A new single-layer urban canopy model for
- 1137 use in mesoscale atmospheric models. *J Appl Meteorol Clim* 50(9):1773–
- 1138 1794, DOI 10.1175/2011JAMC2665.1
- 1139 Ryu YH, Bou-Zeid E, Wang ZH, Smith JA (2016) Realistic representation of
- 1140 trees in an urban canopy model. *Boundary-Layer Meteorol* 159(2):193–220,
- 1141 DOI 10.1007/s10546-015-0120-y
- 1142 Saitoh T, Shimada T, Hoshi H (1996) Modeling and simulation of
- 1143 the Tokyo urban heat island. *Atmos Environ* 30(20):3431–3442, DOI
- 1144 [https://doi.org/10.1016/1352-2310\(95\)00489-0](https://doi.org/10.1016/1352-2310(95)00489-0)
- 1145 Sakakibara Y (1995) A numerical study of the effect of urban geometry upon
- 1146 the surface energy budget. *Atmos Environ* 30:487–496
- 1147 Salim MH, Schlünzen KH, Grawe D, Boettcher M, Gierisch AMU, Fock
- 1148 BH (2018) The microscale obstacle-resolving meteorological model mitras
- 1149 v2.0: model theory. *Geoscientific Model Development* 11(8):3427–3445, DOI
- 1150 10.5194/gmd-11-3427-2018
- 1151 Salim MH, Schubert S, Resler J, Krč P, Maronga B, Kanani-Sühring F, Sühring
- 1152 M, Schneider C (2022) Importance of radiative transfer processes in urban
- 1153 climate models: a study based on the palm 6.0 model system. *Geoscientific*
- 1154 *Model Development* 15(1):145–171, DOI 10.5194/gmd-15-145-2022
- 1155 Schoetter R, Grawe D, Hoffmann P, Kirschner P, Grätz A, Schlünzen KH
- 1156 (2013) Impact of local adaptation measures and regional climate change
- 1157 on perceived temperature. *Meteorol Z* 22(2):117–130, DOI 10.1127/0941-
- 1158 2948/2013/0381
- 1159 Schubert S, Grossman-Clarke S, Martilli A (2012) A double-canyon radia-
- 1160 tion scheme for multi-layer urban canopy models. *Boundary-Layer Meteorol*
- 1161 145(3):439–468, DOI 10.1007/s10546-012-9728-3
- 1162 Stewart ID, Oke TR (2012) Local Climate Zones for urban temperature stud-
- 1163 ies. *Bull Am Meteorol Soc* 93(12):1879–1900, DOI 10.1175/BAMS-D-11-
- 1164 00019.1

- 1165 Stretton MA, Morrison W, Hogan R, Grimmond S (2022) Evaluation of the  
1166 SPARTACUS-Urban radiation model for vertically resolved shortwave ra-  
1167 diation in urban areas. *Boundary-Layer Meteorol* DOI 10.1007/s10546-022-  
1168 00706-9
- 1169 Strømman-Andersen J, Sattrup P (2011) The urban canyon and building en-  
1170 ergy use: Urban density versus daylight and passive solar gains. *Energy Buil*  
1171 43(8):2011–2020, DOI 10.1016/j.enbuild.2011.04.007
- 1172 Suter I, Grylls T, Sützl BS, Owens SO, Wilson CE, van Reeuwijk M (2022)  
1173 udales 1.0: a large-eddy simulation model for urban environments. *Geoscientific*  
1174 *Model Development* 15(13):5309–5335, DOI 10.5194/gmd-15-5309-2022
- 1175 Thatcher M, Hurley P (2012) Simulating Australian urban climate in  
1176 a mesoscale atmospheric numerical model. *Boundary-Layer Meteorol*  
1177 142(1):149–175, DOI 10.1007/s10546-011-9663-8
- 1178 Thorsson S, Lindberg F, Eliasson I, Holmer B (2007) Different methods for  
1179 estimating the mean radiant temperature in an outdoor urban setting. *Int*  
1180 *J Climatol* 27(14):1983–1993, DOI <https://doi.org/10.1002/joc.1537>
- 1181 Todhunter PE, Terjung WH (1988) Intercomparison of three urban climate  
1182 models. *Boundary-Layer Meteorol* 42(3):181–205, DOI 10.1007/BF00123812
- 1183 Tornay N, Schoetter R, Bonhomme M, Faraut S, Masson V (2017) GENIUS: A  
1184 methodology to define a detailed description of buildings for urban climate  
1185 and building energy consumption simulations. *Urban Clim* 20:75–93
- 1186 Tso C, Chan B, Hashim M (1990) An improvement to the basic energy balance  
1187 model for urban thermal environment analysis. *Energy Buil* 14(2):143–152,  
1188 DOI [https://doi.org/10.1016/0378-7788\(90\)90033-F](https://doi.org/10.1016/0378-7788(90)90033-F)
- 1189 UN (2019) World urbanization prospects - the 2018 revision. Department of  
1190 Economic and Social Affairs, Tech Rep ST/ESA/SER.A/420
- 1191 Versegny DL, Munro DS (1989a) Sensitivity studies on the calculation of the  
1192 radiation balance of urban surfaces: I. Shortwave radiation. *Boundary-Layer*  
1193 *Meteorol* 46(4):309–331, DOI 10.1007/BF00172239
- 1194 Versegny DL, Munro DS (1989b) Sensitivity studies on the calculation of the  
1195 radiation balance of urban surfaces: II. Longwave radiation. *Boundary-Layer*  
1196 *Meteorol* 48(1):1–18, DOI 10.1007/BF00121780
- 1197 Villefranque N, Fournier R, Couvreur F, Blanco S, Cornet C, Eymet V, Forest  
1198 V, Tregan JM (2019) A path-tracing Monte Carlo library for 3-D radiative  
1199 transfer in highly resolved cloudy atmospheres. *J Adv Model Earth Syst*  
1200 11(8):2449–2473, DOI 10.1029/2018MS001602
- 1201 Villefranque N, Hourdin F, d’Alençon L, Blanco S, Boucher O, Caliot C,  
1202 Coustet C, Dauchet J, Hafi ME, Eymet V, Farges O, Forest V, Fournier  
1203 R, Gautrais J, Masson V, Piaud B, Schoetter R (2022) The ”teapot in a  
1204 city”: A paradigm shift in urban climate modeling. *Sci Adv* 8(27):eabp8934,  
1205 DOI 10.1126/sciadv.abp8934
- 1206 Wang C, Wang ZH, Ryu YH (2021) A single-layer urban canopy model with  
1207 transmissive radiation exchange between trees and street canyons. *Build*  
1208 *Environ* 191:107,593, DOI <https://doi.org/10.1016/j.buildenv.2021.107593>
- 1209 Wang ZH (2014) Monte Carlo simulations of radiative heat exchange  
1210 in a street canyon with trees. *Sol Energy* 110:704–713, DOI

- 1211 10.1016/j.solener.2014.10.012
- 1212 Wang ZH, Bou-Zeid E, Smith JA (2013) A coupled energy transport  
1213 and hydrological model for urban canopies evaluated using a wire-  
1214 less sensor network. *Q J R Meteorol Soc* 139(675):1643–1657, DOI  
1215 <https://doi.org/10.1002/qj.2032>
- 1216 Wouters H, Demuzere M, Blahak U, Fortuniak K, Maiheu B, Camps J, Tiele-  
1217 mans D, van Lipzig NPM (2016) The efficient urban canopy dependency  
1218 parametrization (SURY) v1.0 for atmospheric modelling: description and  
1219 application with the COSMO-CLM model for a Belgian summer. *Geosci*  
1220 *Model Dev* 9(9):3027–3054, DOI 10.5194/gmd-9-3027-2016
- 1221 Yang L, Yan H, Lam JC (2014) Thermal comfort and building energy  
1222 consumption implications – a review. *Appl Energy* 115:164–173, DOI  
1223 <http://dx.doi.org/10.1016/j.apenergy.2013.10.062>
- 1224 Yang X, Li Y (2013) Development of a three-dimensional urban energy  
1225 model for predicting and understanding surface temperature distribution.  
1226 *Boundary-Layer Meteorol* 149(2):303–321, DOI 10.1007/s10546-013-9842-x

1227 **Supplementary Material For *Boundary-Layer Meteorology* Uncer-**  
1228 **tainties of Radiative Transfer Calculation in Urban Canopy Models**

1229 **Robert Schoetter\*** · Cyril Caliot · Tin-Yuet Chung · Robin Hogan ·  
1230 **Valéry Masson**

1231

1232 \*CNRM, Université de Toulouse, Météo-France, CNRS, 42 avenue Gaspard  
1233 Coriolis, Toulouse, France, robert.schoetter@meteo.fr.

1234 **1 Supplementary Figures**

1235 1.1 Distribution of Wall-to-wall and Wall-to-ground Distances

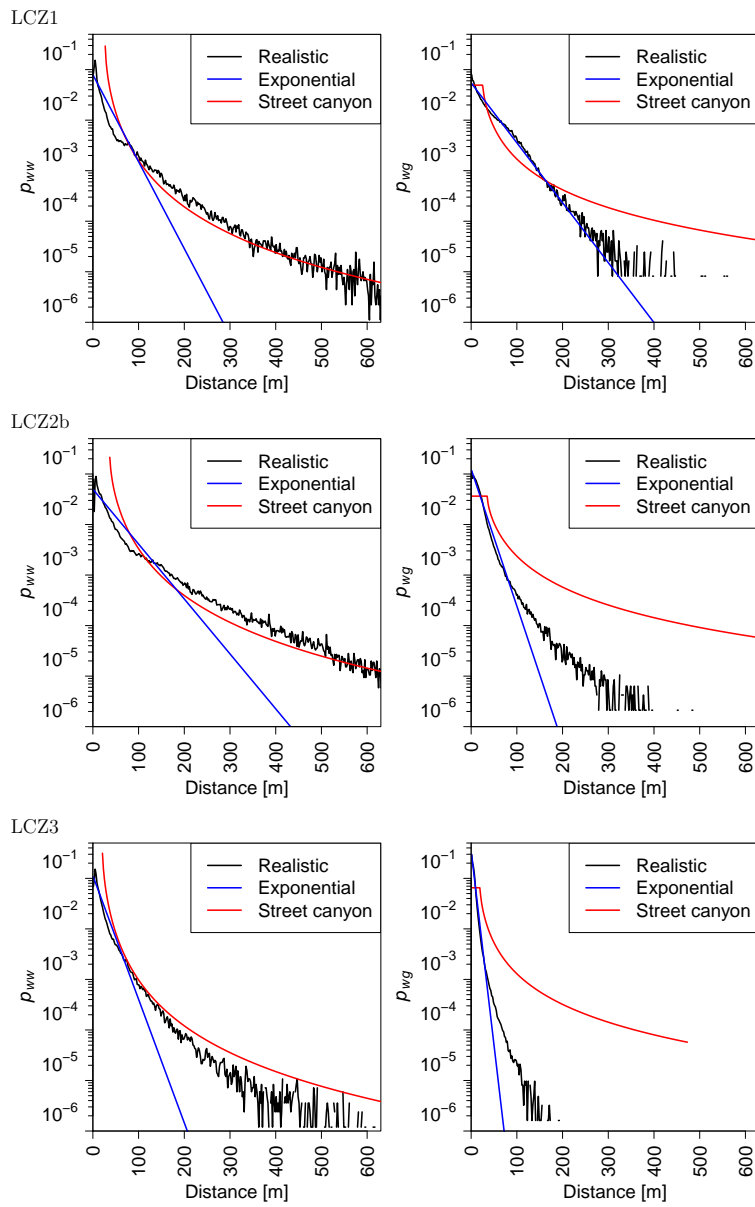
1236 1.2 Simplification of Urban Morphology

1237 1.3 Influence of Spectrally-reflecting Windows

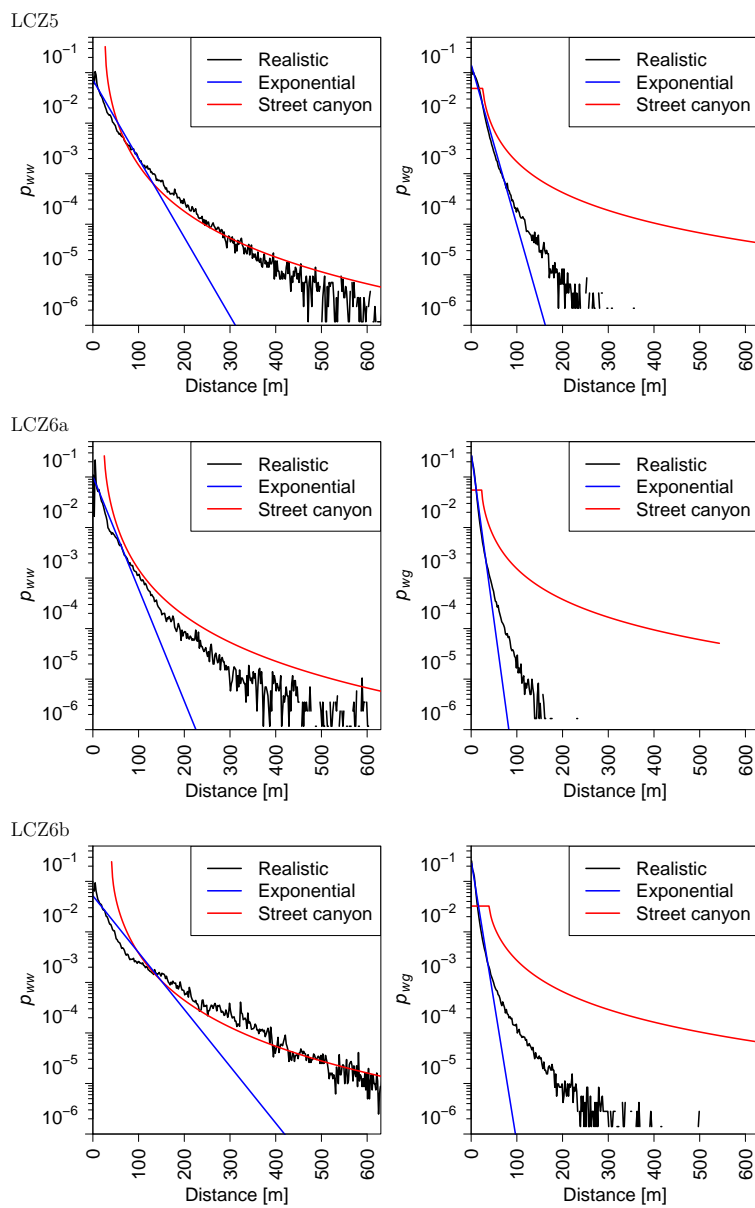
1238 1.4 Influence of Participating Atmosphere in the Urban Canopy Layer

1239 1.5 Influence of Trees on the Urban Radiation Budget

1240 1.6 Influence of Fog on the Urban Radiation Budget

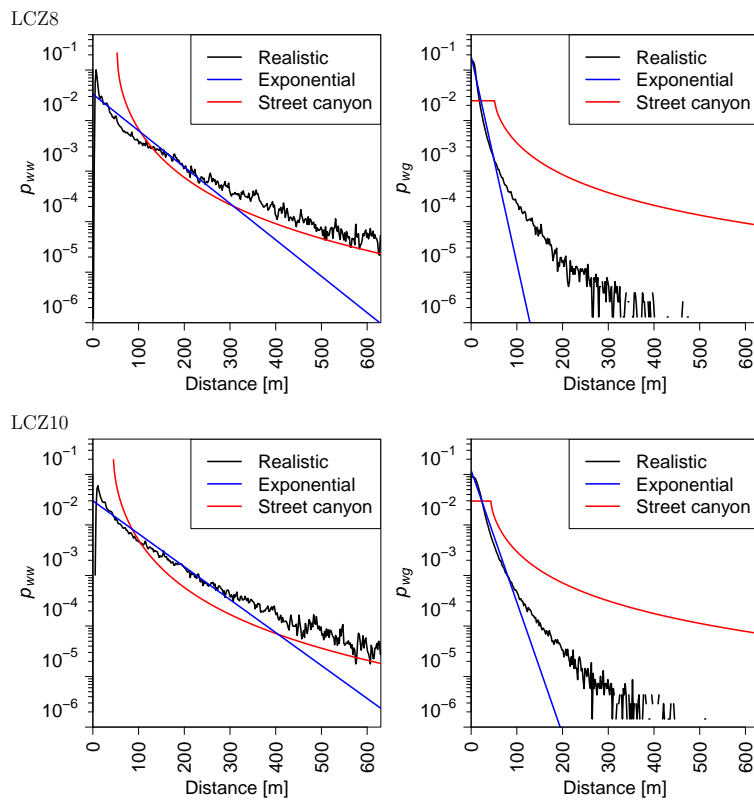


**Fig. 14** Distribution of wall-to-wall ( $p_{ww}$ ) and wall-to-ground ( $p_{wg}$ ) distances for the urban morphologies LCZ1, LCZ2b, and LCZ3



**Fig. 15** Same as Fig. 14, but for the urban morphologies LCZ5, LCZ6a, and LCZ6b

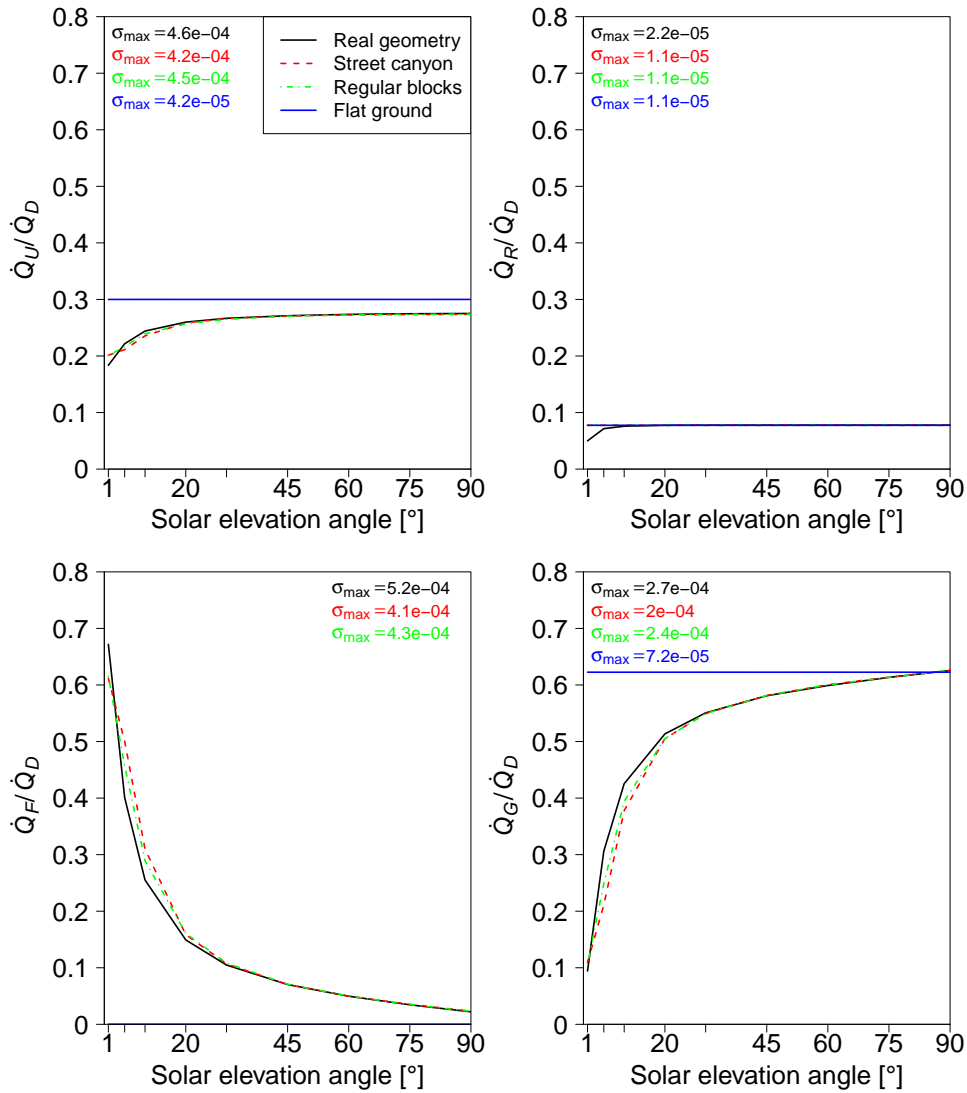




**Fig. 16** Same as Fig. 15, but for the urban morphologies LCZ8, and LCZ10

**Table 5** List of symbols

Symbol	Definition [unit]
$\alpha$	Solar reflectivity (albedo) [1]
$\alpha_{body}$	Average albedo of the human body [1]
$\alpha_{eff}$	Effective broadband albedo [1]
$\alpha_{win,Lam}$	Effective broadband Lambertian window albedo [1]
$A_{district}$	Total horizontal area of district [m <sup>2</sup> ]
$A_n$	Footprint area of building $n$ [m <sup>2</sup> ]
$AF_n$	External facade area of building $n$ [m <sup>2</sup> ]
$\Delta T_{surf}$	Difference between skin surface temperature and air temperature [K]
$\epsilon$	Emissivity of terrestrial radiation [1]
$\epsilon_{body}$	Average emissivity of the human body [1]
$\dot{E}_{air}$	Terrestrial radiation exchanged by the air in the urban canopy layer [W m <sup>-2</sup> ]
$\dot{E}_F$	Terrestrial radiation exchanged by the facades [W m <sup>-2</sup> ]
$\dot{E}_G$	Terrestrial radiation exchanged by the ground [W m <sup>-2</sup> ]
$\dot{E}_R$	Terrestrial radiation exchanged by the roofs [W m <sup>-2</sup> ]
$\dot{E}_{sky}$	Terrestrial radiation exchanged by the sky [W m <sup>-2</sup> ]
$\dot{E}_T$	Terrestrial radiation exchanged by the trees [W m <sup>-2</sup> ]
$f_g$	Facade glazing ratio [1]
$\gamma$	Solar elevation angle [°]
$H_{max}$	Maximum building height [m]
$H_{mean}$	Mean building height [m]
$H_n$	Height of building $n$ [m]
$\frac{H}{W}$	Aspect ratio of representative street canyon [1]
$I_{facet}$	Solar flux density incident on a facet [W m <sup>-2</sup> ]
$I_{win,spec}$	Solar flux density incident on a specularly reflecting window [W m <sup>-2</sup> ]
$k$	Extinction coefficient [m <sup>-1</sup> ]
$\lambda_p$	Plane area building density [1]
$\lambda_w$	External facade surface density [1]
$l_{side}$	Side length of one regular square block [m]
$l_{total}$	Side length of a plot with one regular square block [m]
$L$	Cumulative index of building surface area [m]
$LW_{down}$	Downwelling terrestrial radiation at the surface [W m <sup>-2</sup> ]
$LW_{net}$	Net exchanged terrestrial radiation at the surface [W m <sup>-2</sup> ]
$N_{build}$	Total number of buildings in district [1]
$N_f$	Number of facets in urban geometry [1]
$N_\gamma$	Number of Monte Carlo realisations for a solar elevation angle of $\gamma$ [1]
$N_l$	Number of layers in the urban canopy model [1]
$N_{stream}$	Number of streams per hemisphere employed in the Discrete Ordinates Method [1]
$N_{zen}$	Number of Monte Carlo realisations for $\gamma = 90^\circ$ [1]
$p_{wg}$	Probability distribution of wall-to-ground distance [1]
$p_{ww}$	Probability distribution of wall-to-wall distance [1]
$\dot{Q}_{air}$	Solar flux density absorbed by the air in the urban canopy layer [W m <sup>-2</sup> ]
$\dot{q}_{air}$	$\dot{Q}_{air}$ normalised by $\dot{Q}_D$ [1]
$\dot{Q}_{body,sw}$	Average solar flux density incident on the human body [W m <sup>-2</sup> ]
$\dot{Q}_{body,lw}$	Average terrestrial flux density incident on the human body [W m <sup>-2</sup> ]
$\dot{Q}_D$	Downwelling solar flux density at the top of the urban canopy layer [W m <sup>-2</sup> ]
$\dot{Q}_{facet}$	Solar flux density absorbed by a facet [W m <sup>-2</sup> ]
$\dot{Q}_F$	Solar flux density absorbed by the facades [W m <sup>-2</sup> ]
$\dot{q}_F$	$\dot{Q}_F$ normalised by $\dot{Q}_D$ [1]
$\dot{Q}_G$	Solar flux density absorbed by the ground [W m <sup>-2</sup> ]
$\dot{q}_G$	$\dot{Q}_G$ normalised by $\dot{Q}_D$ [1]
$\dot{Q}_R$	Solar flux density absorbed by the roofs [W m <sup>-2</sup> ]
$\dot{q}_R$	$\dot{Q}_R$ normalised by $\dot{Q}_D$ [1]
$\dot{Q}_T$	Solar flux density absorbed by the trees [W m <sup>-2</sup> ]
$\dot{q}_T$	$\dot{Q}_T$ normalised by $\dot{Q}_D$ [1]
$\dot{Q}_U$	Upwelling solar flux density at the top of the urban canopy layer [W m <sup>-2</sup> ]
$\dot{q}_U$	$\dot{Q}_U$ normalised by $\dot{Q}_D$ [1]
$\dot{Q}_{win,spec}$	Solar flux density absorbed by a specularly reflecting window [W m <sup>-2</sup> ]
$R_{net}$	Net all-wave radiation [W m <sup>-2</sup> ]
$\sigma$	Stefan-Boltzmann constant [W m <sup>-2</sup> ]
$\sigma_H$	Standard deviation of building height [m]
$\sigma_{max}$	Largest value of the standard deviation of normalised Monte Carlo observables [1]
$SW_{down}$	Downwelling solar radiation at the surface [W m <sup>-2</sup> ]
$SW_{net}$	Net absorbed solar radiation at the surface [W m <sup>-2</sup> ]
$T_s$	Skin surface temperature [K]
$z$	Height above ground [m]
$z_{top}$	Height of the urban canopy layer top [m]



**Fig. 17** Effect of urban morphology simplifications on the urban, roof, facade, and ground solar radiation budget for direct-only downwelling solar radiation and the LCZ9 morphology with flat roofs. The values of  $\sigma_{max}$  indicate the highest value of the standard deviation of the radiative observable obtained from the MCM simulations for all values of  $\gamma$

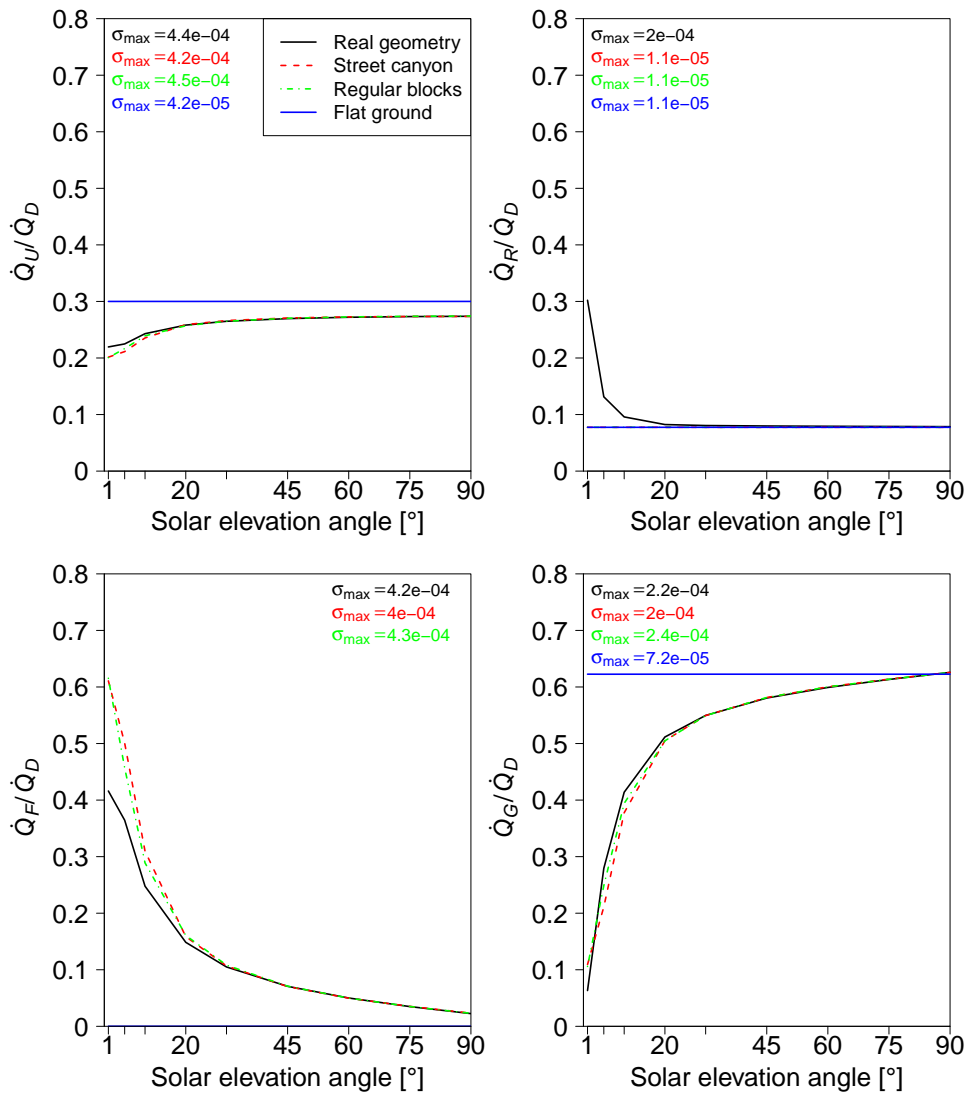


Fig. 18 Same as Fig. 17, but for LCZ9 with pitched roofs

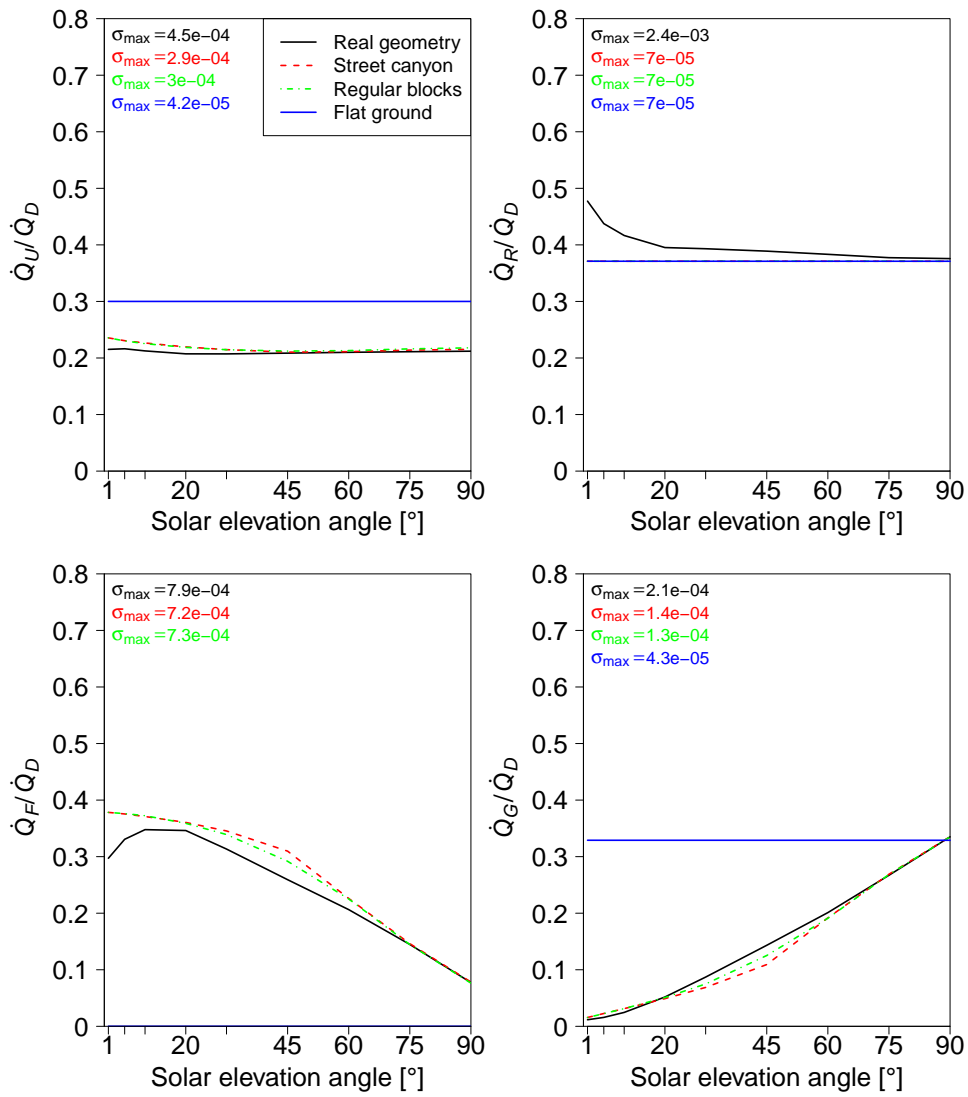


Fig. 19 Same as Fig. 17, but for LCZ2a with pitched roofs

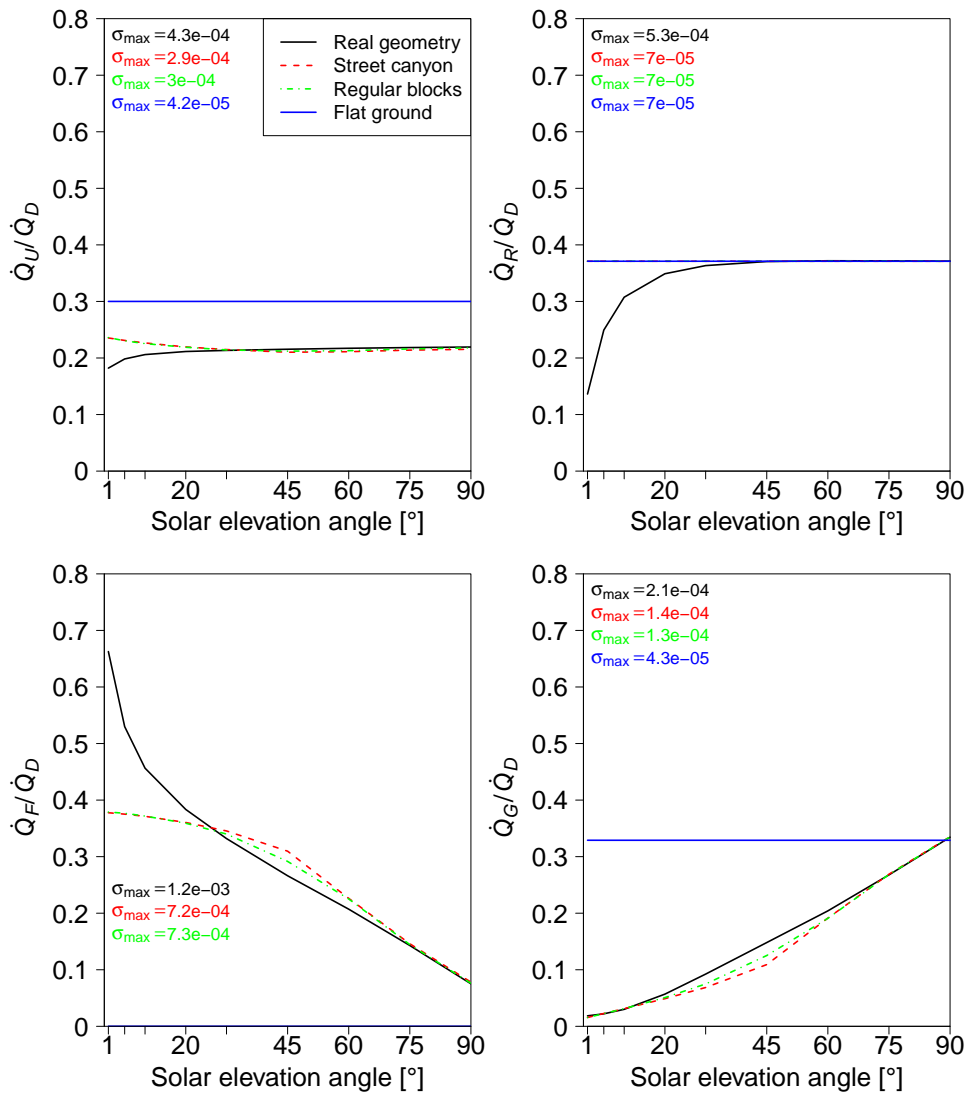


Fig. 20 Same as Fig. 17, but for the LCZ2a morphology with flat roofs.

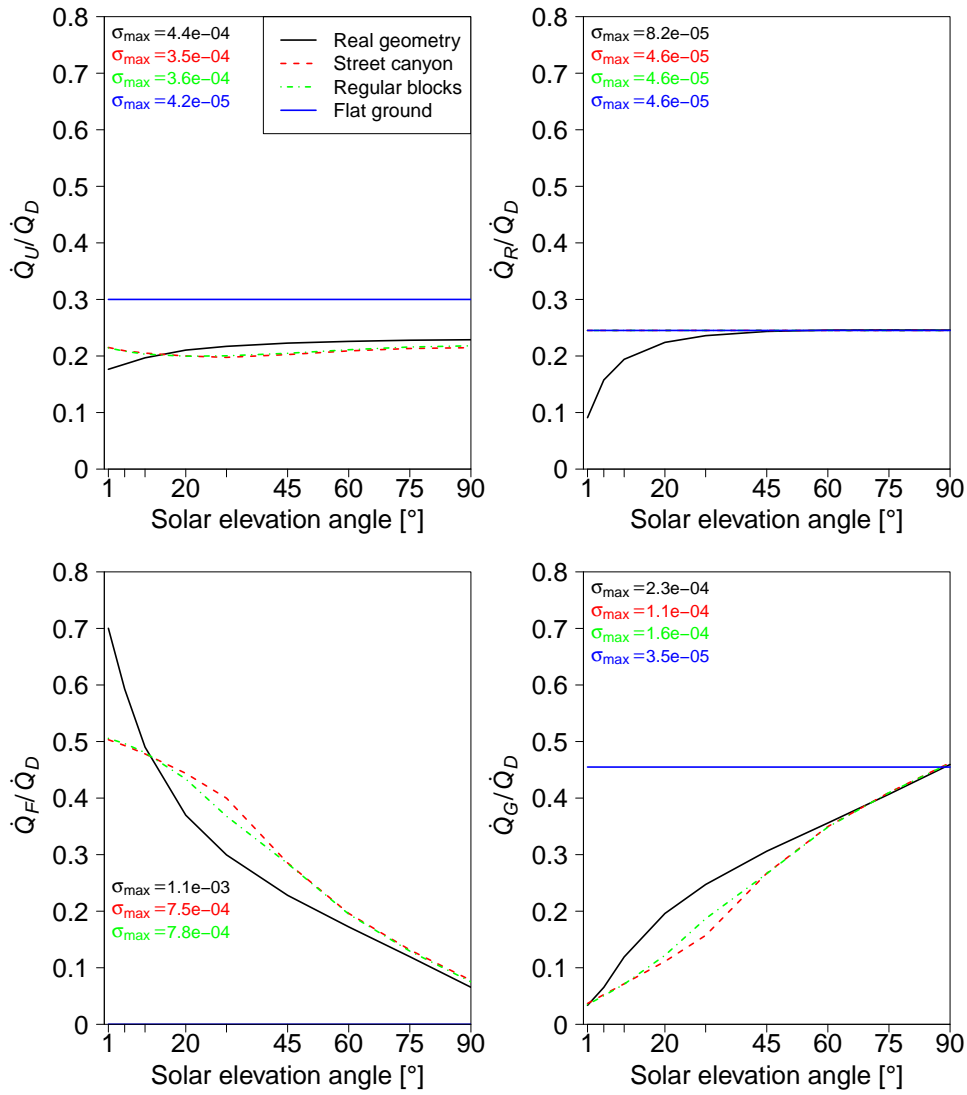


Fig. 21 Same as Fig. 17, but for LCZ2b with flat roofs

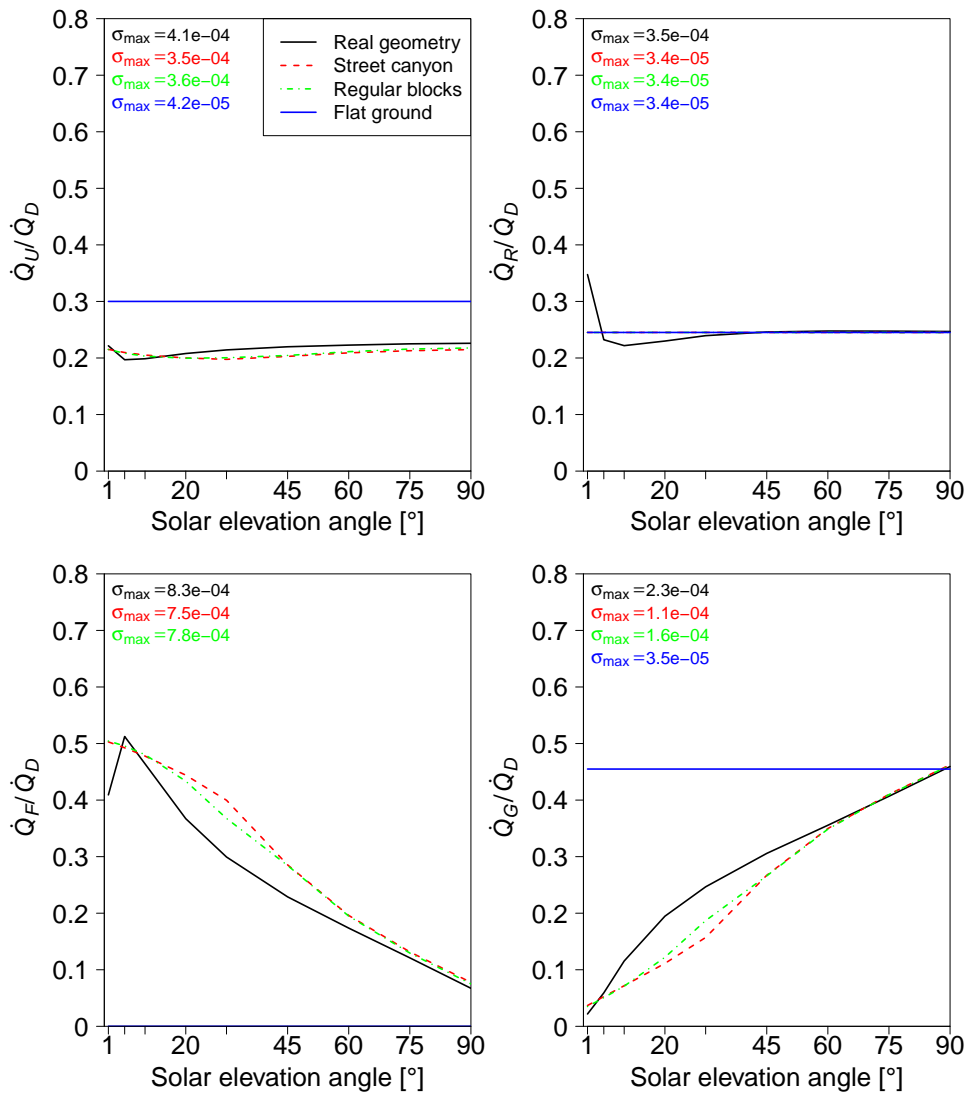


Fig. 22 Same as Fig. 17, but for LCZ2b with pitched roofs



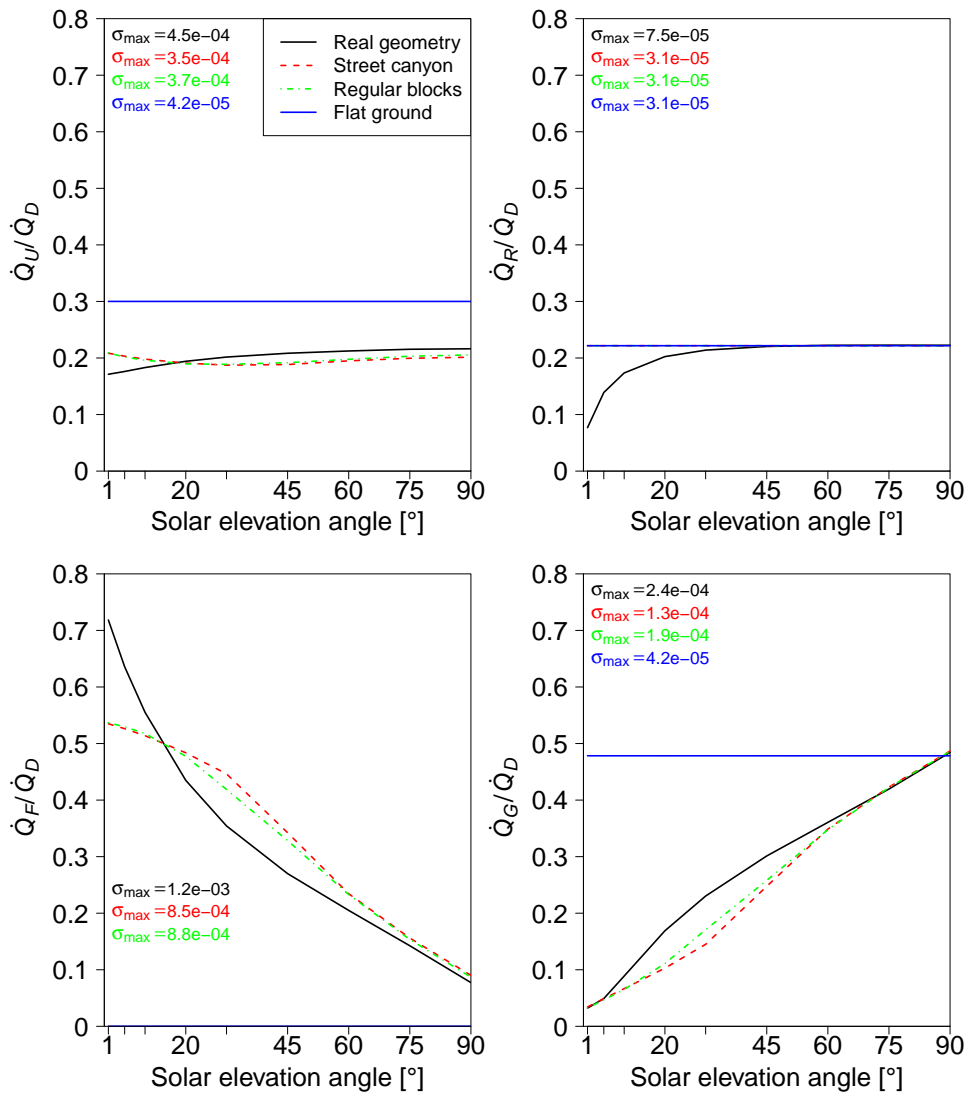


Fig. 23 Same as Fig. 17, but for LCZ5 with flat roofs

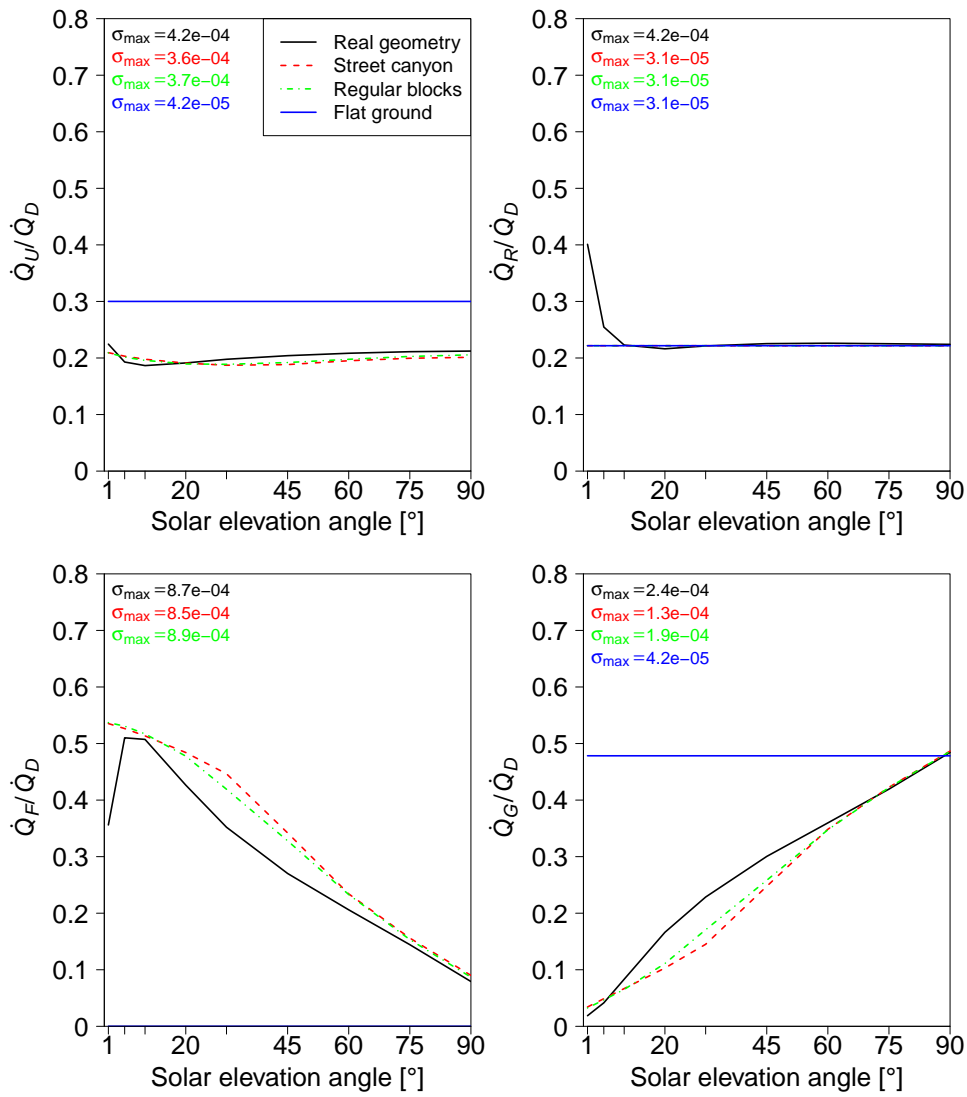


Fig. 24 Same as Fig. 17, but for LCZ5 with pitched roofs

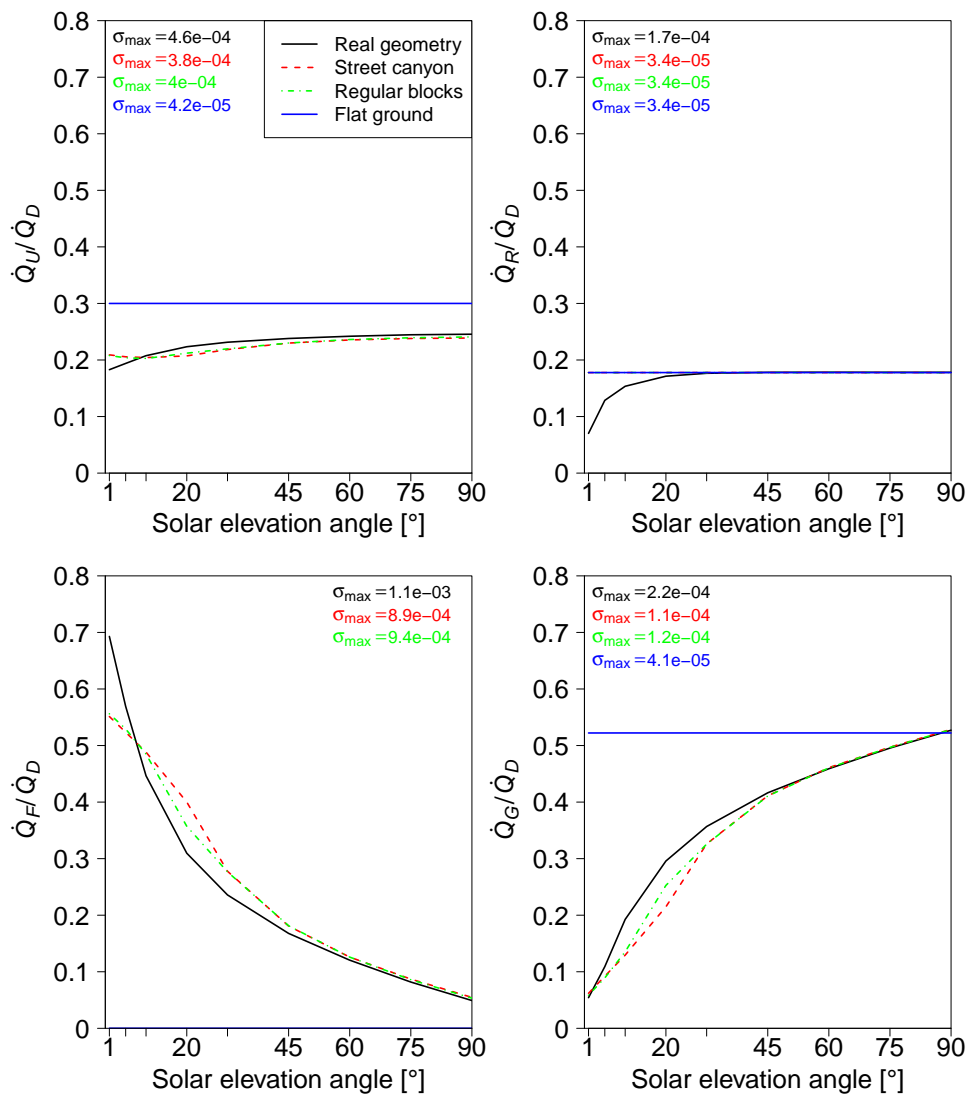


Fig. 25 Same as Fig. 17, but for LCZ10

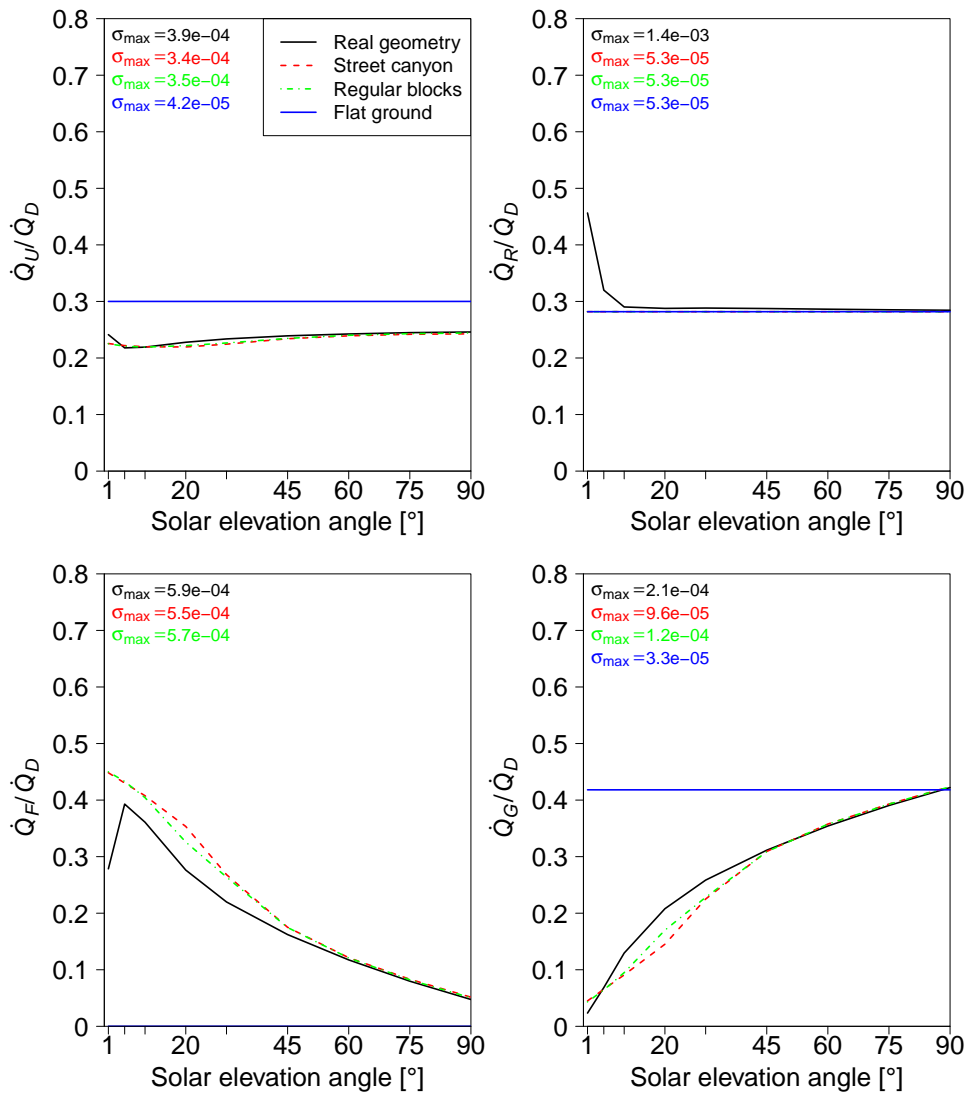


Fig. 26 Same as Fig. 17, but for LCZ3

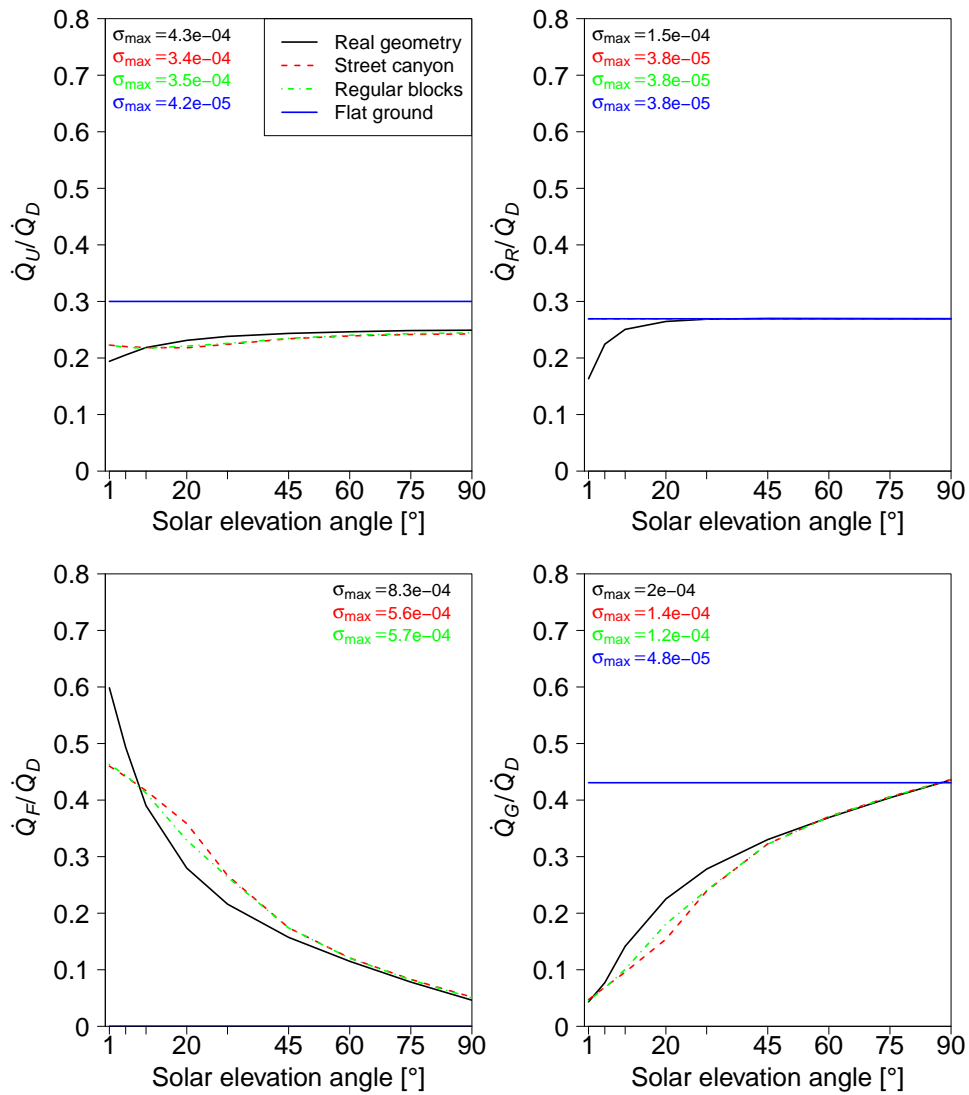


Fig. 27 Same as Fig. 17, but for LCZ6a with flat roofs

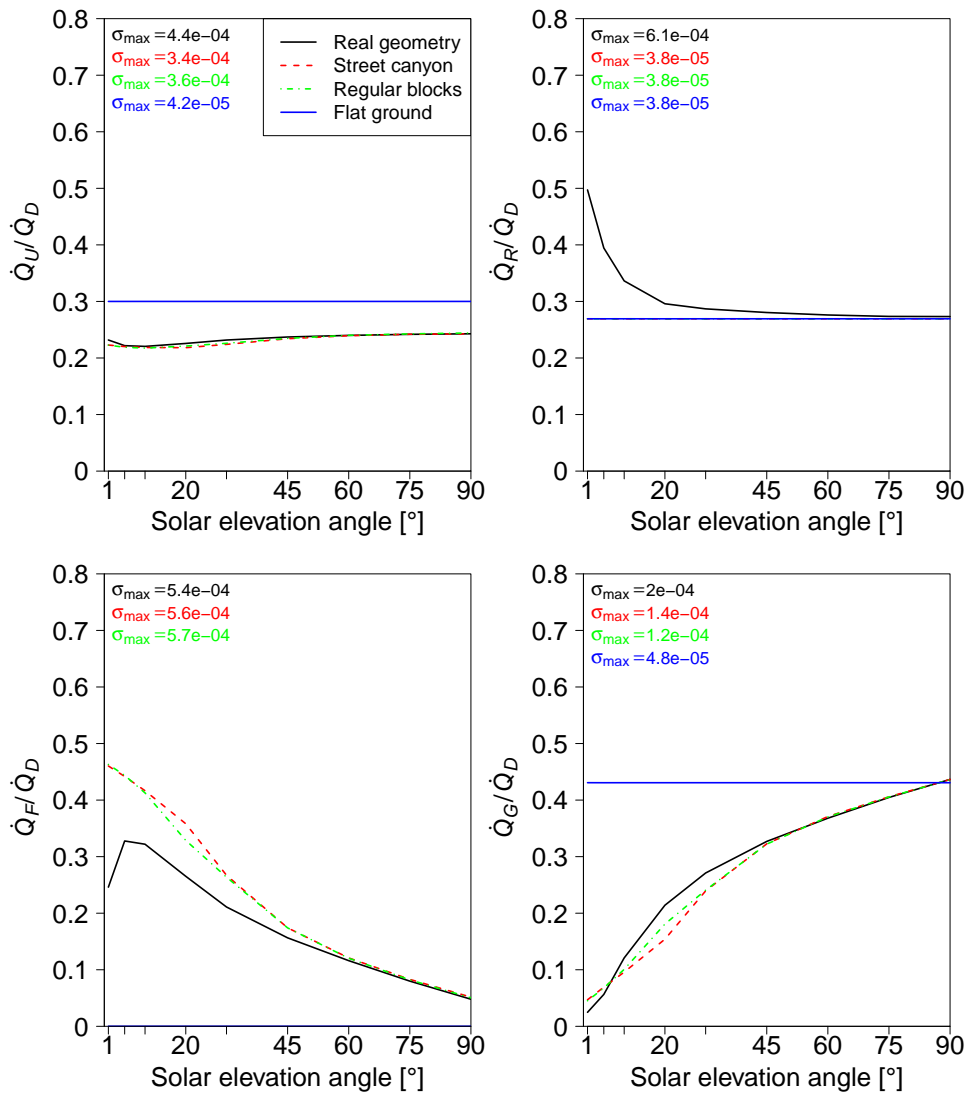


Fig. 28 Same as Fig. 17, but for LCZ6a with pitched roofs

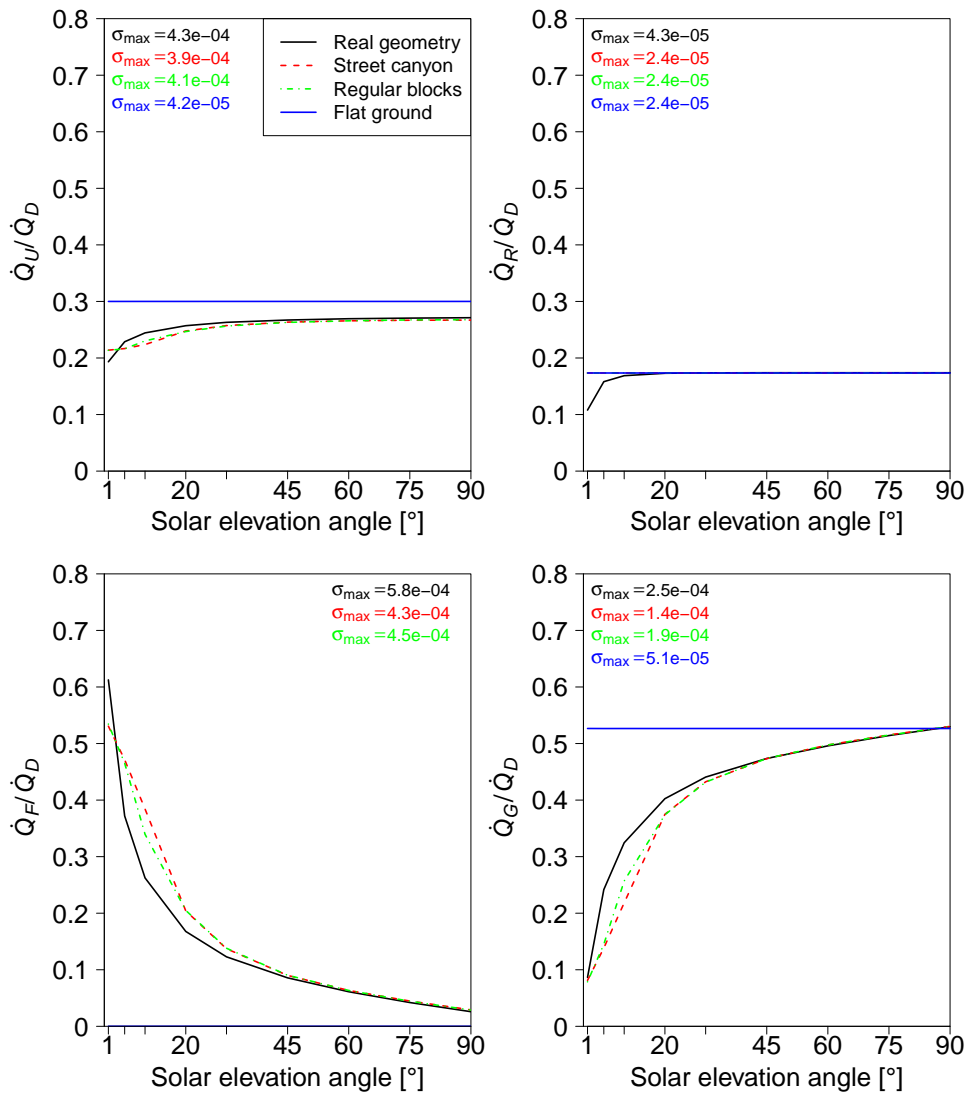


Fig. 29 Same as Fig. 17, but for LCZ6b with flat roofs

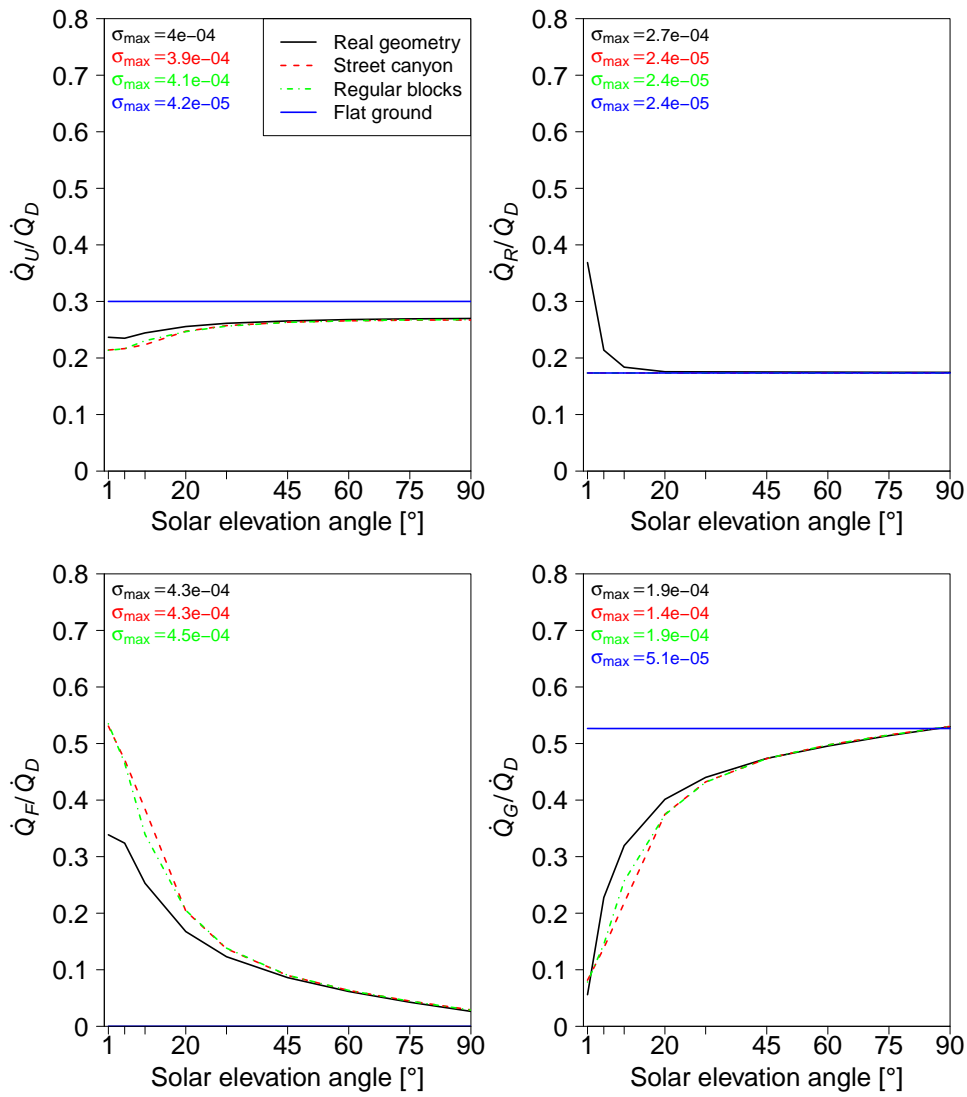


Fig. 30 Same as Fig. 17, but for LCZ6b with pitched roofs



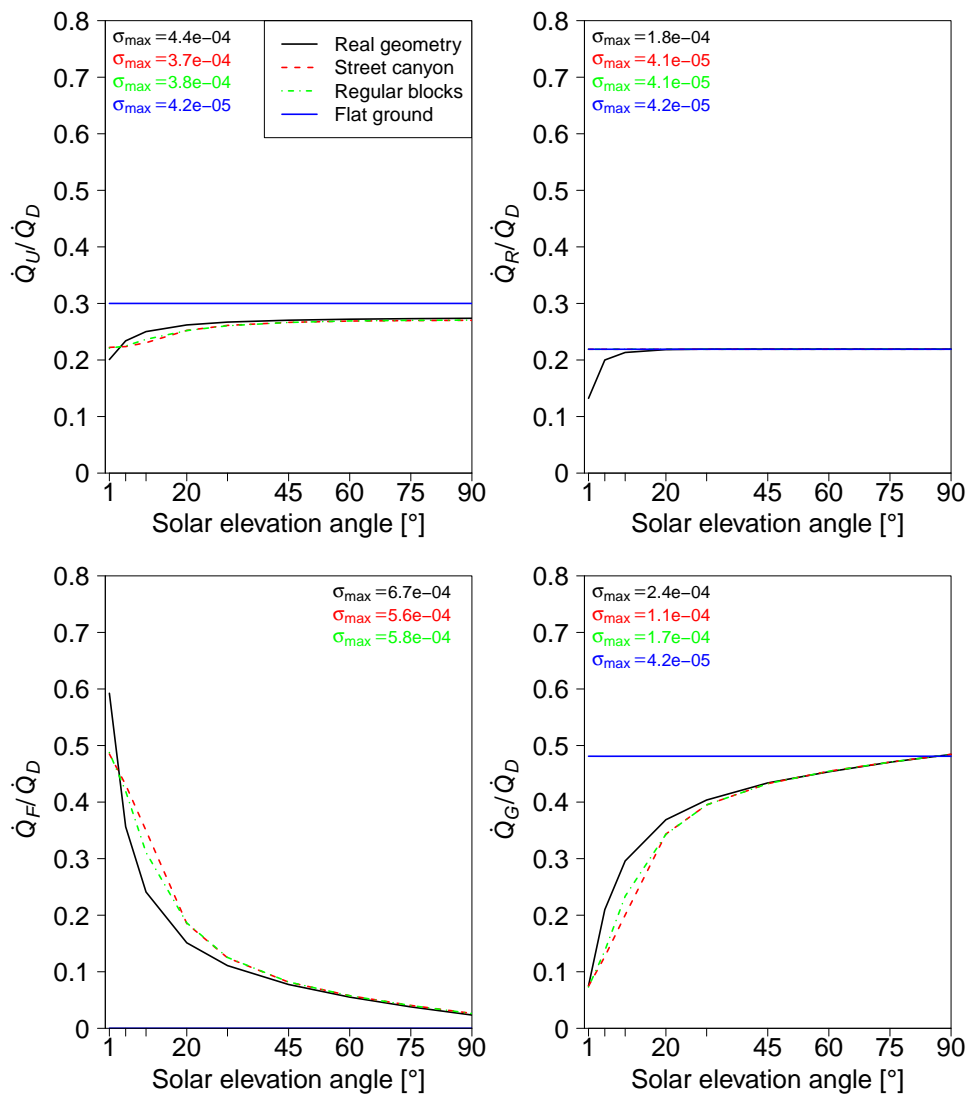


Fig. 31 Same as Fig. 17, but for LCZ8

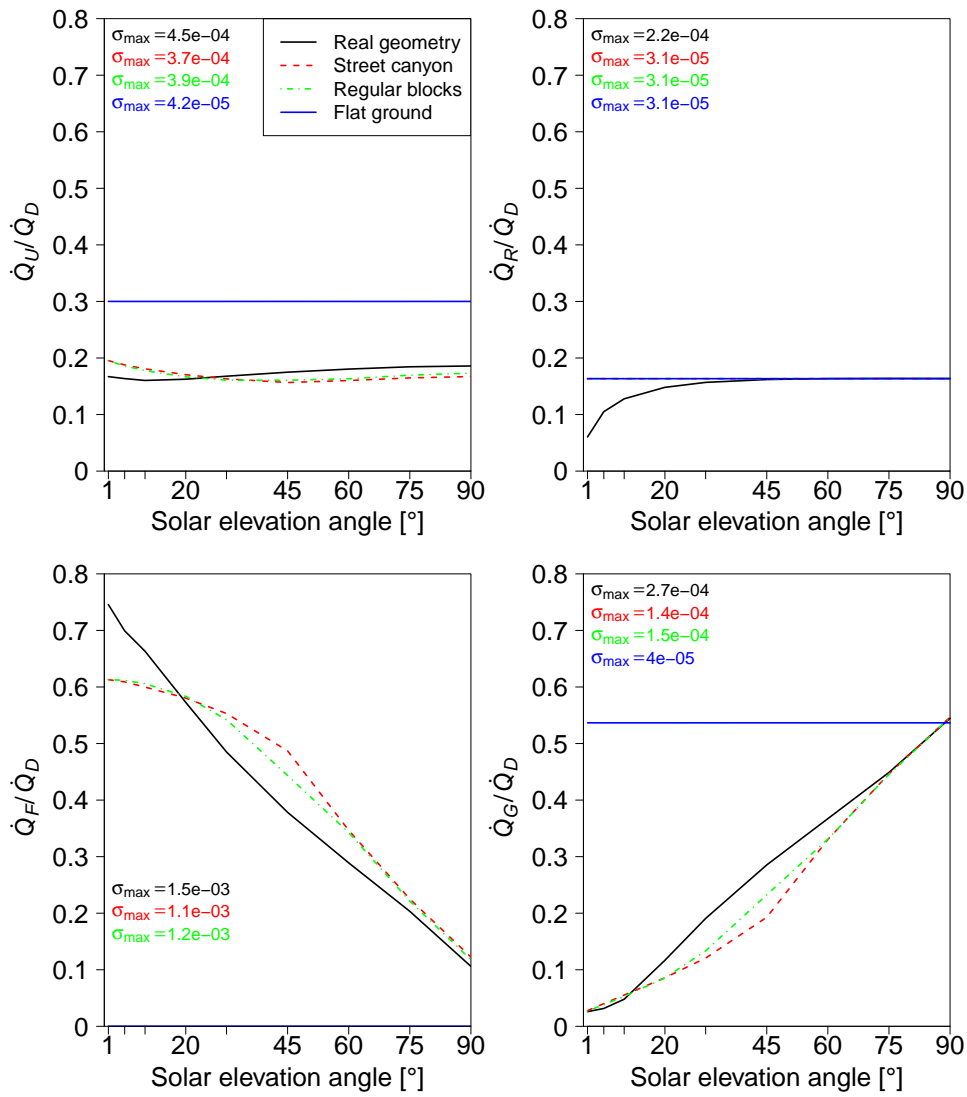
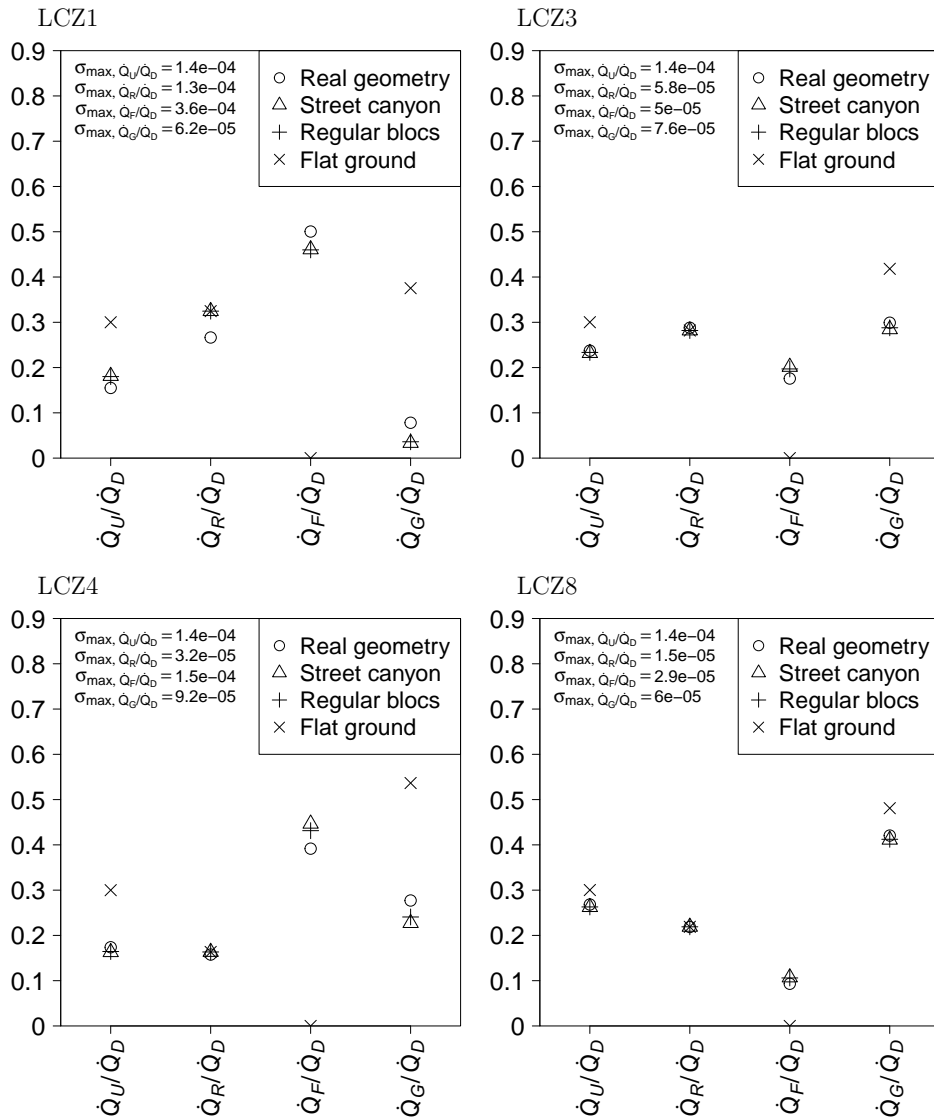


Fig. 32 Same as Fig. 17, but for LCZ4



**Fig. 33** Effect of urban morphology simplifications on the urban, roof, facade, and ground solar radiation budget for diffusive-only downwelling solar radiation and the LCZ1, LCZ3, LCZ4, and LCZ8 districts

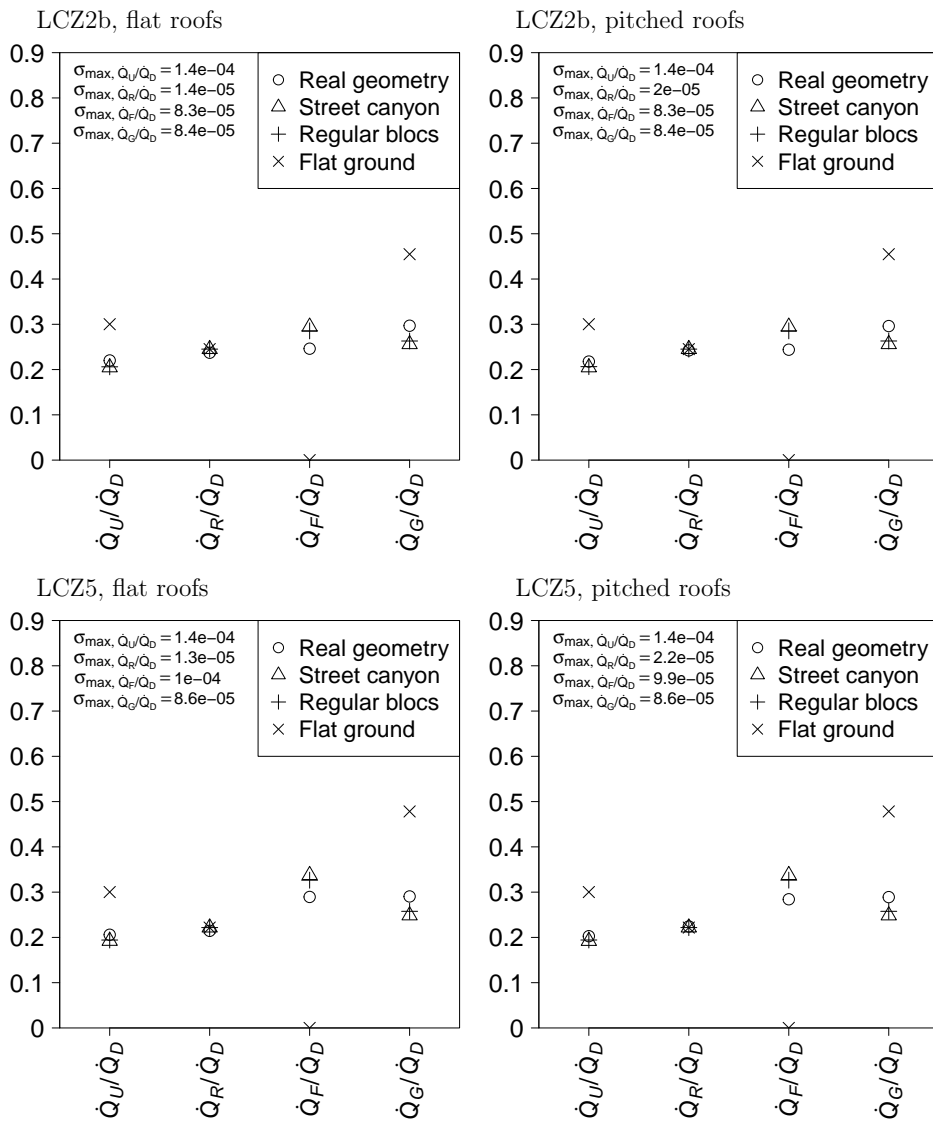
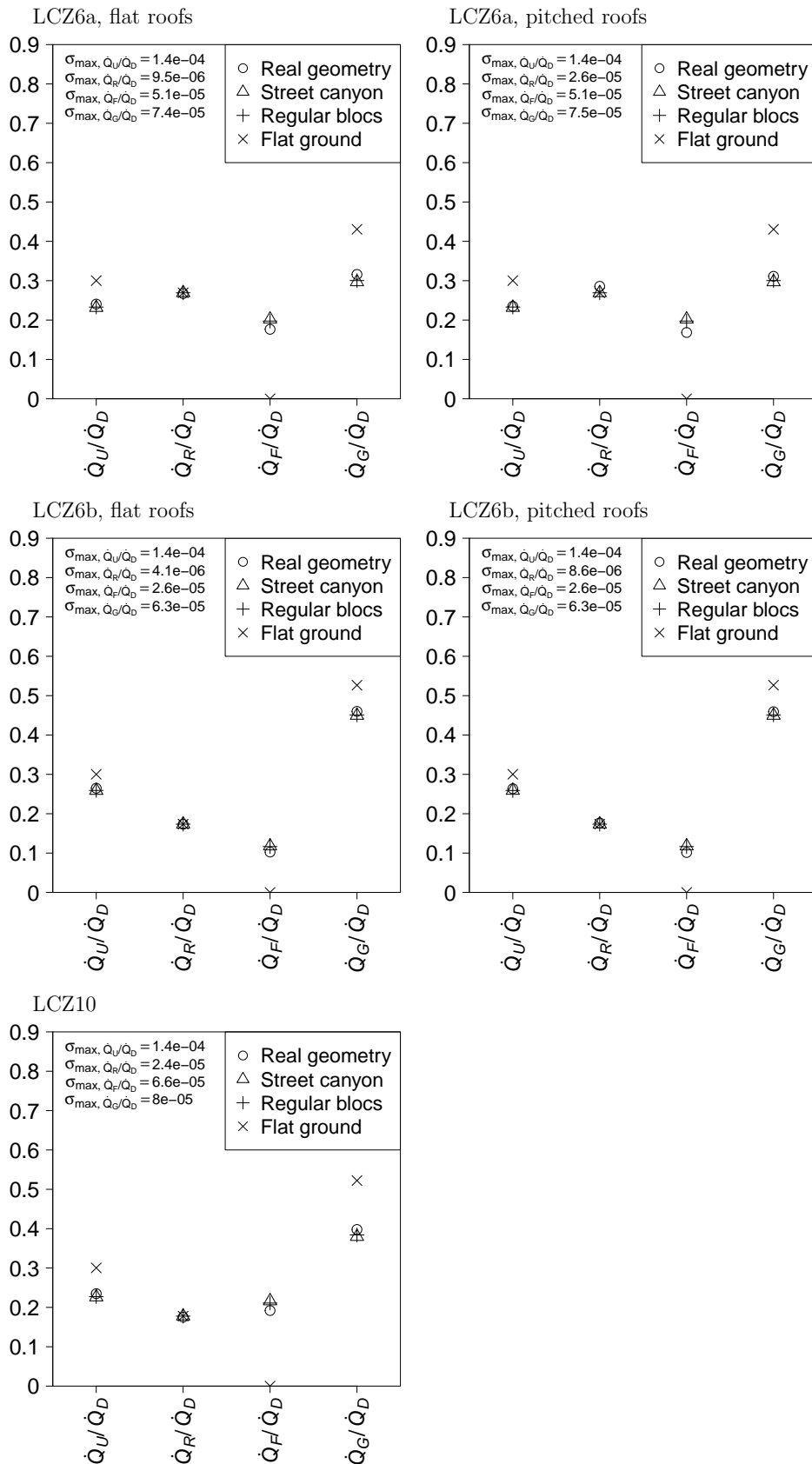
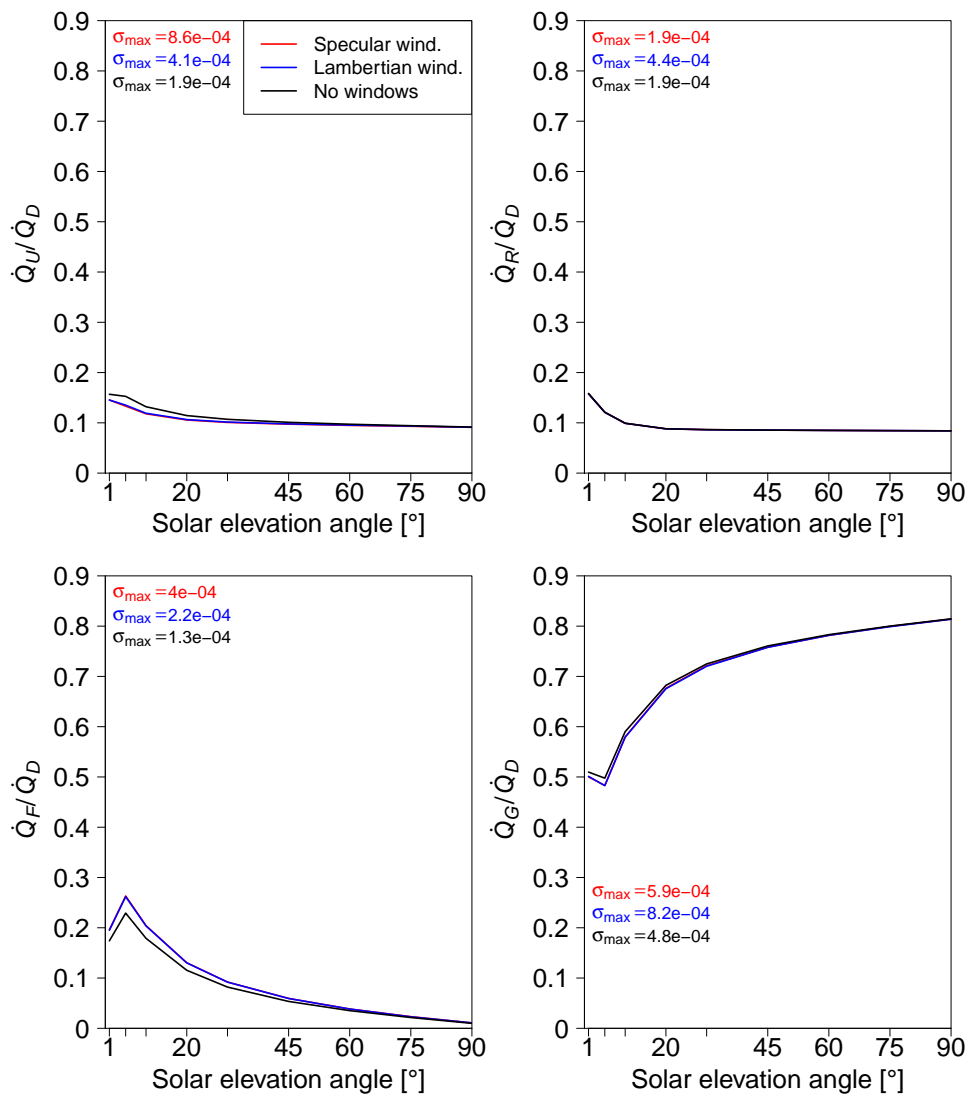


Fig. 34 Same as Fig. 33, but for the LCZ2b and LCZ5 districts with flat and pitched roofs



**Fig. 35** Same as Fig. 33, but for the LCZ6a and LCZ6b districts with flat and pitched roofs as well as the LCZ10 district



**Fig. 36** Effect of (specularly-reflecting) windows on the urban, roof, facade, and ground solar radiation budget for clear-sky conditions and the realistic LCZ9 morphology

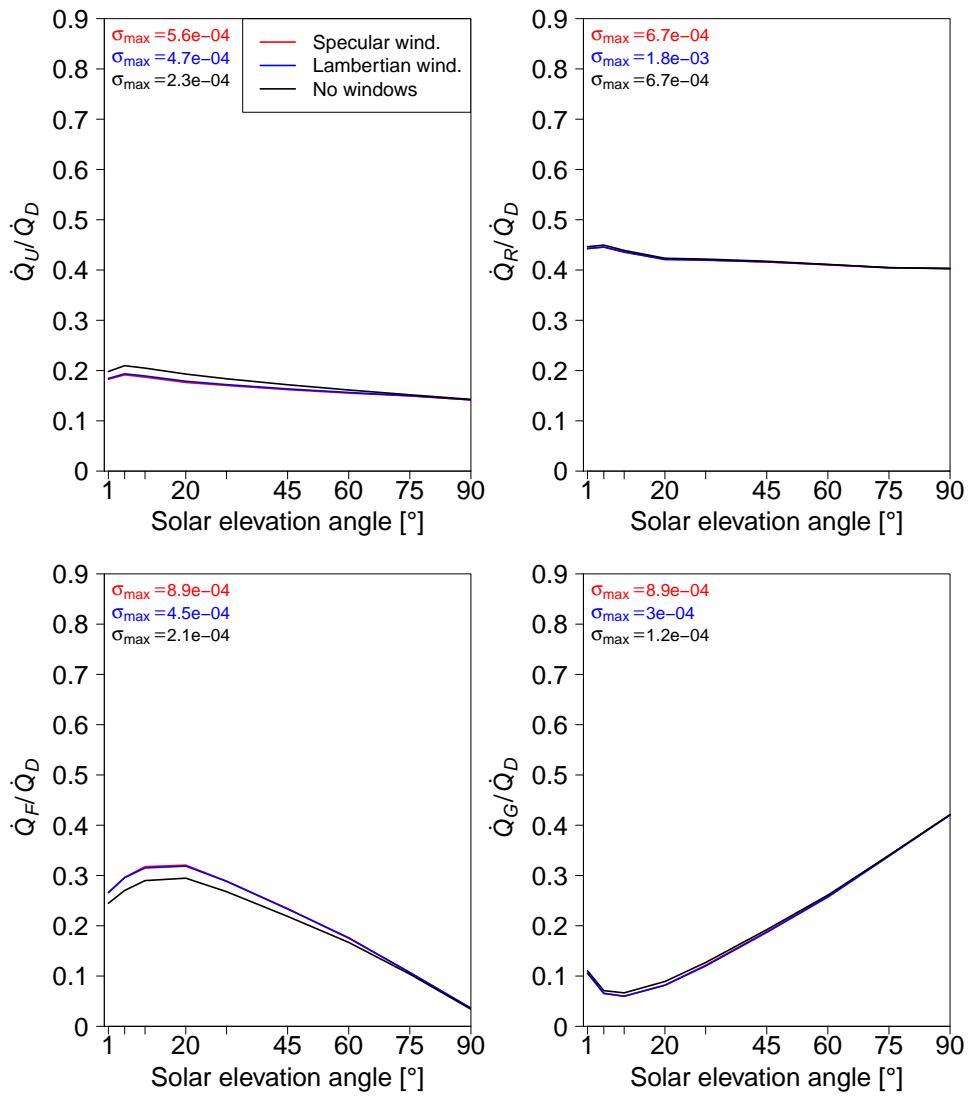


Fig. 37 Same as Fig. 36, but for the realistic LCZ2a morphology

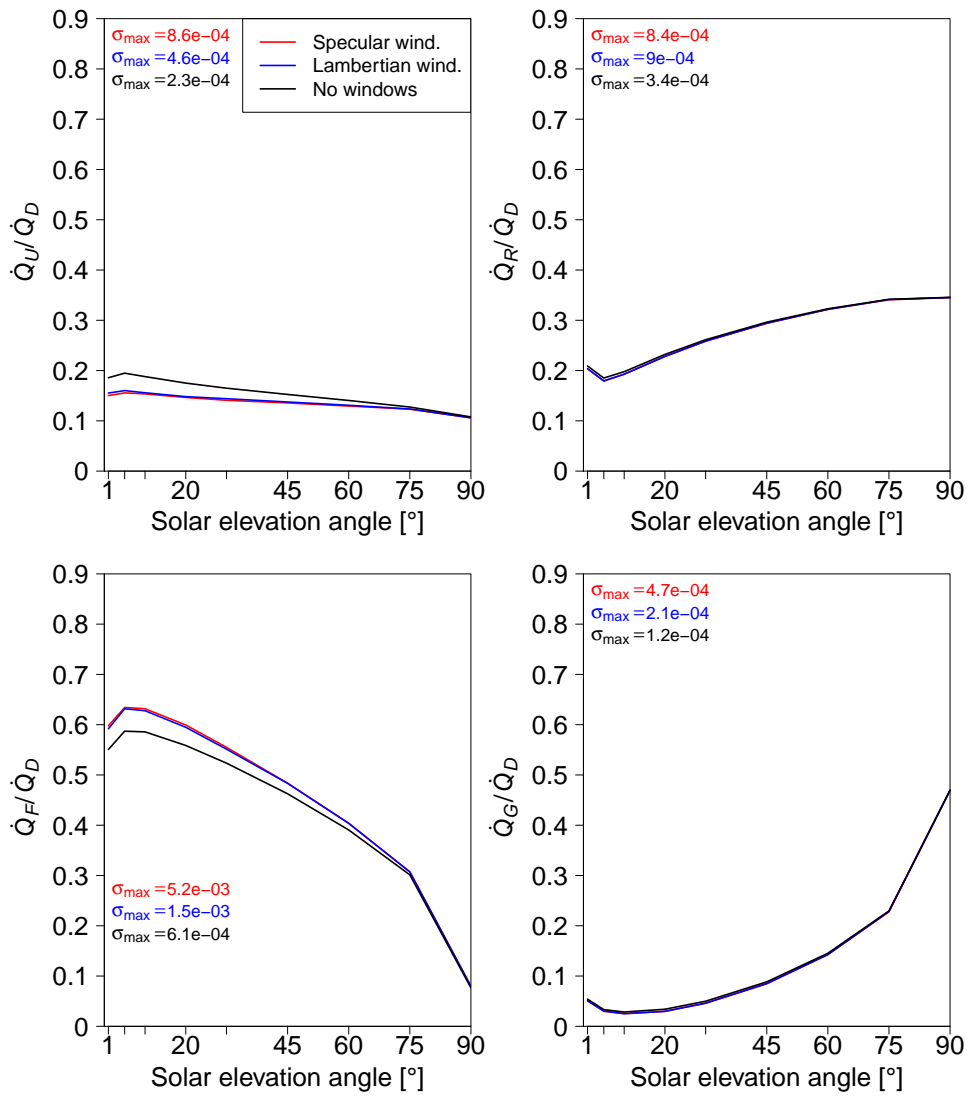
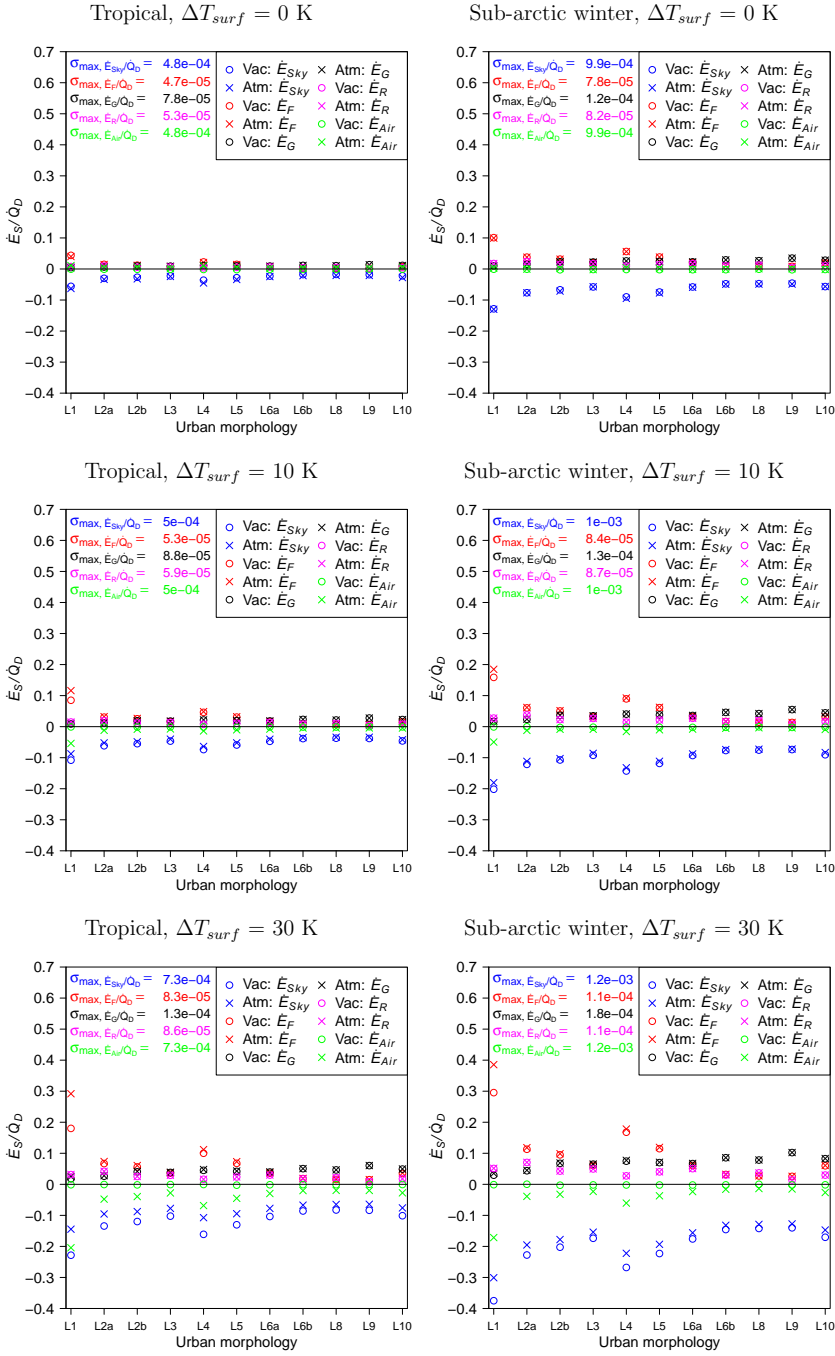


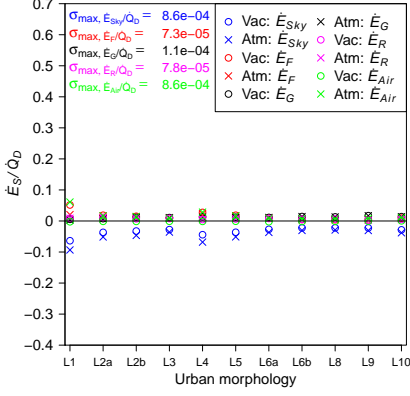
Fig. 38 Same as Fig. 36, but for the realistic LCZ1 morphology



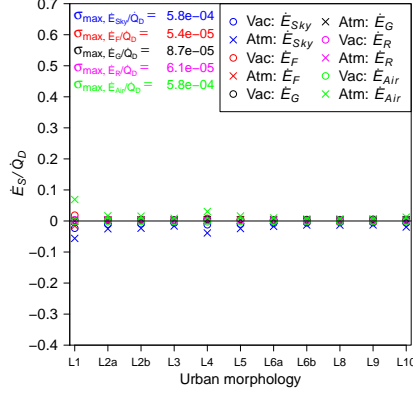


**Fig. 39** Effect of participating atmosphere on the terrestrial radiation exchanged by the sky, the roofs, the facades, the ground, and the air for clear-sky tropical for the realistic LCZ morphologies and sub-arctic winter atmospheres

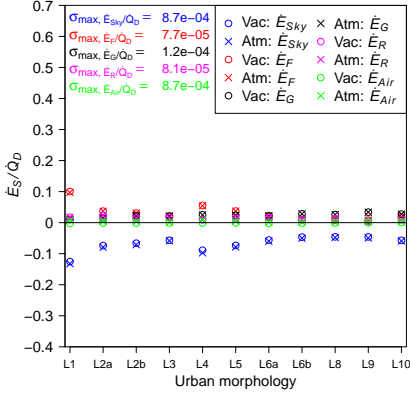
Mid-latitude winter,  $\Delta T_{surf} = -10$  K



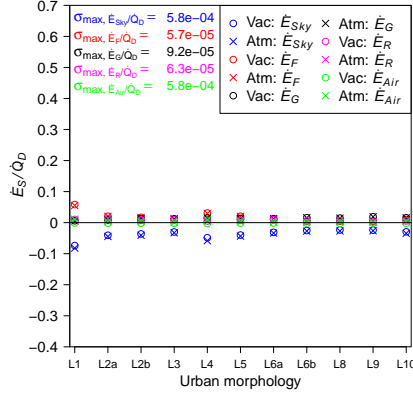
Mid-latitude summer,  $\Delta T_{surf} = -10$  K



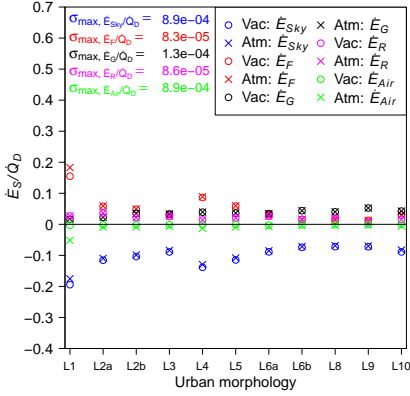
Mid-latitude winter,  $\Delta T_{surf} = 0$  K



Mid-latitude summer,  $\Delta T_{surf} = 0$  K



Mid-latitude winter,  $\Delta T_{surf} = 10$  K



Mid-latitude summer,  $\Delta T_{surf} = 10$  K

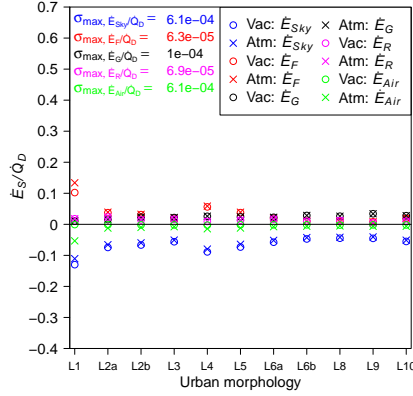
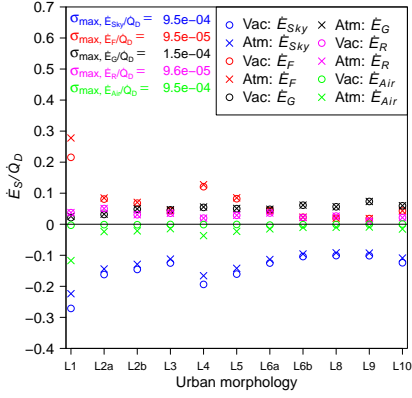
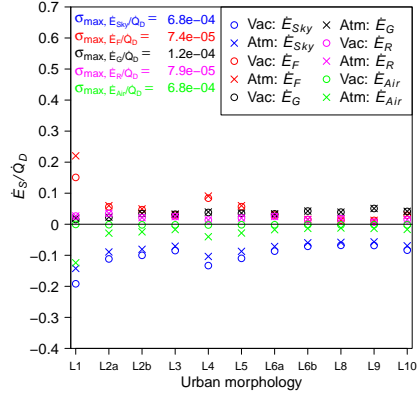
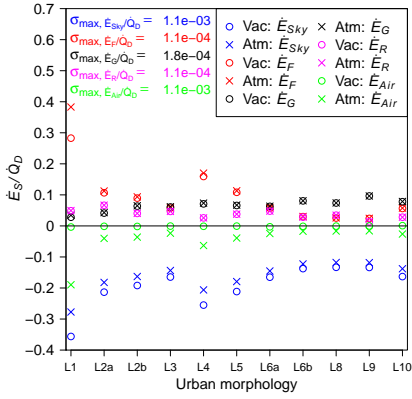
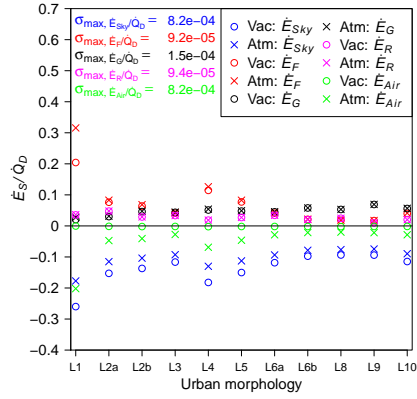
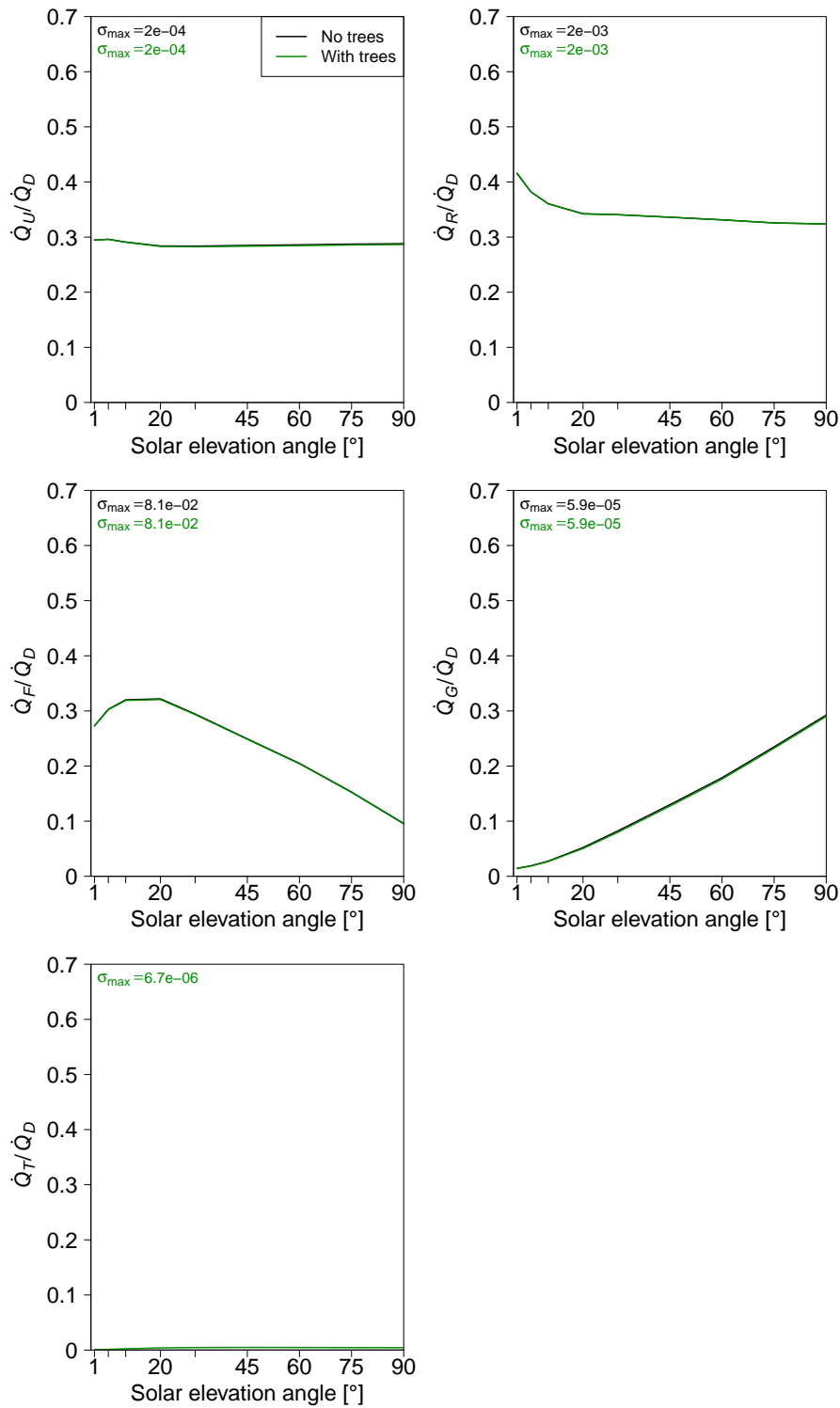


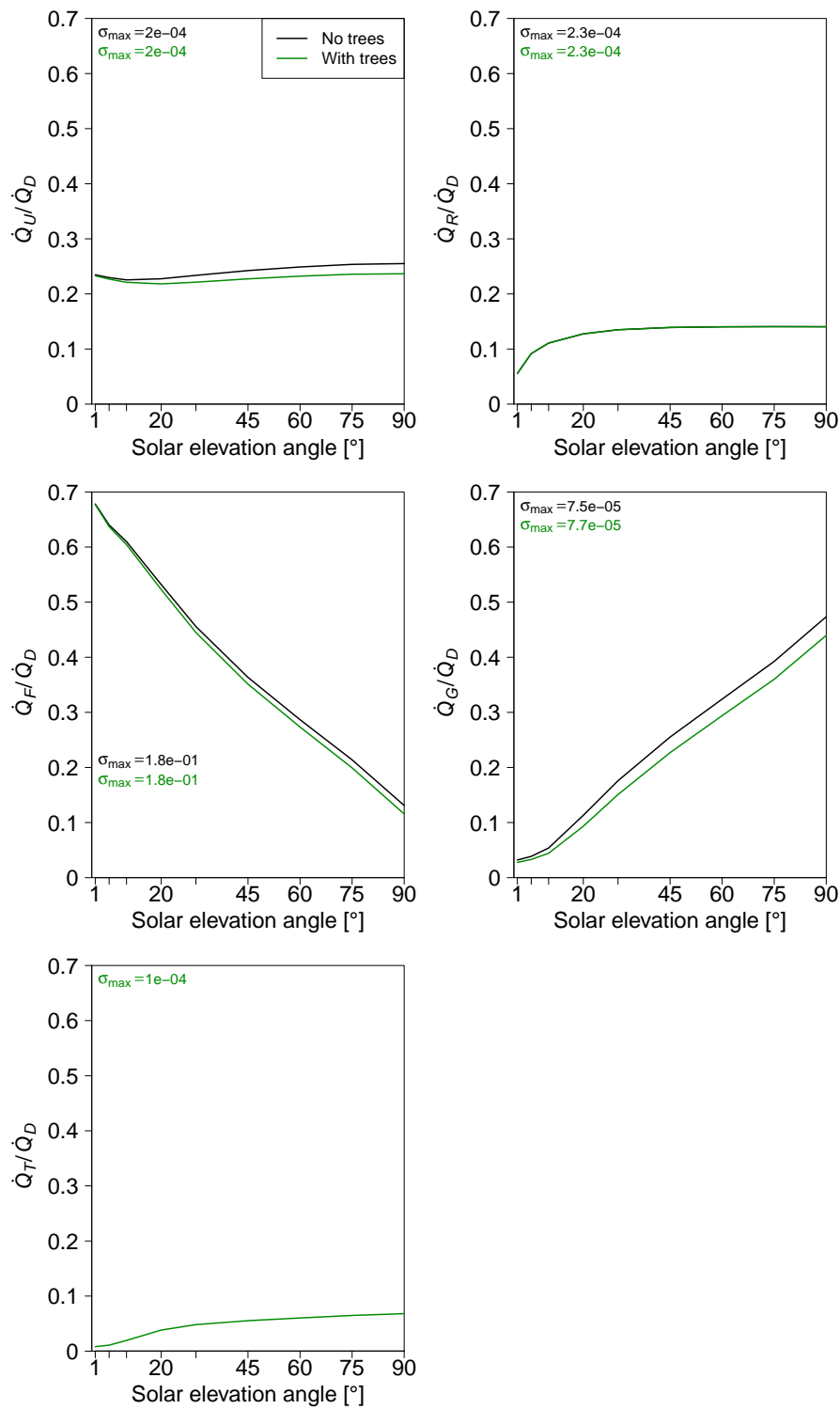
Fig. 40 Same as Fig. 39, but for clear-sky mid-latitude summer and winter atmospheres

Mid-latitude winter,  $\Delta T_{surf} = 20$  KMid-latitude summer,  $\Delta T_{surf} = 20$  KMid-latitude winter,  $\Delta T_{surf} = 30$  KMid-latitude summer,  $\Delta T_{surf} = 30$  K

**Fig. 41** Same as Fig. 40, but for different skin surface temperature of urban facets



**Fig. 42** Effect of trees on the urban, roof, facade, ground, and tree solar radiation budget for direct-only downwelling solar radiation and the realistic LCZ2a morphology



**Fig. 43** Same as Fig. 42, but for the realistic LCZ4 morphology

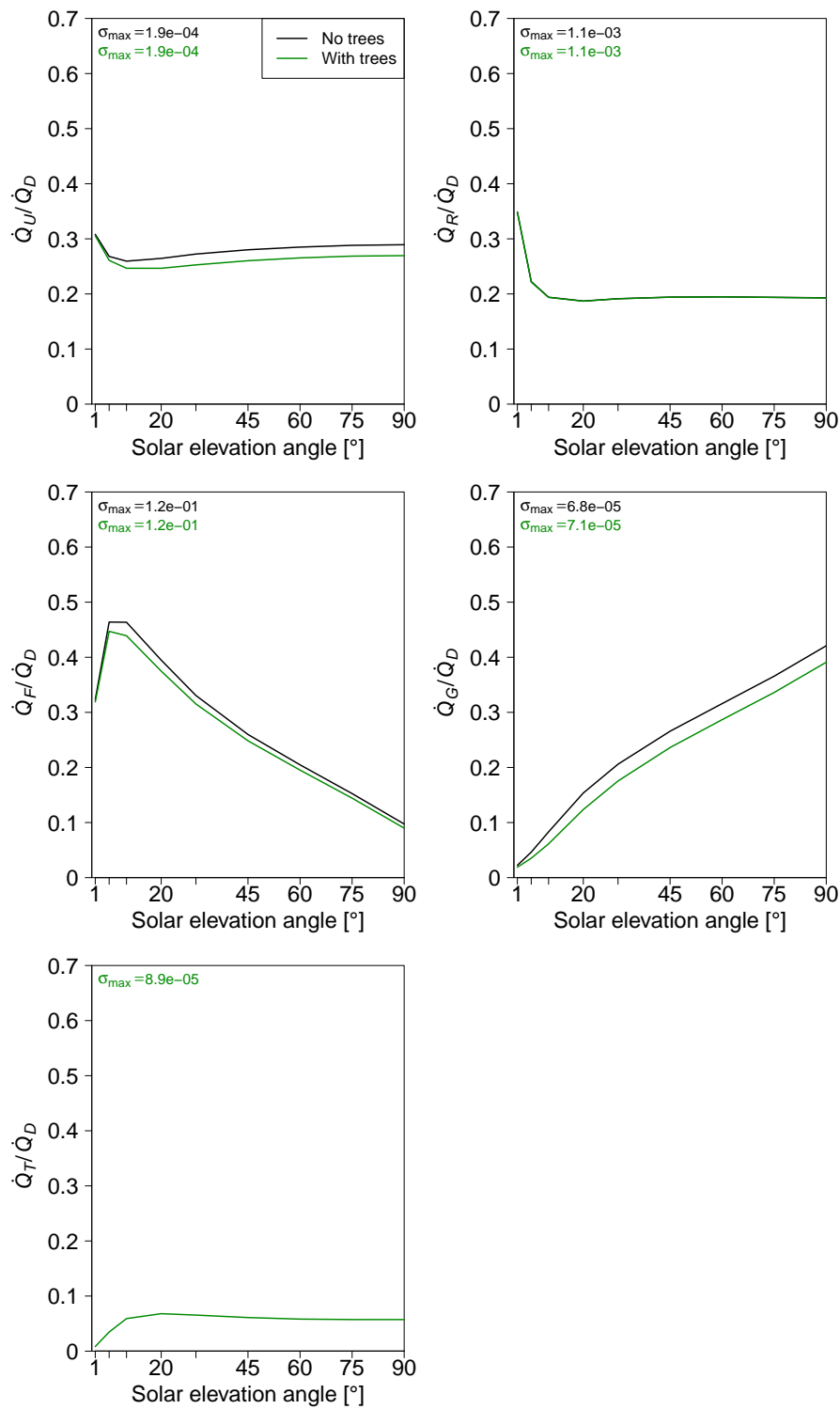
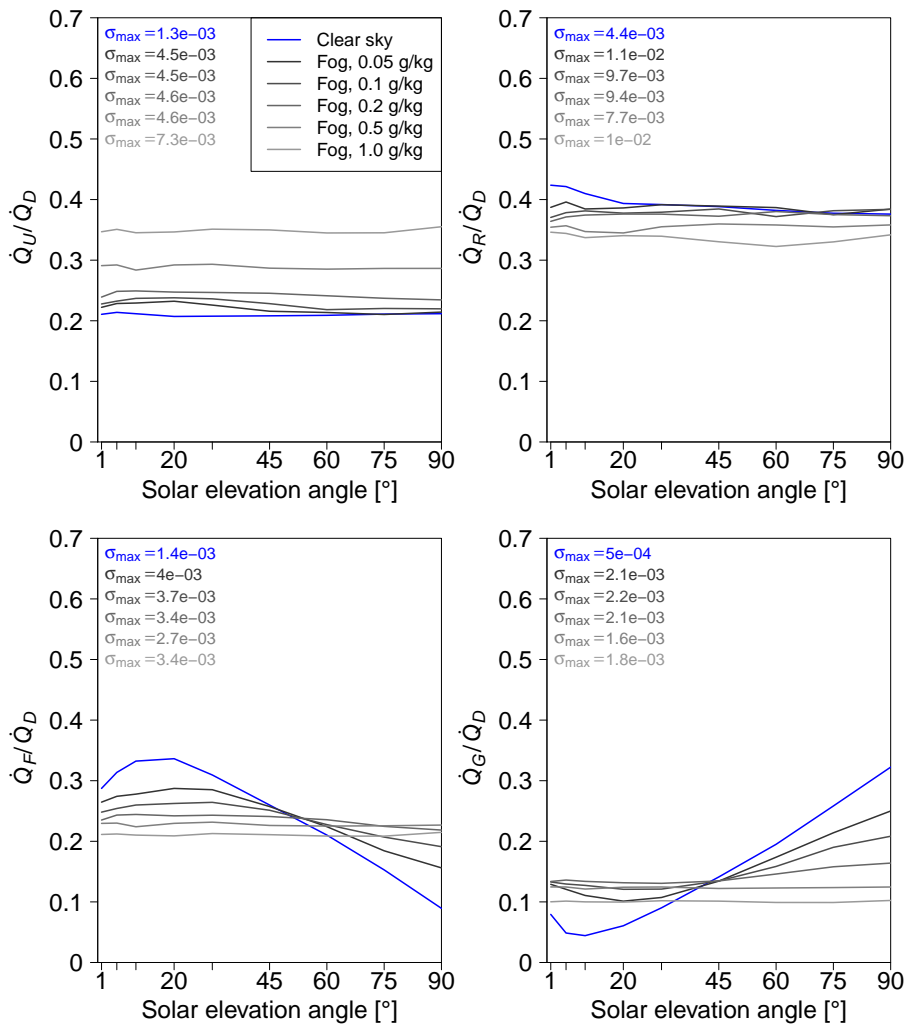


Fig. 44 Same as Fig. 42, but for the realistic LCZ5 morphology



**Fig. 45** Effect of fog on the urban, roof, facade, and ground solar radiation budget for the realistic LCZ2a morphology

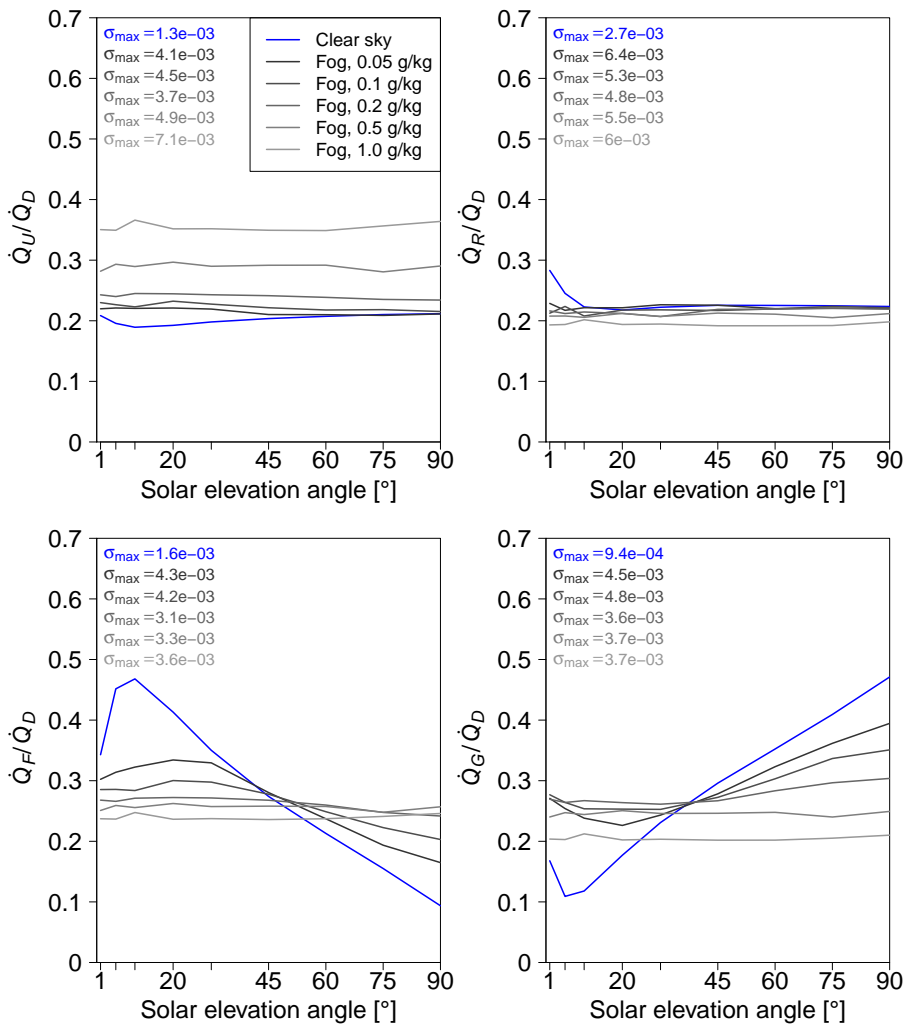


Fig. 46 Same as Fig. 45, but for the realistic LCZ5 morphology



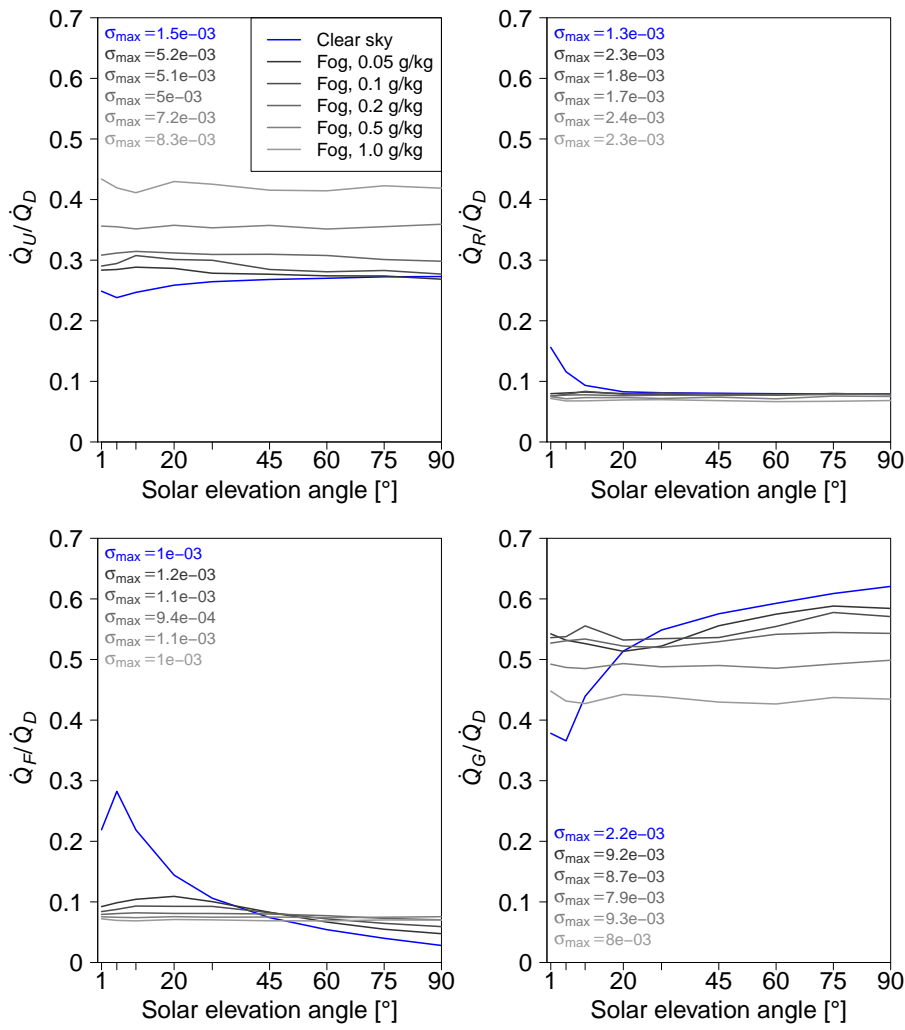
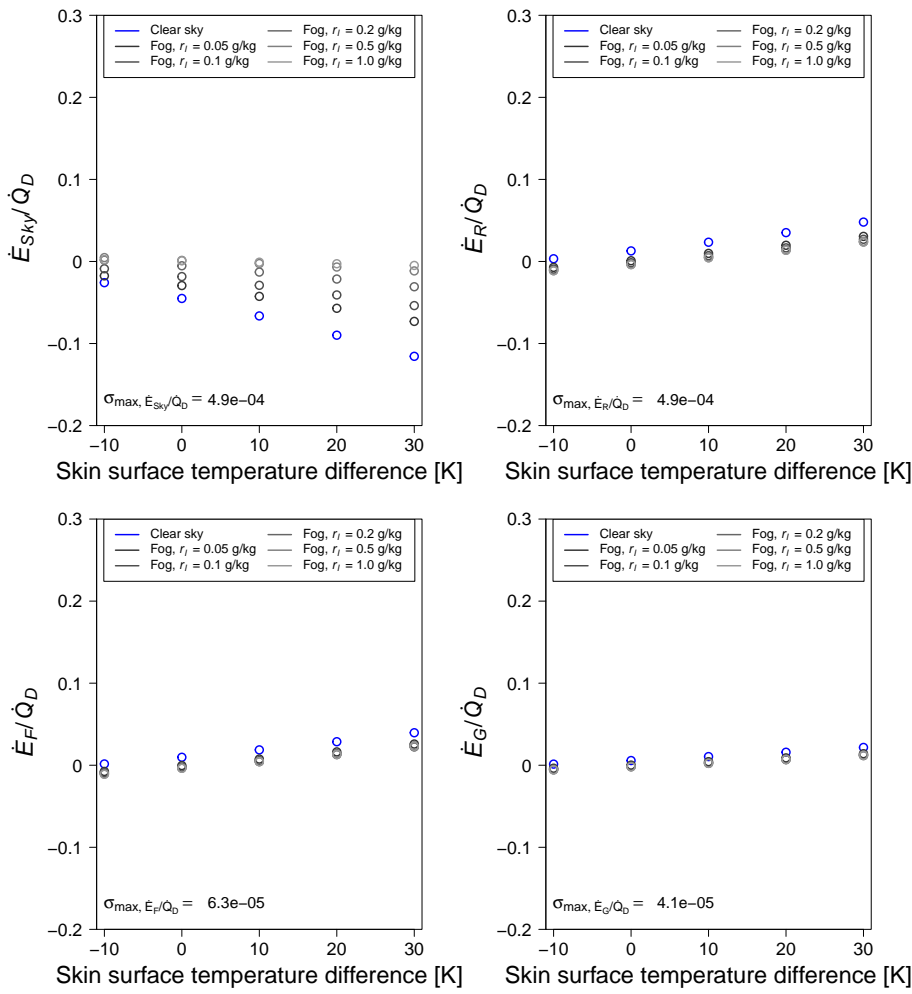
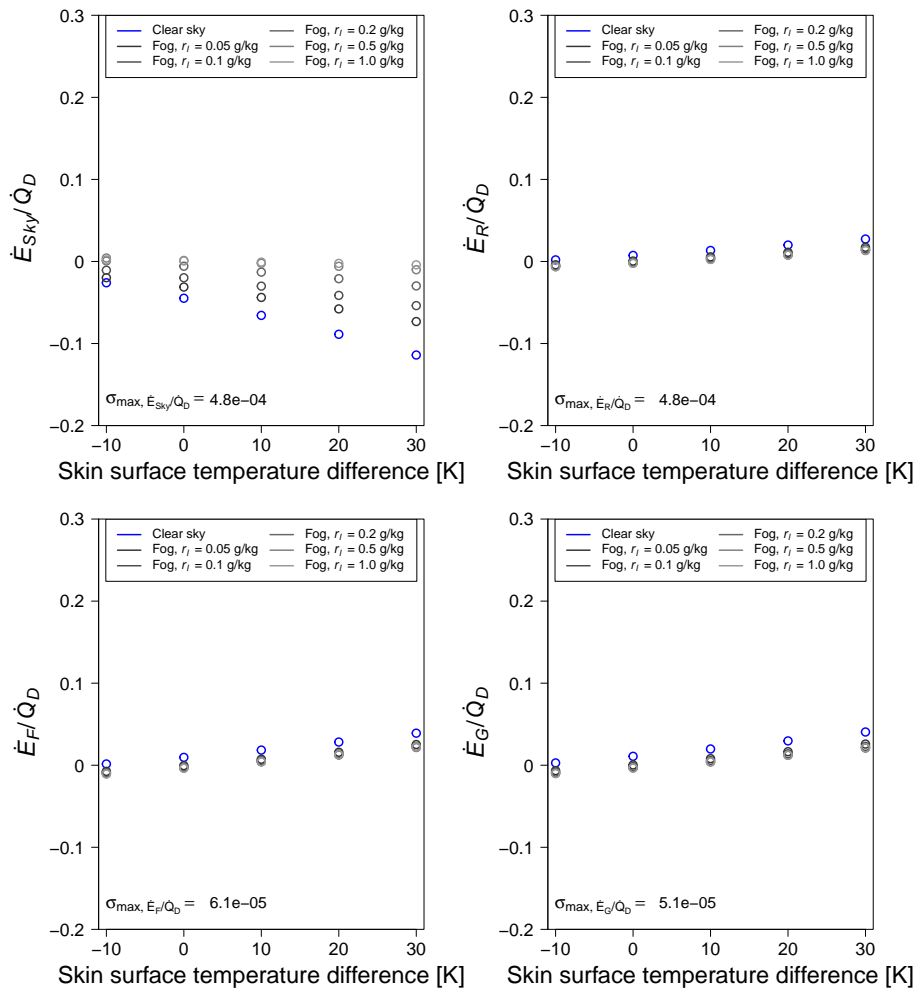


Fig. 47 Same as Fig. 45, but for the realistic LCZ9 morphology



**Fig. 48** Effect of fog on the terrestrial radiation exchanged by the sky, the roofs, the facades, and the ground for the realistic LCZ2a morphology



**Fig. 49** Same as Fig. 48, but for the realistic LCZ5 morphology

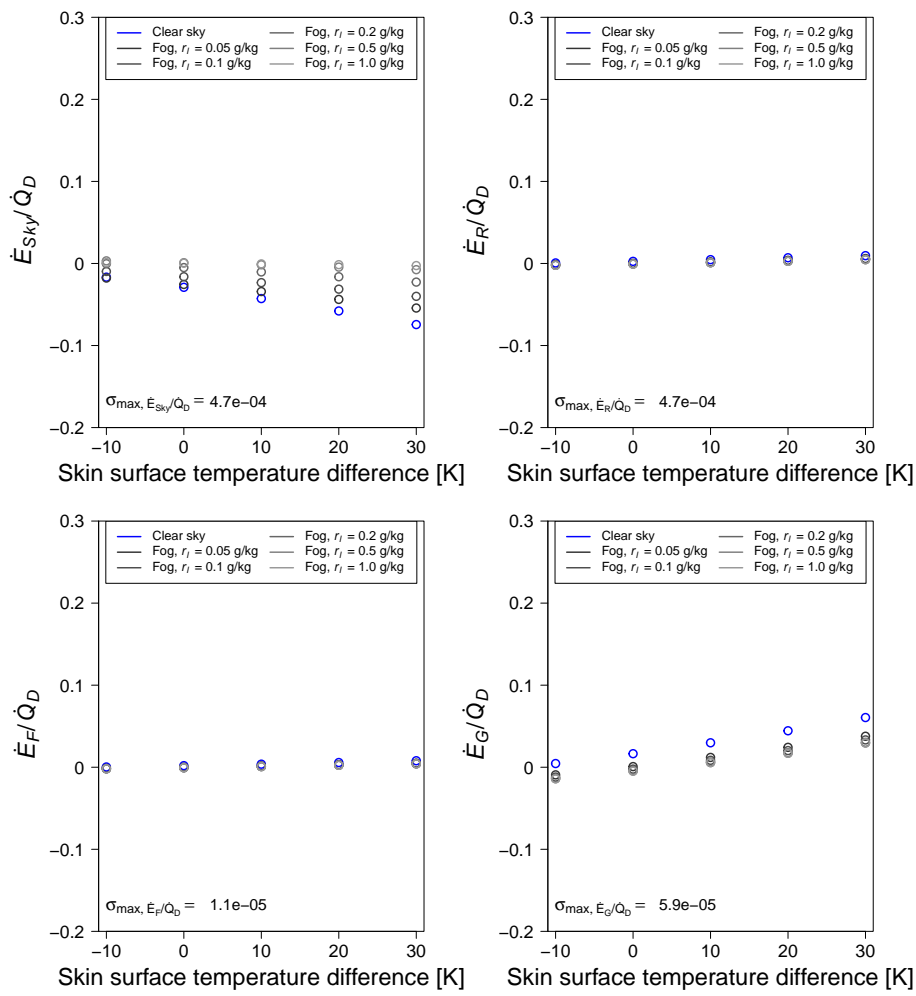


Fig. 50 Same as Fig. 48, but for the realistic LCZ9 morphology